

*Nobody ever figures out what life is all about, and it doesn't matter.  
Explore the world. Nearly everything is really interesting  
if you go into it deeply enough.*  
Richard P. Feynman



## Abstract

Hadronetherapy is a medical treatment based on beams of charged particles accelerated towards deep-seated tumors on clinical patients. The reason why it is increasingly used is the favorable depth dose profile, according to which the release of dose is low and quite constant in the entrance channel but sharply focused near the end of the path, originating the so-called *Bragg peak*. However, nuclear interactions between the beam and the human body particles occur, generating target and projectile nuclear fragments which modify the dose profile.

Nuclear fragmentation has to be inspected even in the context of space radioprotection. Long-term human missions outside the Earth's orbit are going to be planned in the next years, among which the NASA travel to Mars, and it is fundamental to protect astronauts health and electronics from radiation exposure and consequent nuclear fragmentation.

To overcome the lack of experimental data of nuclear fragmentation reactions in the energy range of hadrontherapy and space radioprotection interest, the FOOT (FragmentatiOn Of Target) experiment has been conceived with the main aim of measuring differential nuclear cross sections with a resolution less than 5%.

In this thesis, a first analysis of data taken at the GSI with a beam of  $^{16}O$  at  $400 \text{ MeV}/n$  impinging on a target of graphite ( $C$ ) will be presented, showing the first preliminary results of elemental cross sections and differential ones in angle.

A MC data set was exploited to study the performance of the Kalman tracking reconstruction algorithm, whose results underline its high reliability. MC cross section is then calculated comparing MC generated particles with reconstructed tracks and a strong agreement was obtained as a closure test of the applied analysis procedure. Finally, a preliminary experimental cross section was measured, finding a high comparability with MC measurements for heavy fragments. (1991 caratteri per un max di 2000 secondo le direttive unibo...)



# Contents

<b>Introduction</b>	<b>i</b>
<b>1 Charged particles interactions</b>	<b>1</b>
1.1 Electromagnetic interactions . . . . .	1
1.2 Nuclear interactions . . . . .	6
<b>2 Applications</b>	<b>11</b>
2.1 Hadrontherapy . . . . .	11
2.2 Radioprotection in space . . . . .	16
2.3 Experimental cross sections . . . . .	21
<b>3 The FOOT experiment</b>	<b>33</b>
3.1 The goal and experimental requirements . . . . .	33
3.2 Design criteria . . . . .	35
3.3 Electronic detector setup . . . . .	35
<b>4 GSI 2021 Analysis</b>	<b>45</b>
4.1 GSI facility . . . . .	45
4.2 The FOOT setup at GSI 2021 data taking . . . . .	45
4.3 Analysis software . . . . .	46
4.4 Fragment identification . . . . .	48
4.5 Tracking . . . . .	49
4.6 Analysis strategy . . . . .	54
<b>5 Results</b>	<b>67</b>
5.1 Closure test on MC dataset . . . . .	67
5.2 Experimental results . . . . .	81
<b>Conclusions</b>	<b>89</b>
<b>Bibliography</b>	<b>98</b>



# Introduction

According to the World Health Organization (WHO), cancer is a leading cause of death worldwide, accounting for nearly 10 millions deaths in 2020<sup>1</sup>. However, the percentage of survival is increasing considerably: up to 2021, 65% of women and 60% of men are alive 5 years after diagnosis<sup>2</sup>. That is the consequence of a wider diffusion of screening programs as well as an improvement in the performance of the adopted therapies.

Among them, an important role is played by hadrontherapy, for which there is growing evidence about its safety and effectiveness for a large variety of clinical situations . It is a medical treatment based on the delivery of beams of charged particles towards deep-seated tumors of a patient. The reason for which it is increasingly used is the favorable depth-dose profile, according to which the release of dose is low in the entrance channel and increases sharply near the end of the particle range, which is called Bragg peak (BP). Hence, it is possible to tune the beam energy in order to release the highest amount of dose in the tumor region, sparing healthy tissues and organs around it. This represents a big advantage over conventional radiotherapy, which is instead based on the use of beams of X-rays. Unlike charged particles, their radiation intensity is high at the beginning and decrease exponentially as they enter into a material.

Once the tumor is evaluated, a Treatment Planning System (TPS) is commissioned for every patient in order to define the specific dose of the beam. It consists of a software based on advanced Monte Carlo models which simulates several aspects of the treatment, among which the beam energy release and its interaction with the human body. However, at the moment some uncertainties in TPS calculation are present due to inability to exactly evaluate the contribution of nuclear fragmentation processes.

Indeed, beams can interact with nuclei of the human body producing two

---

<sup>1</sup>Global cancer observatory: Cancer today. (accessed in September 2022)  
<https://gco.iarc.fr/today>

<sup>2</sup>AIOM, Associazione Italiana di Oncologia Medica, 2021. I numeri del cancro in Italia  
[https://www.aiom.it/wp-content/uploads/2021/10/2021\\_NumeriCancro\\_web.pdf](https://www.aiom.it/wp-content/uploads/2021/10/2021_NumeriCancro_web.pdf)

types of fragments: on the one hand, projectile fragments are high energy particles which can release dose beyond the BP; on the other hand, target fragments have low energy and stop nearby where they are generated, causing dose release even in healthy tissues. Due to their effects and the lack of experimental data, these processes need to be studied.

Nuclear fragmentation is also fundamental to deal with the field of space radioprotection. Long-term space missions outside the Earth's orbit are nowadays an important intent for public and private space agencies: for example, NASA intends to send the first humans back to the Moon within 2024, in sight of the following mission to Mars in the 2030s. However, several critical aspects need to be faced, among which astronauts' health prevention and electronics protection from risks due to space and cosmic radiations, the main source of fragmentation processes. In fact, for a six-month journey to Mars an astronaut would be exposed to roughly 300 mSv of radiation, to be compared with the 3 mSv received on Earth during the same amount of time, increasing cancer probability of more than 3%.

At present, there is a lack of experimental data about nuclear fragmentation for light fragments ( $Z < 10$ ) in the energy range between 100 MeV/n and 800 MeV/n, typical energies used in hadrontherapy and relevant for space radioprotection. They would be fundamental in order to further optimize TPS in hadrontherapy and risk models for space missions.

To fill this gap, the FOOT (FragmentatiOn Of Target) experiment has been conceived with the aim of measuring differential nuclear cross sections of both target and projectile fragments with an uncertainty less than 5%, taking advantage of an inverse kinematic approach for the measurement of target fragments.

The aim of this thesis is the measurement of elemental and angular differential cross sections from experimental data taken at GSI in July 2021, where a beam of  $^{16}O$  at 400 MeV/u impinging on a target of graphite (C) was employed. At first, a Monte Carlo dataset was exploited in order to study track efficiency, background contributions and fragment corrections. Tracks are reconstructed by a Kalman Filter algorithm, for which charge identification was evaluated exploiting the Tof Wall detector. After a MC cross section measured to check the reliability of the analysis strategy, real data of GSI 2021 campaign were processed.

In *Chapter 1*, an overview of the main processes of charged particles interaction with matter is provided. In *Chapter 2*, hadrontherapy and space radioprotection are introduced, underlying the main physical applications and

the experimental results in these fields. In *Chapter 3*, the FOOT experiment is presented, explaining its purposes and the tasks of each subdetector in the electronic setup. In *Chapter 4*, the analysis procedure is described, focusing on the encountered critical aspects. In *Chapter 5*, the cross sections results are reported, both for MC and real datasets. In *Conclusions*, the overall work is resumed and the main results are discussed, in sight of future data takings and analysis.



# Chapter 1

## Charged particles interactions

In this chapter, an overview of the most relevant processes that occur when a charged particle interacts with matter is presented, focusing on those aspects that are critical or important for hadrontherapy and space radioprotection purposes.

The main interactions are *electromagnetic* (EM) and *nuclear*.

### 1.1 Electromagnetic interactions

When a charged particle, such as a proton or a heavier ion, crosses an absorbing medium, the most significant happening processes are:

- *inelastic Coulomb scattering* with atomic electrons, responsible for the main energy loss in the medium;
- *elastic Coulomb scattering* with nuclei, responsible for deviation of the particle from its starting direction.

Their features are described in the following paragraphs.

#### 1.1.1 EM interaction with atomic electrons

From a geometrical point of view, the probability to interact can be considered (see Sec. 1.2) as proportional to the area of the target [1] and, since the diameter of a nucleus ( $R_{nucleus} \sim 10^{-14} m$ ) is much lower than the one of an atom ( $R_{atom} \sim 10^{-10} m$ ), a charged particle interacts much more with electrons of a target rather than with its nuclei.

If the electron is considered at rest and the condition  $m_{projectile} \gg m_{e^-}$  holds, the process can be described simply as an exchange of momentum due to electrostatic Coulomb force from the incoming charged particle to the

nearby electron. The collision could be soft enough that the atomic electron is excited to an external atomic energy level (*excitation*) and de-excited emitting a photon, or hard enough to eject the electron away (*ionization*). Moreover, the charged particle interacts with a lot of electrons during its path inside the medium, so rather than focusing on just a collision, it is better to consider the energy loss in the whole process.

What described so far and its assumptions were modeled by Bohr and fixed by Bethe and Bloch in the so-called quantity *stopping power* [2].

### 1.1.2 The Bethe-Bloch formula

The *stopping power*  $\frac{dE}{dx}$  represents how much energy per unit path has been absorbed by atomic electrons of a medium after a charged particle crossed it and it is measured in  $\frac{\text{MeV}}{\text{cm}}$ ; to focus on the energy lost by the projectile, it is sufficient to put a minus sign. The formula is the following:

$$-\frac{dE}{dx} = 4\pi N_A r_e^2 m_e c^2 \frac{Z\rho}{A} \frac{z^2}{\beta^2} \left( \ln \frac{2m_e c^2 \beta^2 \gamma^2}{I} - \beta^2 - \frac{\delta(\gamma)}{2} - \frac{C}{Z} \right) \quad (1.1)$$

where  $N_A$  is the Avogadro Number,  $r_e$ ,  $m_e$  are respectively the classical radius and the mass at rest of the electron,  $c$  is the speed of light and  $4\pi N_A r_e^2 m_e c^2$  is a constant of the value of  $0.3071 \frac{\text{MeV cm}^2}{\text{g}}$ ;  $Z$ ,  $A$  and  $\rho$  are respectively the atomic number, the mass number and the density of the target;  $z^2$ ,  $\beta^2$  and  $\gamma$  are respectively the atomic number, the velocity and the Lorentz factor of the charged particle;  $I$  is the mean ionization energy of the target and  $\delta$  and  $C$  are correction factors.

For what concerns the medium dependence, it can be considered quite constant except for the density  $\rho$ . In fact, in a first approximation

- the  $\frac{Z}{A}$  term is close to 0.5 for most of stable nuclei,
- even if the mean ionization energy  $I$  spans in a range from 19 eV for  $H$  to 820 eV for  $Pb$ , its contribution varies negligibly for all the elements because its dependence in the Bethe-Bloch formula is logarithmic,
- only the  $\rho$  term varies of several orders of magnitude.

Thus, in order to focus more on the impinging charged particle rather than on the material, it is possible to introduce the *mass stopping power* defined as follow:

$$\frac{dE}{d\chi} = \frac{1}{\rho} \frac{dE}{dx} \quad (1.2)$$

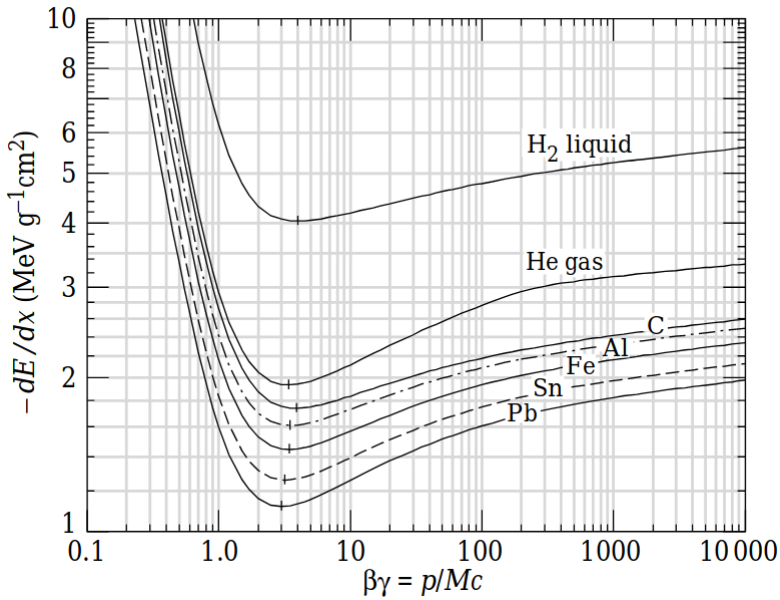


Figure 1.1: Mass stopping power vs  $\beta\gamma$  for different media. For heavy materials (where  $\frac{Z}{A} \sim 0.5$ ) the behaviour is very similar.

which is measured in  $\frac{MeV}{g} cm^2$ . In this way, the radiation has the same effects on a given unit of mass thickness independently from the different medium material density.

The *stopping power* presents a dependence on the velocity of the charged particle  $\beta$ : at low energies it is proportional to  $\frac{1}{\beta^2}$ , it decreases until a minimum value around  $\beta\gamma = 3$  and then there is a logarithmic rise proportional to  $\ln(\beta^2)$  as a consequence of Eq.1.1. The behavior of the *mass stopping power* in terms of the velocity can be seen in Fig. 1.1.

Another important aspect is the dependence on the square of the charge of the incoming particle and not on its mass, which means that different ions would lose different amount of energy, as reported in Fig. 1.2 for an example of particles with  $z=1$  and  $z=2$ .

In hadrontherapy, the energy range of interest is the one where the stopping power is mainly dependent on  $\frac{z^2}{\beta^2}$  [3], which means that the slower is the particle, the higher is the energy released until it stops and the higher is the charge, the more is the energy release in unit of length, as explained in Sec. 2.1.1. In parallel, the mass stopping power is one of the main quantities to focus on in radioprotection, as seen in Sec. 2.2.4.

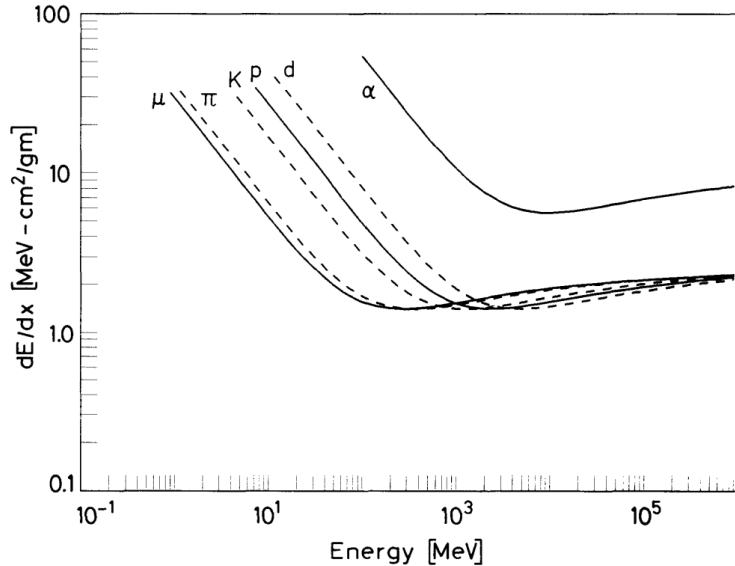


Figure 1.2: Mass stopping power vs energy for different charged particles. The behavior of  $He$  ( $z = 2$ ) is remarkably higher than the remaining particles (all with  $z = 1$ ).

### 1.1.3 Bethe-Bloch corrections

The previous Equation (Eq. 1.1) is a good approximation for  $0.5 < \beta\gamma < 500$ , while for lower or higher values some corrections are needed.

At very low energies, the hypothesis that the atomic electron is at rest falls and the so called *shell correction* holds ( $\frac{C}{Z}$  term in Eq. 1.1): the phenomenological consequence is that the energy loss reaches a maximum and then decreases sharply to 0 when the particle is very close to stop.

Another important correction is due to the *Barkas effect*, according to which electrostatic interaction between the particle and the target changes due to recombination and ionization processes and the effective charge  $z_{eff}$  can be written as:

$$z_{eff} = z(1 - e^{-125\beta(z - \frac{2}{3})}). \quad (1.3)$$

At high energies there is the *density effect* ( $\delta$  term in Eq. 1.1): the stopping power becomes more or less constant because the capability of the particle to interact with nearby electrons decreases as the polarization of crossed atoms increases. This effect depends on the density of the material: the denser the material is, the more the electrons are shielded from the full electric field intensity of the crossing particle.

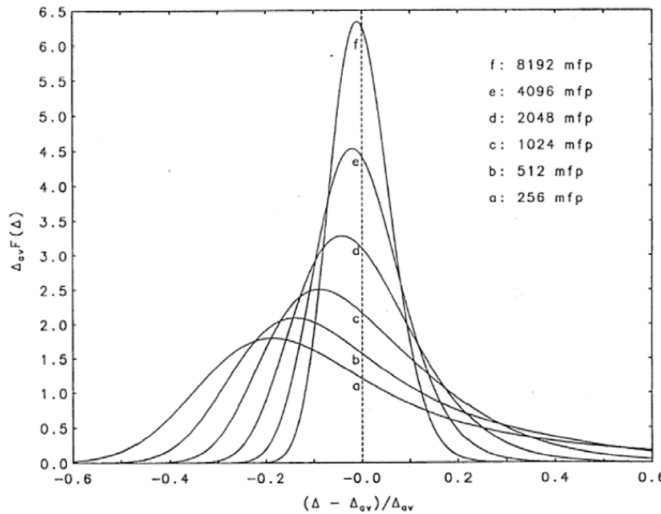


Figure 1.3: Energy loss distribution  $F$  vs its variation with regard to the mean value  $\frac{\Delta - \Delta_{mean}}{\Delta_{mean}}$ . The thickness of the crossed material is described in terms of *mean free path* (*mfp*) of the particle; the higher is the thickness, the higher is the number of collisions and the more the distribution is close to a Gaussian.

### 1.1.4 Energy loss and range uncertainties

The energy loss is the consequence of hundreds of independent interactions between the charged particle and atomic electrons. Since every collision can be different, the stopping power is determined by a stochastic process which suffers of statistical fluctuations [4].

These fluctuations cause the so called *energy loss straggling*, according to which the energy loss is described by the Vavilov distribution (see Fig. 1.3). In the limit of many collisions, it can be approximated to a Gaussian distribution as a consequence of the central limit theorem.

$$f(\Delta E) = \frac{1}{\sqrt{2\pi}\sigma} \exp \frac{-(\Delta E - \overline{\Delta E})^2}{2\sigma^2}. \quad (1.4)$$

Despite the process is statistical, it is possible to define the distance that a charged particle travels in a target material before loosing all its energy. This quantity is called *range* and depends on the type of material, the type of particle, its kinetic energy  $E_k$  and the stopping power  $\frac{dE}{dx}$ :

$$R = \int_0^{E_k} \left( \frac{dE}{dx} \right)^{-1} dE \quad (1.5)$$

The statistical variations of range are referred to as *range straggling*. The quantity defined in Eq. 1.5 is the mean value of a distribution inherited from the one of Eq. 1.4, whose relative standard deviation  $\frac{\sigma_{range}}{R}$  can be derived as follow:

$$\frac{\sigma_{range}}{R} = \frac{f}{\sqrt{m}} \left( \frac{E}{mc^2} \right). \quad (1.6)$$

What emerges is that fluctuations depend on mass and the highest ones are for lighter nuclei.

The main characteristics of the range are important in hadrontherapy in order to improve the positive effects of the treatment and are described in more details in Sec. 2.1.2.

### 1.1.5 EM interaction with nuclei

Another electromagnetic interaction which can happen is the *elastic Coulomb collision* with nuclei of the crossing material, whose main effect is the deflection of the incident particle from the incoming direction. The distribution of the scattering angles is described by the Molière's theory [5] and, in particular, its standard deviation  $\sigma_\theta$  can be derived as follow:

$$\sigma_\theta = \frac{13.6 MeV}{\beta cp} z \sqrt{\frac{x}{X_0}} \left[ 1 + 0.038 \ln \left( \frac{x}{X_0} \right) \right] \quad (1.7)$$

where  $\beta$  and  $z$  are respectively the momentum and the charge of the projectile and  $\frac{x}{X_0}$  is the absorber material thickness in units of radiation length.

An important consideration inspecting Eq. 1.7 is that the lighter is the incoming particle at a fixed energy, the larger would be the lateral spread of its deflection.

Both range and EM straggling are challenging concerns for the selectivity of hadrontherapy and are discussed in Sec. 2.1.3.

Furthermore, it is also possible that an *inelastic Coulomb collision* with nuclei happens. In this case, generally the nucleus is excited and then de-excited with emission of radiation ( $\gamma$  rays).

## 1.2 Nuclear interactions

Even if electromagnetic interactions are the main source for energy loss in a medium, it is not possible to neglect the contribution of *nuclear interactions*, whose effects are of great importance in hadrontherapy and radio-protection, as will be discussed later.

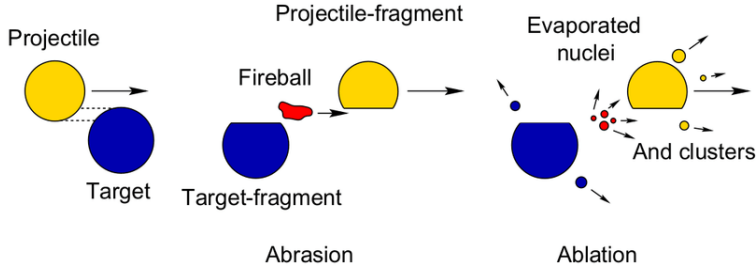


Figure 1.4: Sketch of the abrasion - ablation model.

They are charge-independent short range interactions ( $d \sim 1 \text{ fm}$ ) between nucleons with enough energy to overcome the Coulomb barrier. As for EM interactions, it is possible to distinguish *elastic nuclear collisions*, where there is transfer of projectile energy to the target and *inelastic nuclear collisions* where new particles are produced as a consequence of nuclei structure changes [6].

For the purposes of this work, the latter interactions are the more critical and will be discussed in the following paragraphs.

### 1.2.1 Nuclear fragmentations

At the energy range of hadrontherapy and space radioprotection, the most frequent inelastic nuclear interaction that occurs is *nuclear fragmentation*, that can be explained through the *abrasion-ablation model* [7], illustrated in Fig. 1.4.

Let's suppose to have a heavy target and a projectile; the former is at rest while the latter crosses it. After the collision, there is the “abrasion phase”: the target and the projectile nuclei are fragmented with the emission of an excited state of nucleons called *fire ball* ( $t_{\text{abrasion}} \sim 10^{-22} - 10^{-23} \text{ s}$ ). Subsequently, the nuclei go into thermalisation and de-excitation with emission of light and intermediate mass fragments in the “ablation phase” ( $t_{\text{abrasion}} \sim 10^{-26} - 10^{-28} \text{ s}$ ).

If the projectile energy is high, the interaction can be central with a high production of secondary particles. However, the most common one is the peripheral interaction, with a lower multiplicity of fragments.

The projectile fragments have approximately the same energy per nucleon of the starting particle, but with a lower charge: according to Eq. 1.1 and Eq. 1.5, this implicates that the range of the fragment is higher than the one of the projectile due to the dependence of the stopping power to  $z^2$ . On the other hand, target fragments are generated at very low velocities, so they

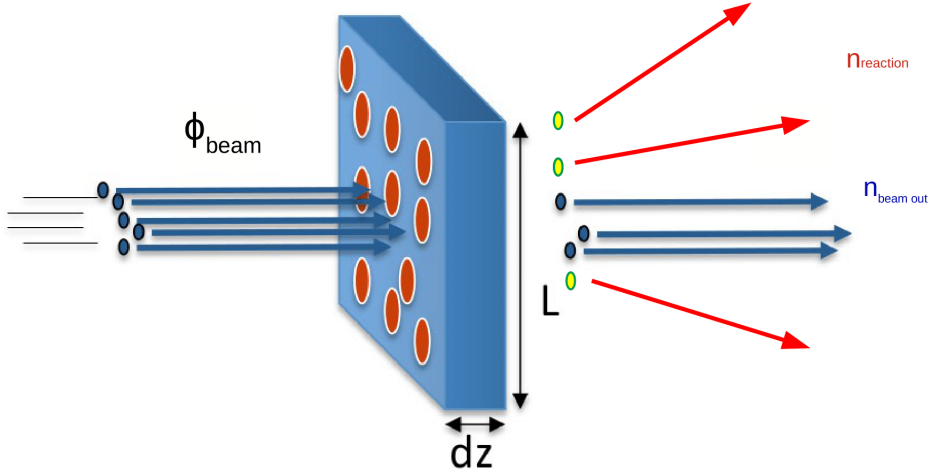


Figure 1.5: Sketch of a cross section measurement.  $\Phi_{beam}$  is the flux of the projectile particles impinging on a target of width  $dz$ , length  $L$  and density  $n_t$ . After the crossing with the target,  $n_{beam\ out}$  particles remain in the beam, while  $n_{reaction}$  ones went into nuclear interaction, of which it is possible to measure the cross section  $\sigma_r$ .

will stop after a very short range of the order of few  $\mu m$ .

Both projectile and target fragments can interact again with the crossed medium but, when dealing with biological matter, the further release of energy can have even collateral effects, as explained in Sec. 2.1.4 for hadron-therapy and Sec. 2.2.4 for space radioprotection.

As a consequence of this, it is fundamental to have an in-depth knowledge of the fragmentation processes and a key parameter for its complete description is the measurement of the *nuclear cross section*.

### 1.2.2 Nuclear cross section

The *cross section* is a quantity that gives a measure of the probability for a reaction to occur and can be described as follows: let's consider a uniform density beam composed of  $N_{beam}$  particles with velocity  $v$  impinging on a target of area  $S$  and differential thickness  $dz$ , as sketched in Fig. 1.5. The incoming flux is:

$$\phi_{beam} = n_{beam} \cdot v$$

which represents the number of beam particles per unit time and unit of surface, where  $n_{beam} = \frac{N_{beam}}{V}$ .

The target particle density is:

$$n_t = \frac{N_A \rho_t}{A_t}$$

where  $N_A$  is the Avogadro number,  $\rho_t$  is the target density and  $A_t$  the target mass number. While the incoming beam crosses the target, some projectile particles are intercepted by it and go into a specific nuclear interaction. The number of particles  $dN_r$  which undergo a nuclear reaction “ $r$ ” in an interval  $dt$  can be obtained:

$$\frac{dN_r}{dt} = \phi_{beam} n_t \sigma_r dV \quad (1.8)$$

where  $dV = S \cdot dz$  is the infinitesimal volume of the target. It is proportional to the flux of the projectile beam  $\phi_{beam}$  and the nuclear density  $n_t$ . The term of proportionality  $\sigma_r$  is exactly the *cross section*[8].

It has the dimension of an area and is measured in *barns* ( $1 b = 10^{-24} \text{ cm}^2$ ) and, as a consequence, it can be considered naively as the superimposed surface of interaction between the projectile and the target, as said in Sec. 1.1.1.

The measurement of a given interaction can happen also in terms of some parameters, such as the kinetic energy or the scattering angle of the produced fragment. In this case the proportional term is the *differential cross section*  $\frac{d\sigma_r}{d\Omega}$  or  $\frac{d\sigma_r}{dE}$  or even the *double differential cross section*  $\frac{d^2\sigma}{d\Omega dE}$  and represents the probability that a specific process “ $r$ ” occurs in the interval  $[\Omega; \Omega + d\Omega]$  or  $[E; E + dE]$  or both. Integrating in all the intervals, it is possible to obtain back the *cross section* of a specific reaction:

$$\sigma_r = \int_0^\Omega \int_0^{E_{max}} \frac{d^2\sigma}{d\Omega dE} d\Omega dE. \quad (1.9)$$

Finally, the sum of results of all the processes gives the *total cross section* of fragmentation:

$$\sigma_{tot} = \sum \sigma_r.$$

### 1.2.3 Empirical models

In Fig.1.6 the total nuclear cross section of  $p - C$  interaction is shown: after a steep increase at low energies, the cross-section follows a plateau quite constant for  $E > \sim 100 \text{ MeV}/n$ . This behaviour is similar also for other nuclear interactions and can be modelled empirically with several methods.

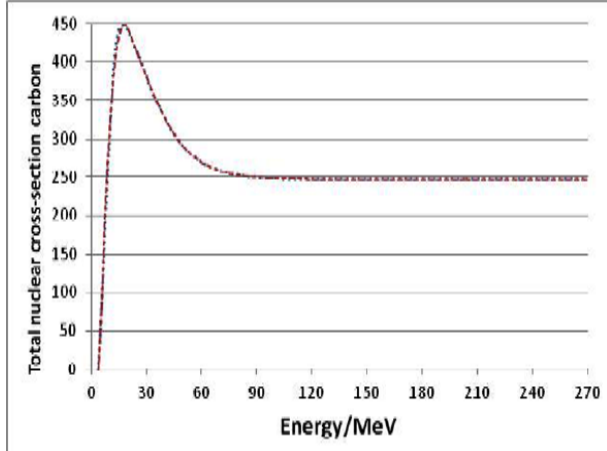


Figure 1.6: Nuclear cross section of p C interaction vs energy

The semiempirical model of the *Bradt-Peters law* [9] considers the interacting particles as spheres according to the liquid drop model and the cross section as a superimposition of the interacting areas:

$$\sigma_r = \pi r_0^2 c_1 (A_p^{1/3} + A_t^{1/3} - b_0)^2 \quad (1.10)$$

where  $r_0 = 1.25\text{ fm}$ ,  $b_0$  and  $c_1$  are parameters and  $A_p$  and  $A_t$  are respectively the mass number of the projectile and the target. It works for  $E > 100\text{ MeV/u}$  and represents the value of the plateau of the cross section after the peak.

Another method considers the nucleons of the projectile and the target starting from the cross section  $\sigma_{pp}$  among protons and  $\sigma_{pn}$  among a proton and a neutron [CITARE]:

$$\sigma_r(Z_p, N_p, Z_t, N_t, E_p) = \pi C(E) \left( \sqrt{Z_p^{2/3} \sigma_{pp} + N_p^{2/3} \sigma_{pn}} + \sqrt{Z_t^{2/3} \sigma_{pp} + N_t^{2/3} \sigma_{pn}} \right)^2 \quad (1.11)$$

where  $C(E)$  is a parameter,  $Z$  and  $N$  are the atomic number and mass atomic number of projectile ( $p$ ) and target ( $n$ ). Its validity is for  $30\text{ MeV} < E < 400\text{ GeV}$  and  $8 < A < 100$ .

# Chapter 2

# Applications

For the purposes of this thesis, the most relevant consequence of charged particle interaction with a target (see Chap.1) is the transfer of a high quantity of energy in the medium: from the biological point of view, this translates into direct or indirect damages to cells that frequently causes their death [10].

These radiation effects on biological matter are at the basis of two opposite applications: on the one hand *hadrontherapy* exploits charged particle interaction with the tumor area of the patient in order to kill cancer cells, while on the other hand *space radio-protection* studies how to limit astronauts health and electronics devices damages due to radiation exposure in space. Both are described in the following paragraphs.

## 2.1 Hadrontherapy

IHadrontherapy is a medical treatment which employs a beam of charged particles to deliver dose to the tumor region of a patient.

The first idea dates back to the 50's of the previous century from the professor R. Wilson and only some years later the first clinical trial accomplished at the Lawrence Berkeley Laboratory, using the experimental cyclotron to produce a beam of protons for medical purposes [11]. From that time on, a lot of improvements were reached by research, as well as very promising results in clinical treatments. For these reasons, many hadrontherapy centers were built worldwide.

As of 2022, there are 114 facilities (with other 36 under constructions) [12], among which two are operating in Italy: CNAO (Centro Nazionale di Adroterapia Oncologica) [13] set in Pavia which provides beam of protons and  $^{12}C$  ions taken by a synchrotron and Centro di Protonterapia in Trento [14] which

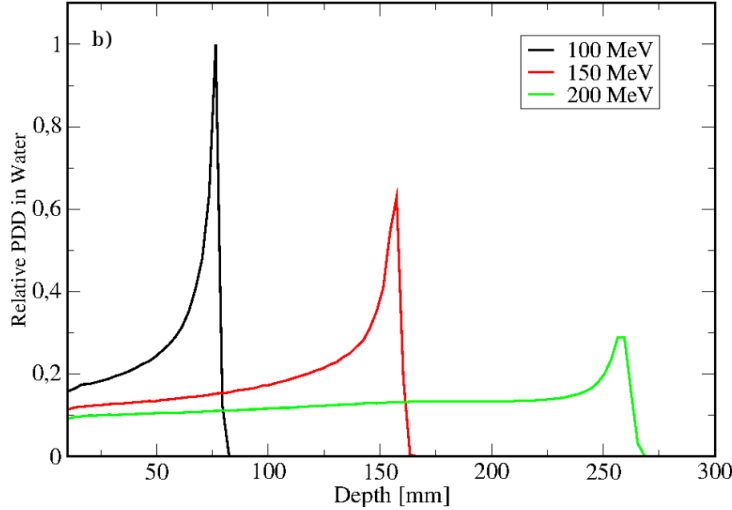


Figure 2.1: Simulation of depth dose profile of protons crossing a water phantom at different energies (100 MeV, 150 MeV and 200 MeV) [16]

exploits proton beams delivered by a cyclotron.

Today only  $p$  and  $^{12}C$  ions are used to treat solid tumours, but other particles such as neutrons,  $He$  and other light ions nuclei (like  $Li$ ,  $O$ , up to  $Si$  ions) have been either used or planned to be used for the future clinical treatments [15].

The main advantage of hadrontherapy relies upon the way energy is released in matter by charged particles, as described in the following paragraphs.

### 2.1.1 Bragg peak

In radiobiology, evaluation of radiation effects in human body is given in terms of *dose*, which is the energy absorbed by the tissue per unit mass:

$$D = \frac{dE}{dm} \quad (2.1)$$

and it is measured in *Gray* ( $1 \text{ Gy} = 1 \frac{\text{J}}{\text{kg}}$ ). For charged particles, the energy absorbed by tissues is very close to the one released by the radiation and it is possible to find a relation between *dose* and *stopping power*:

$$D = \frac{dE}{dm} = \phi \frac{dE/dx}{\rho} \quad (2.2)$$

where  $\phi$  is the *fluence* ( $\frac{\text{protons}}{\text{cm}^2}$ ) and  $\frac{dE/dx}{\rho}$  is the *mass stopping power* ( $\frac{\text{MeV cm}^2}{\text{g}}$ ).

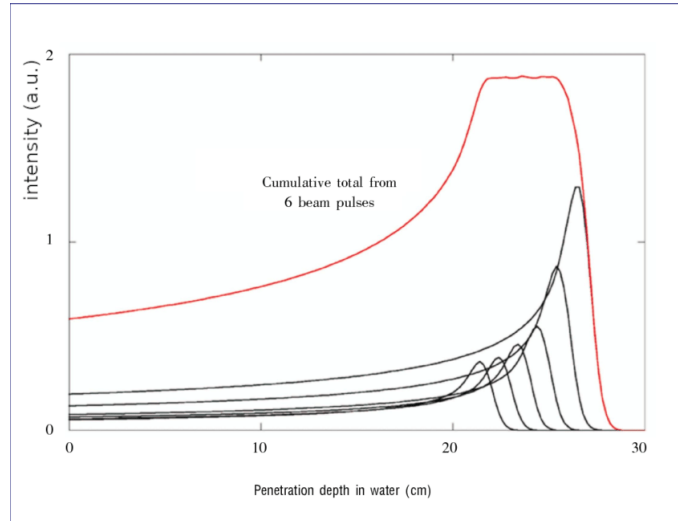


Figure 2.2: SOBP as the overlapping of Bragg peaks of slightly different energy proton beams in water, whose emission intensity is in arbitrary units (a.u.) [17]

The dose released in a medium in terms of crossed path (*depth - dose profile*) for charged particles has a very peculiar behaviour, as seen in Fig. 2.1. Since the *dose* is strictly associated to the *stopping power* (see Sec. 1.1.2), inspecting Eq. 1.1, it is possible to infer that the curve is more or less constant in the entrance channel where  $dE/dx \propto \ln(E)$  and the kinetic energy is still very high. When the energy of the particle decreases enough, the energy loss is proportional to  $dE/dx \propto 1/\beta^2$ , so the *dose* goes very sharply to high values while the particle slows down, until it stops.

Hence, the dose deposition is very localized in the region where the beam is stopped (*Bragg peak*) and it represents the best advantage of hadrontherapy: according to where the tumor is situated, it is possible to deliver a beam of charged particles whose energy is mainly released in a very focused region, sparing healthy tissues nearby.

### 2.1.2 Range and SOBP

The range of a charged particle depends on its kinetic energy (see Sec. 1.1.4) and, starting from Eq. 1.5, it is possible to show that

$$R(E) = \alpha E^p \quad (2.3)$$

where  $E$  is the kinetic energy,  $\alpha$  is a constant which depends on the material and  $p$  is a constant which depends on the energy. For charged particles in

human body, it is approximated as  $R \propto E_0^{1.75}$ .

This is a fundamental property to exploit in hadrontherapy because in order to reach a deeper region in human body, it is sufficient to increase the energy of the beam, which translates into a shift of the *Bragg peak*, as seen in Fig. 2.1.

The typical energy for hadrontherapy beams is of the order of hundreds of MeV: considering the highest depth in human body around 30 cm, the initial kinetic energy for such a range is around  $200\text{MeV}/n$  for  $p$  and  $400\text{MeV}/n$  for  $^{12}\text{C}$  [18], where the difference is due to the fact that heavier ions have a lower range in the same energy unit because Eq. 1.1 infers  $R \propto \frac{A}{z^2}$ .

The Bragg peak has the dimension of some mms, thus, despite it is very localized, it is generally shorter than the longitudinal depth of a tumor, which is of the order of cms. In order to extend the dose released in a certain region, it is applied the so called Spread Out Bragg Peak (SOBP) [19]: changing slightly the energy of the beam, the Bragg peak is shifted and convoluted to a wider region, as seen in Fig. 2.2.

In order to obtain a SOBP, according to the provided accelerator, it is possible to apply a degrader on a fixed energy beam, which is spread on energy and no more monochromatic (with cyclotrons), or just accelerating particles with different energies, obtaining in this way a pulse flux (with synchrotrons) [20].

### 2.1.3 Straggling

Even if the finite range is important for the high physical selectivity of hadrontherapy, range uncertainties are a real problem. As explained in Sec. 2.1.2, even a slight variation of energy causes the shift of the Bragg peak and, in terms of treatment, this conceives an undershooting of the tumor and an overdosing of healthy tissues, as seen in Fig. 2.3 [21].

On the one hand, the longitudinal displacement of the range is the consequence of the statistical fluctuation due to Bethe-Bloch, as described in Eq. 1.3 and Eq. 1.5. In particular, for a beam of  $p$  at the energy of  $200\text{ MeV}/n$ , the straggling is about 2.5 mm for a tumor at depth of 30 cm.

On the other hand, even elastic Coulomb scattering is affected by fluctuations which influence the lateral displacement of the beam, as described in Eq. 1.6. For a  $p$  beam of  $200\text{ MeV}/n$ , the lateral straggling would be of the order of 5 mm.

Since these collateral effects are present, it is fundamental to know the processes of interaction of charged particle with matter as best as possible, in order to limit the risk factor of the treatment [22].

Supposing that the physics-related uncertainties are reduced as much as

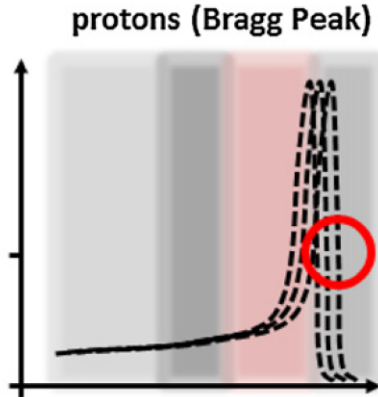


Figure 2.3: Effects of range uncertainties on dose profile: the peak can move causing undershooting of the tumor (red area) and overdosing of healthy tissues (grey area) or viceversa.

possible, there are even other sources of range variations during the clinical treatment, such as patient position, organ motions, uncertainties in definition of the planned treatment and so on. A way to take them under control is to exploit the dose released by the beam not only for therapy, but also for *in vivo range monitoring*, for example by the activity of the secondary fragments. This technique is under research [23] but first promising clinical results were obtained by several experiments, among which the INFN INSPIRE [24][25].

#### 2.1.4 The impact of nuclear fragmentation

The conventional *radiotherapy* is based on the tumor irradiation with a beam of  $\gamma$ -rays which interact with matter distinctively from charged particles: photons have an exponential attenuation and so a release of energy in all the crossed material, while charged particles have a finite range with the highest amount of dose released in the *Bragg peak*, as seen in Fig. 2.4. These are some reasons why hadrontherapy is preferable to the traditional one, however there are also some critical aspects it is important to consider, such as the fact that charged particles can also undergo nuclear interactions. For example, inspecting the Bragg peaks of  $p$  and  $^{12}C$  on Fig. 2.4, it is possible to see that the latter is thinner due to the mass dependence according to the Eq.1.6 but also that there is a tail of dose released after it. This is a consequence of nuclear fragmentation (see Sec. 1.2.1):

- $^{12}C$  ions can undergo nuclear fragmentation while crossing the biological matter. They generate projectile fragments which travel more than

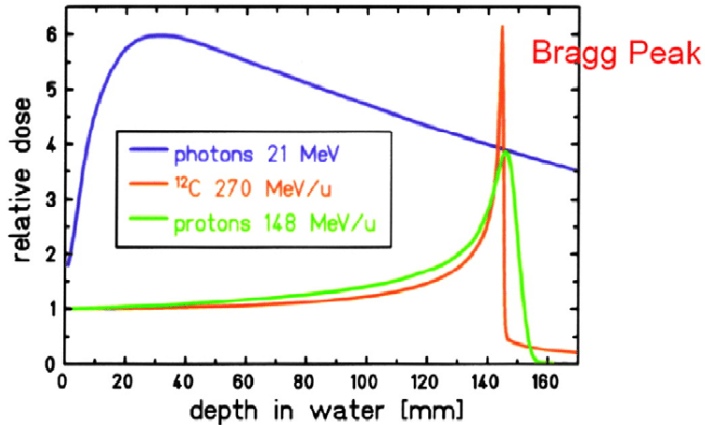


Figure 2.4: depth-dose profile for photons and charged particles.

$^{12}C$  ions (see Sec. 1.2.1) and go beyond the Bragg peak, causing the presence of the above mentioned tail in the dose profile.

- On the other hand, protons undergo only in target fragmentation at the energies of hadrontherapy. This explains the absence of the tail after the Bragg Peak, because target fragments have a very short range.

In other words: the heavier the ion, the sharper the Bragg Peak and the wider the tail after it .

A release of dose after the Bragg peak due to projectile fragments is damaging for the healthy tissues beyond the tumor. Nevertheless, target fragments absorption by biological matter through all the path cannot be neglected in terms of effects [26]: that's why having a deep knowledge of nuclear interactions is fundamental.

## 2.2 Radioprotection in space

In the last decades, interest in space missions is growing more and more and several governative and commercial space agencies are planning long travels in the next future. In particular, NASA's goal is to send humans to Mars within 2030 [27].

Even if the most important requirements are faced promisingly in terms of technological, medical and psychological challenges [28], a lot of work needs to be done on what concerns deep space radiation exposure. In fact, outside

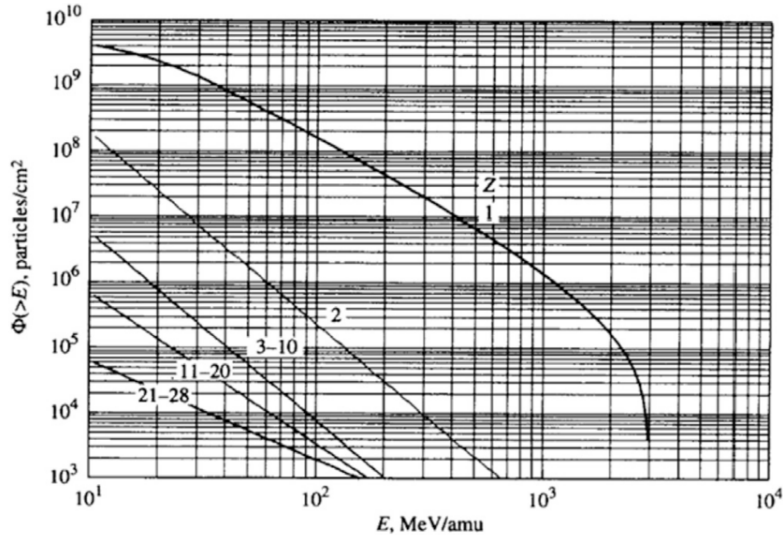


Figure 2.5: Integrated fluence spectra of SPE solar wind of September 29, 1989 [31]

the Earth's atmosphere and magnetic fields, isotropic fluxes of charged particles at high energy are present and exposition of humans and electronics to them can cause irreparable risks.

These effects are the consequence of energy transfer during charged particles interaction with matter as described in Chap. 1 and so they are the same exploited in hadrontherapy. That's why space radiation protection and particle therapy researches share the same tools, devices and main topics [29].

In the next paragraphs, the main sources of radiation in space and the rationale for a passive shielding are described.

### 2.2.1 Geomagnetically trapped particles

Within the magnetic field of the Earth, charged particles (mainly protons and electrons) are trapped in the so called *Van Allen belts*, not uniform regions which extend up to 19000 km far from the magnetosphere . Electrons reach energies up to 10 MeV and protons between 30 keV to 500 MeV [30]. These belts can be crossed quickly by deep space mission spacecrafts, so risks concern mainly human missions or satellites in Low Earth Orbit (LEO).

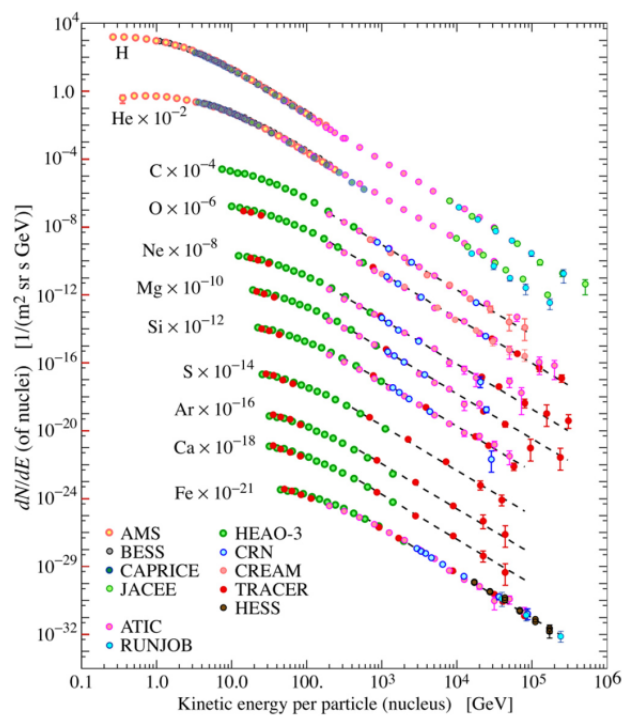


Figure 2.6: The flux of nuclei from Ref. [32]

### 2.2.2 Solar particle events (SPEs)

Among electromagnetic radiation, the Sun continuously emits a particle flux made mainly of protons and electrons called *solar wind*. However, the energies are lower than  $keV$ , so negligible in terms of space radiation risks. The most concerning SPEs are the ones emitted during *solar flares*, local outbursts on the Sun surface where a large amount of energy is released [33]. Despite these processes are very rare, particles are accelerated up to the  $GeV$  region (see Fig. 2.5) and the biological consequences on human beings can be very harmful.

### 2.2.3 Galactic cosmic rays (GCRs)

Another important source of radiation is given by GCRs, originated by astrophysical environments inside and outside the galaxy. As seen in Fig. 2.6, the energy spectrum of emitted particles spans for several orders of magnitude and the element abundance is composed of 85 % of protons, 14 % of helium and about 1% heavier nuclei. The particles with an energy up to  $10^{18} eV$  have an isotropic flux because they are bent by the magnetic field of the galaxy, while the higher energy ones may be anisotropic [34]. However, despite the flux decreases for heavier elements, their contribution in terms of energy loss is high due to the dependence of the stopping power to  $z^2$  ( see Eq. 1.1) and thus GCRs represent a significant hazard for humans in space for their critical biological effects at high energies.

### 2.2.4 Shielding

Radioprotection principles are based on 3 main points: increasing the distance from the source, reducing the time of exposure and applying radiation shielding [35]. In deep space scenario, SPEs and GCRs have isotropic fluxes so the distance is irrelevant, while limiting time is a problem to the scope of long space missions. Thus, the only aspect to focus on is passive shielding for external radiation.

As studied in Chap. 1, the main interactions of charged particles with matter are inelastic Coulomb scattering (described by Bethe-Bloch formula in Sec. 1.1.2) and nuclear fragmentation (described by abrasion-ablation model in Sec. 1.2.1) so the most efficient shielding material would be the one able to stop a high-energy charged particle in the shortest path possible and to limit damages due to nuclear fragmentation.

Regarding the stopping power of the material, it is possible to infer from Eq.

1.1 that:

$$\frac{dE}{d\chi} \propto \frac{Z_t}{A_t} \quad (2.4)$$

where  $\frac{dE}{d\chi}$  is the *mass stopping power* ( $MeVg/cm^2$ ) and  $Z_t$ ,  $A_t$  are respectively the atomic number and mass number of the target particle.

Moreover, regarding the fragmentation, evaluating the nuclear cross section per unit mass recalling Eq. 1.11 implicates:

$$\sigma_{mass} = \frac{N_a \sigma_R}{A_t} \propto A_t^{-1/3} \quad (2.5)$$

where  $\sigma_{mass}$  is the mass nuclear cross section ( $cm^2/g$ ),  $\frac{N_a}{A_t}$  is the number of targets per unit mass and  $A_t$  is mass number of the target particle. If the shielding material is made of light elements (low  $A_t$ ), the former equation implies an high stopping power, so a high release of energy in a short unit of mass thickness (hopefully within the one of the material). In parallel, as a consequence of the latter equation, the probability of nuclear interaction is increased too but the generated light fragments are of less biological significance than the incident ion [36]. As a conclusion, the most ideal radiation shielding material is the one with lighter nuclei.

The best choices would be an electron plasma or liquid hydrogen but their containment in a spacecraft is currently too difficult, while high density polyethylene (HDPE) is a good compromise for its chemical composition (i.e.,  $C_2H_4$ ), followed by liquid water [37]. Up to now, spacecrafts are mainly build with aluminum hulls and, according to nuclear fragmentation models, a mass thickness of  $20 g cm^{-2}$  is enough to break up the majority of incident ions, as shown in Table 2.1 [38] where the percentage of fragmentation in *Al* is reported.

Ion	$5 g cm^{-2}$ Al	$10 g cm^{-2}$ Al	$20 g cm^{-2}$ Al	$40 g cm^{-2}$ Al
$^{12}C$	0.128	0.240	0.423	0.667
$^{16}O$	0.141	0.261	0.455	0.702
$^{24}Mg$	0.160	0.295	0.503	0.753
$^{28}Si$	0.169	0.309	0.522	0.772
$^{56}Fe$	0.213	0.381	0.617	0.853

Table 2.1: Calculated attenuation percentage of high-energy ions by fragmentation in aluminum using geometric cross sections.

In order to evaluate damages on human health, at first, it is fundamental to know the transport and interaction of charged particles (SPEs or GCRs) with shielding material. A lot of different models are used: deterministic ones

using transport equations such as HZETRN developed by NASA, as well as Monte Carlo ones where geometries and way of scattering are simulated, like PLANETOCOSMICS developed by ESA [39].

## 2.3 Experimental cross sections

All the empirical models described in Sec. 1.2.3 and Sec. ?? are refined starting from real data but, in the range of hadrontherapy and space radioprotection (between hundreds of *MeV* and *GeV*), the experimental panorama is poor. This implicates wide uncertainties (around 10%) and discrepancies between the model and real cases. Thus, experiments of fragmentation nuclear cross section in these ranges are needed.

### 2.3.1 Hadrontherapy experiments

The human body is made mainly of four elements [40]: hydrogen, carbon, oxygen and nitrogen. As a consequence, to simulate therapeutic beam interactions with the patient, collisions of proton or heavier ion beams with carbon and hydrogen target are generally studied.

The first attempt of selection of nuclear cross section data was given by P. Schwaller et Al. in [41], where proton total cross-sections measured at CERN in the energy range between 180 *MeV* to 560 *MeV* are reported, as seen in Fig.2.7.

A great deal of experimental nuclear reaction measurements are collected in dedicated data libraries, where it is possible to filter only the ones of interest in hadrontherapy, for example nuclear reactions involving light nuclei with  $A < 20$  and with beam energies up to 250 *MeV/n*.

One of the main dataset used for this purpose is EXFOR [42], a worldwide co-operation library which contains more than 17.000 works about neutrons, photons and charged particles induced reactions. Of similar importance is the Landolt–Börnstein dataset, a collection of data in several scientific fields among which particles and nuclear reactions published by Springer Nature[43] and the Particle Data Group (PDG) dataset[44] for hadron interactions.

However, the aforementioned datasets can lack of experimental data in specific ranges and this limitation can be overcome using libraries of data ex-

trapolated by different theoretical models, such as ICRU[45] and TALYS[46] which consists of a vast number of state-of-the-art nuclear-reaction models or INCL[47], which is a dynamical Monte Carlo model like INCL[47].

In Fig. 2.8 and Fig. 2.9 the target cross section of  $p$  against  $^{12}C$  are respectively shown. The only cases in which the energy range is equally covered is for the production of  $^7Be$  and  $^{11}C$  due to the fact that they have been well studied as important isotopes for PET diagnostic technique.

Carbon beams reactions were studied in several experiments. A special mention needs to be done for the one performed at GANIL[48], where angular differential fragmentation cross sections of  $^{12}C$  at 95 MeV/u on thin targets have been measured (see Fig. 2.10). Another important experiment was the one performed at INFN-LNS[49], for the measurement of the  $^{12}C$  fragmentation at 62 MeV/n (see Fig. 2.11 and Fig. 2.12). Recently, the most complete results were obtained by the FIRST[50] experiment, measuring differential cross sections in energy and angular distribution of  $^{12}C$  impinging on a gold target (see Fig. 2.13 and 2.14).

### 2.3.2 Space Radioprotection experiments

Despite cosmic rays particles have an energy range from MeV to  $10^9$  TeV, the peak of the spectrum is between hundreds of MeV to GeV, with a composition of  $p$  for 98% and heavier ions up to  $^{56}Fe$  for 2%. As a consequence, nuclear cross sections for medium-light fragments (from H to Ni) at the aforementioned energy range are important to characterize cosmic radiation.

A comprehensive data collection was generated by Norbury et al. [51] where charge changing, elemental and isotopic cross-sections of several projectiles and targets with reference to specific angles and energies are reported. In Fig. 2.15, the total cross section for the production of  $^1H$  with different target and projectile is shown.

More recent is the data collection presented as a collaboration between GSI, ESA and NASA [52][53], where experimentally measured total nucleus nucleus reaction cross sections are systematically compared with theoretical models. Cross sections of  $^4He$ ,  $^{12}C$ ,  $^{56}Fe$  are reported in Fig. 2.16.

### 2.3.3 General considerations

What emerges from the cited studies is that there is a lack of data in the specific energy range of interest for both hadrontherapy and space radioprotection and an evident discrepancy between real data and models. Moreover,

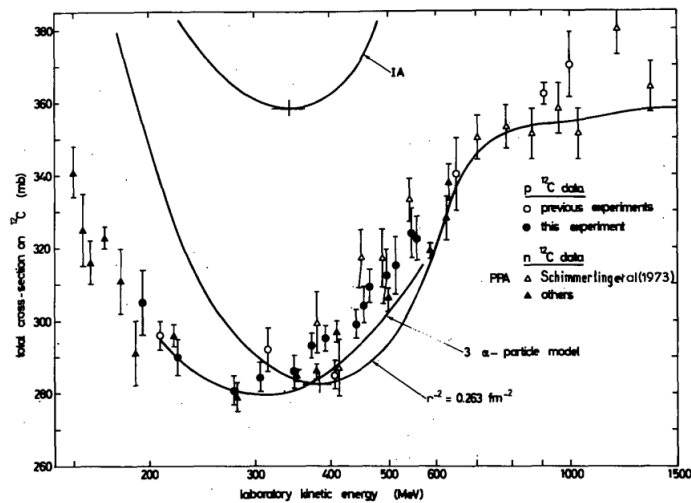


Figure 2.7: Total cross sections of protons ( $\circ$ ) and neutrons ( $\triangle$ ) on  ${}^{12}C$  compared to theoretical predictions

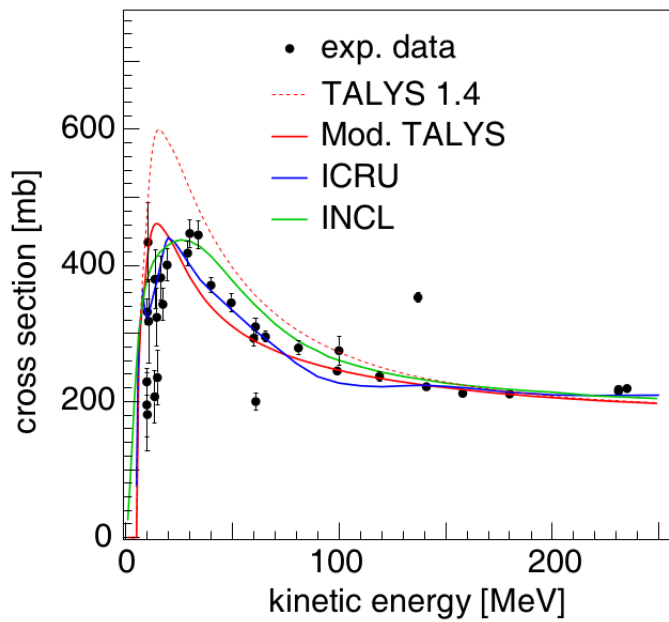


Figure 2.8:  $p + {}^{12}C$  reaction cross section. Experimental data are drawn from the EXFOR database and are represented by black dots; results of TALYS 1.4 (dashed red), Modified TALYS (solid red), ICRU (solid blue) and INCL (solid green) are also shown.

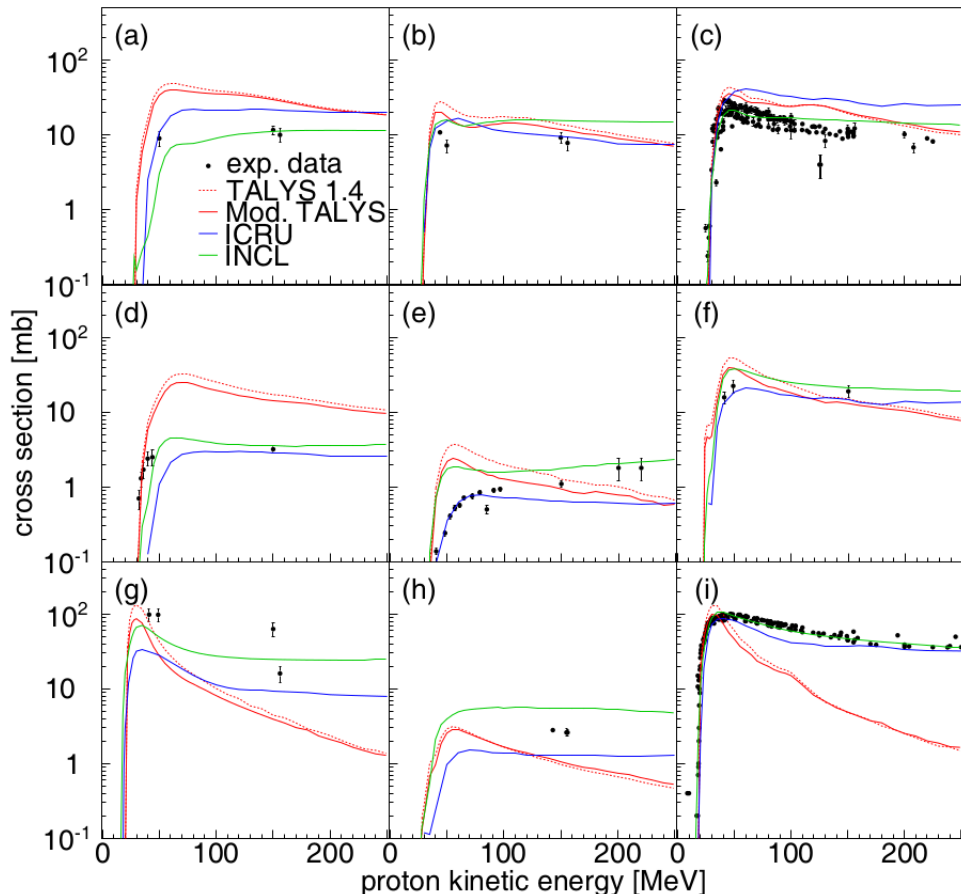


Figure 2.9: From  $p + {}^{12}C$  reaction, cross section production for (a)  ${}^6Li$ , (b)  ${}^7Li$ , (c)  ${}^7Be$ , (d)  ${}^9Be$ , (e)  ${}^{10}Be$ , (f)  ${}^{10}B$ , (g)  ${}^{11}B$ , (h)  ${}^{10}C$  and (i)  ${}^{11}C$ . Experimental data are taken from Landolt–Bornstein dataset and are represented by black dots; results of TALYS 1.4 (dashed red), Modified TALYS (solid red), ICRU (solid blue) and INCL (solid green) are also shown.

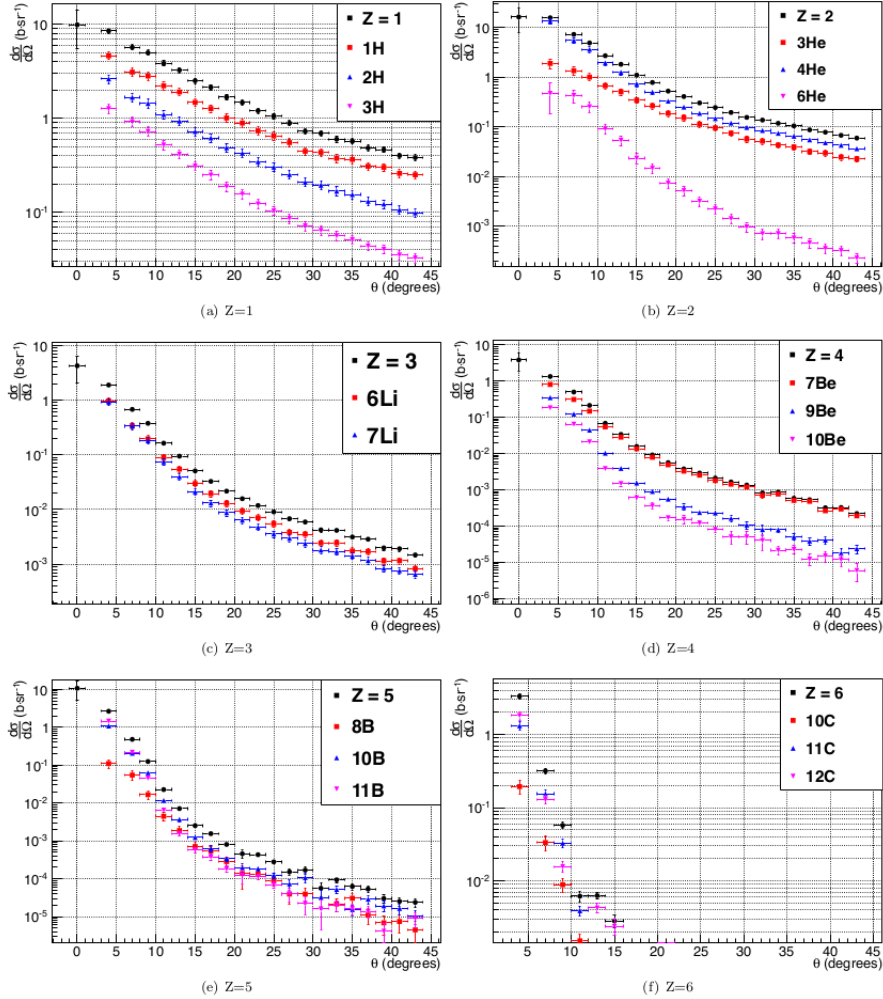


Figure 2.10: Angular distributions for fragments resulting from the fragmentation of  $^{12}\text{C}$  on carbon target. The distributions of the different isotopes are superimposed.

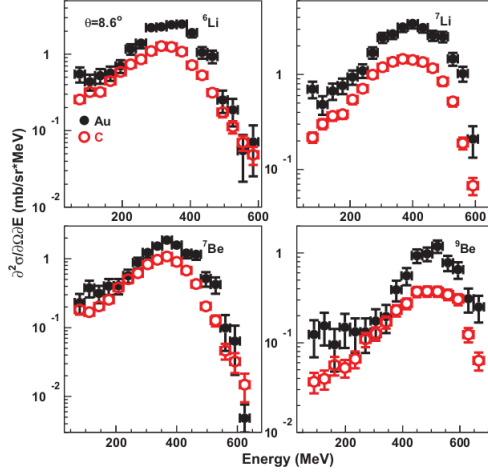


Figure 2.11: Double differential cross sections measured at  $\theta_{lab} = 8.6^\circ$  for the production of  ${}^6\text{Li}$ ,  ${}^7\text{Li}$ ,  ${}^7\text{Be}$  and  ${}^9\text{Be}$  in the  ${}^{12}\text{C} + {}^{197}\text{Au}$  ( $\bullet$ ) and  ${}^{12}\text{C} + {}^{12}\text{C}$  ( $\circ$ ) reactions at 62 MeV/n.

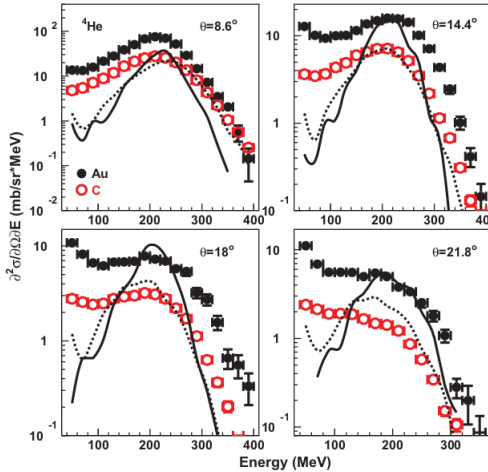


Figure 2.12: Double differential cross sections measured at  $\theta_{lab} = 8.6^\circ$ ,  $14.4^\circ$ ,  $18^\circ$  and  $21.8^\circ$  for the  ${}^4\text{He}$  production in the  ${}^{12}\text{C} + {}^{197}\text{Au}$  ( $\bullet$ ) and  ${}^{12}\text{C} + {}^{12}\text{C}$  ( $\circ$ ) reactions at 62 MeV/n. Prediction by INCL (dashed line) is also shown.

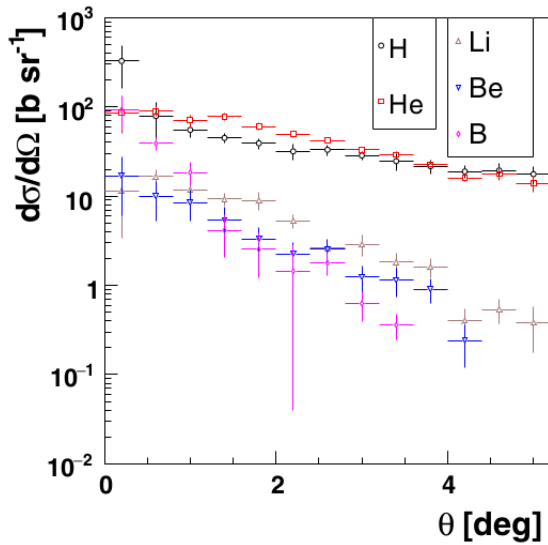


Figure 2.13: Angular differential Cross section of different fragments with respect to the ion incoming direction.

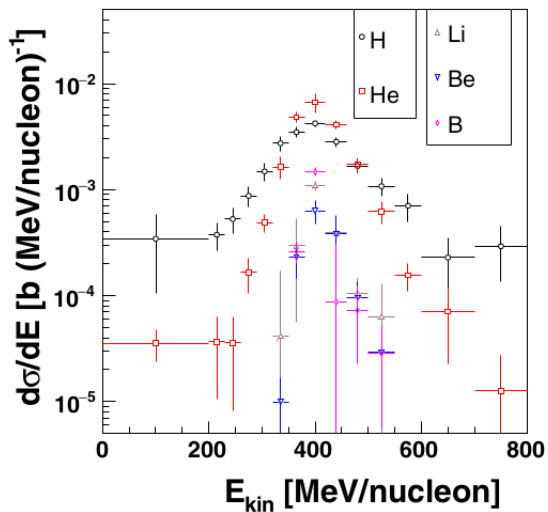


Figure 2.14: Energy differential Cross section of different fragments with respect to the ion incoming direction.

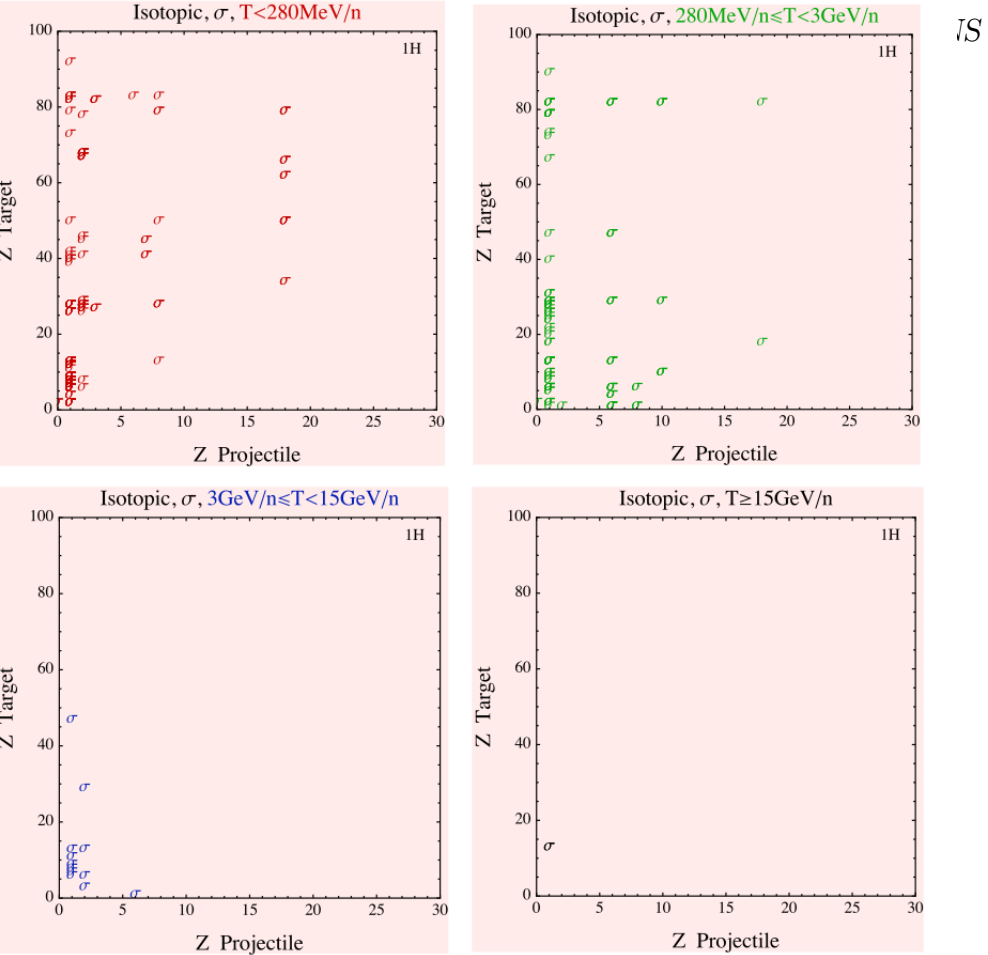


Figure 2.15: Isotopic total cross-sections for  ${}^1H$  fragments. "σ" presents the measurement of a proton fragment generated with the combination of a specific target and projectile. The energy regions will be  $T < 280\text{MeV}/n$  (below the pion threshold),  $280\text{MeV}/n < T < 3\text{GeV}/n$  (low energy),  $3\text{GeV}/n < T < 15\text{GeV}/n$  (medium energy),  $T > 15\text{GeV}/n$  (high energy).

where present, cross sections are partial (differential in angle or in kinetic energy, never in both variables together) and only with reference to the initial energy of the beam, instead of the fragment energy itself.

To overcome the described issues, the current results are not enough and new measurements are needed. In particular, double differential nuclear cross sections with respect to the fragment angular distribution and energy spectra need to be taken for both light and medium ions in the energy range of hadrontherapy (from 100 MeV/n to 400 MeV/n for p,He,C,O mainly) and space radioprotection (up to 800 MeV/n for elements from p to Fe). This is the main goal of the FOOT experiment (see Sec. 3).

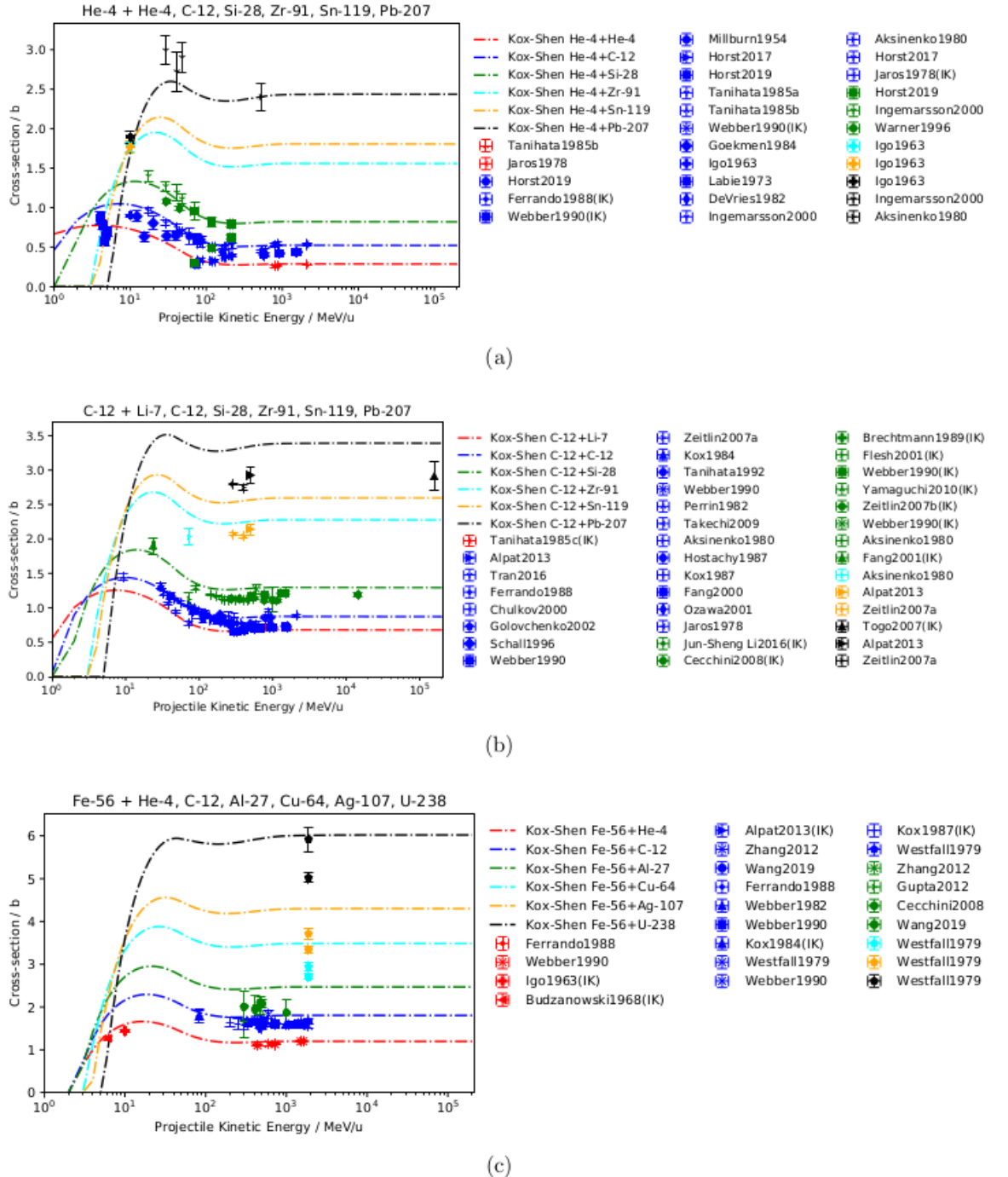


Figure 2.16: Data collections for  ${}^4He$ ,  ${}^{12}C$  and  ${}^{56}Fe$  projectiles on different targets. Dots are experimental data taken from different experiments, lines are model predictions.

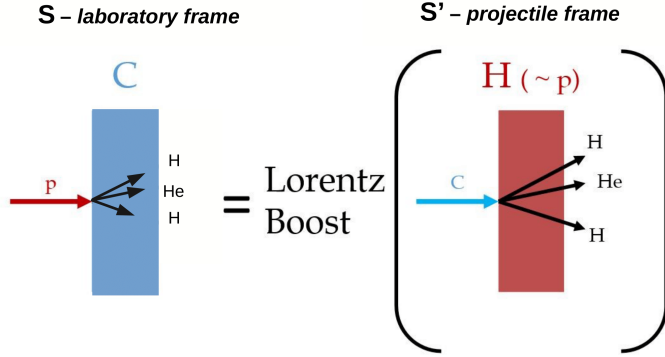


Figure 2.17: (a) and (b) !! to be modified

### 2.3.4 Inverse kinematics

All the experimental results described up to now give information about the projectile fragment cross section. As said in Section 1.2.1, they have a range wide enough to escape far from the target and to be detected by the experimental setup.

However, hadrontherapy and space radioprotection applications demand for a good knowledge even of target fragments, the ones which stop in a very little range, because their effects are not negligible. It is not possible to study these fragments directly because they are absorbed by the target without any possibility to be detected. A way to proceed is then to study the target fragments indirectly applying the theoretical approach of *Inverse Kinematics*.

Let's suppose to be in the relativistic frame  $S$  (*laboratory frame*) where a projectile proton  $p$  impinges on a heavy target  $t$  with velocity  $\beta$  on the positive axis  $z$ . If nuclear fragmentation occurs, in hadrontherapy energy range, it generates only target fragments with a very short range (see Fig. (a)). Instead, it is possible to consider a relativistic frame  $S'$  (*projectile frame*) where the projectile  $p$  is at rest and the target  $t$  moves toward it with a velocity  $-\beta$ . The fragments generated are obviously the same as in the frame  $S$  but here they would have enough energy to escape (see Fig. (b)) and so to be detected.

To study the fragments of the target, the idea is then to analyze  $t \rightarrow p$  (*projectile frame*) rather than  $p \rightarrow t$  (*laboratory frame*) and go back with the mathematical approach of (*inverse kinematics*), which consists of a Lorentz transformation.

Let's consider a generic four-vector  $\mathbf{A}$  in the *laboratory frame S*:

$$\mathbf{A} = (a_t, \vec{a})$$

where  $a_t$  is the temporal coordinate and  $\vec{a}$  the spatial vector. The Lorentz transformation of  $\mathbf{A}$  from  $S$  into  $\mathbf{A}'$  of  $S'$  can be written as:

$$\mathbf{A}' = \Lambda \mathbf{A}$$

where  $\Lambda$  is a 4x4 matrix.

In the case described before, the transformation happens only in the z direction maintaining constant the value of the velocity. As a consequence, the transformation can be expressed as follows:

$$\begin{pmatrix} a'_t \\ a'_x \\ a'_y \\ a'_z \end{pmatrix} = \begin{pmatrix} \gamma & 0 & 0 & -\beta\gamma \\ 0 & 1 & 0 & 0 \\ 0 & 0 & 1 & 0 \\ -\beta\gamma & 0 & 0 & \gamma \end{pmatrix} \cdot \begin{pmatrix} a_t \\ a_x \\ a_y \\ a_z \end{pmatrix} = \begin{pmatrix} \gamma a_t - \beta\gamma a_z \\ a_x \\ a_y \\ -\beta\gamma a_t + \gamma a_z \end{pmatrix} \quad (2.6)$$

where  $\beta$  is the velocity in z direction and  $\gamma = \sqrt{1 - \beta^2}$ . It can be demonstrated that  $\Lambda^{-1}(\beta) = \Lambda(-\beta)$ , which implicates that the inverse transformation is:

$$\begin{pmatrix} a_t \\ a_x \\ a_y \\ a_z \end{pmatrix} = \begin{pmatrix} \gamma & 0 & 0 & \beta\gamma \\ 0 & 1 & 0 & 0 \\ 0 & 0 & 1 & 0 \\ \beta\gamma & 0 & 0 & \gamma \end{pmatrix} \cdot \begin{pmatrix} a'_t \\ a'_x \\ a'_y \\ a'_z \end{pmatrix} = \begin{pmatrix} \gamma a_t - \beta\gamma a_z \\ a_x \\ a_y \\ -\beta\gamma a_t + \gamma a_z \end{pmatrix} \quad (2.7)$$

Replacing the generic four-vector  $\mathbf{A}$  with the space-time one  $\mathbf{S} = (ct, x, y, z)$  or momentum-energy one  $\mathbf{P} = (E/c, p_x, p_y, p_z)$ , it is possible to obtain the kinematic information in the needed reference frame, and consequently the needed cross section.

This technique allows to overcome the problem of short range target fragments and is used in the FOOT experiment, as explained in Sec. 3.1.



# Chapter 3

## The FOOT experiment

The FOOT (FragmentatiOn Of Target) experiment was funded by INFN (Istituto Nazionale di Fisica Nucleare) in 2017 and currently it consists of more than 100 collaborators dislocated between ten INFN italian sections and several foreign universities and research institutes.

The goal of the experiment is the measurement of differential nuclear cross sections in order to fill the gaps in experimental data collections in the energy range of hadrontherapy and space radioprotection interest. The results would be, in fact, fundamental to optimize the hadrontherapy treatment planning systems, a software which computes the expected dose distribution in the patient's tissue starting from a simulation of the interactions of the beam in the human body (see Sec. 2.1.4). As well, it is of unavoidable importance to enhance the reliability of the computational models for what concerns space radiation effects, focusing on astronauts and space craft electronics risks in long time travels out of the Earth's atmosphere (see Sec. 2.2.4).

Nevertheless the apparatus configuration is currently under optimization, first results were already collected in several facilities, among which CNAO (Centro Nazionale di Adroterapia Oncologia) in Pavia, HIT in Heidelberg and GSI in Darmstadt in Germany. Data takings with the complete configuration of the experiment are foreseen within 2024.

In the next sections, the FOOT experiment motivations and research program are introduced, followed by a description of the experimental setup.

### 3.1 The goal and experimental requirements

The final goal of the FOOT experiment is to measure target differential cross sections in energy ( $d\sigma/dE_{kin}$ ) with an accuracy better than 10% and projectile double differential cross section in energy and angle ( $d^2\sigma/(d\Omega dE_{kin})$ )

with an accuracy better than 5%, in the energy range of hadrontherapy (between 150 MeV/n and 400 MeV/n) and space radioprotection (up to 800 MeV/n).

It is a fixed target experiment in which beams of protons (or of heavier ions like  $^4He$ ,  $^{12}C$ ,  $^{16}O$ ) are shot against a target containing H, C or O to simulate what happens during the beam-human interaction. The measurement of the target cross section can be achieved applying the *inverse kinematic* approach (details in Sec. 2.3.4).

In order to retrieve differential cross section in terms of a specific element, up to now composite targets like polyethylene ( $C_2H_4$ ) and graphite (C) are used, where the results concerning for example only hydrogen cross section can be obtained subtracting respectively the cross section of graphite to the one of polyethylene, as shown in the following formula [48]:

$$\sigma(H) = \frac{1}{4}(\sigma(C_2H_4) - 2\sigma(C)).$$

The same process can be used even for differential cross sections and for other elements and materials, like PMMA (polymethyl methacrylate, chemical formula  $C_5O_2H_8$ ) to retrieve cross section of Oxygen or  $Al_2O_3$  for what concerns Aluminium, currently used for space crafts. However, the cross section obtained by target subtraction is affected by an uncertainty which is the quadratic sum of the ones of the separated targets so, in order to prevent large errors, very precise measurements are needed.

To achieve the mentioned requirements on cross section measurements in both direct and inverse kinematic, high performances in terms of charge and isotopic identification capability of fragments are needed, in particular [54]:

- $\sigma(p)/p$  at level of 4 - 5 %
- $\sigma(T_{tof})$  at level of 100 ps
- $\sigma(E_{kin})/E_{kin}$  at level of 1 - 2 %
- $\sigma(\Delta E)/\Delta E$  at level of 5 %

where  $p$  is the momentum,  $T_{tof}$  is the Time of Flight ,  $E_{kin}$  is the kinetic energy and  $\Delta E$  is the total energy deposition of the fragment in the detector.

In the following section, the design criteria of the experimental setup are described.

## 3.2 Design criteria

In order to design and optimize the detector, a MonteCarlo simulation of a  $^{16}O$  beam of  $200 \text{ MeV}/n$  impinging a target of  $C_2H_4$  was computed and the results in terms of fragments angular and kinetic energy distributions are shown in Fig. 3.1. It is possible to see that "heavy" fragments ( $Z > 2$ ) are peaked with an angular distribution around  $1^\circ$  and almost fully contained below  $10^\circ$ , while the kinetic energy distribution is peaked around the primary beam value. On the other hand, it is possible to notice that light particles have wider distributions. This is an important aspect to consider for the design of the experiment for what concerns the geometrical acceptance.

Another requirement of the FOOT experiment is its portability, in order to succeed data takings in different experimental rooms in research centers spread out in different places. For this reason, size and weights of detectors are also other criteria to consider for the experiment design.

Finally, the overall material budget close to the active detection area has to be minimized in order to limit multiple scattering of the beam and further fragmentation.

In order to match the mentioned requirements and performances, the FOOT experiment is organized in two alternative setups:

- an electronic setup based on a magnetic spectrometer for track reconstruction and particle identification optimized for  $Z \geq 3$  particles with an angular acceptance of  $\sim 10^\circ$  with respect to the beam axis
- an emulsion chamber spectrometer for identification of fragments with  $Z \leq 2$  and an angular acceptance up to  $\sim 70^\circ$

The electronic setup description is provided in the next sections, while the emulsion apparatus is discussed in [55].

## 3.3 Electronic detector setup

The preliminary step of a cross section measurement is the univocal fragment charge and isotopic reconstruction for particle identification (PID). To achieve this goal, the FOOT electronic setup has been designed exploiting PID techniques. In particular:

- the charge  $Z$  of the fragments can be identified from energy loss  $\Delta E$  and  $TOF$  starting from the Bethe-Bloch formula (Eq. 1.1) given by a scintillator detector and a silicon microstrip apparatus.

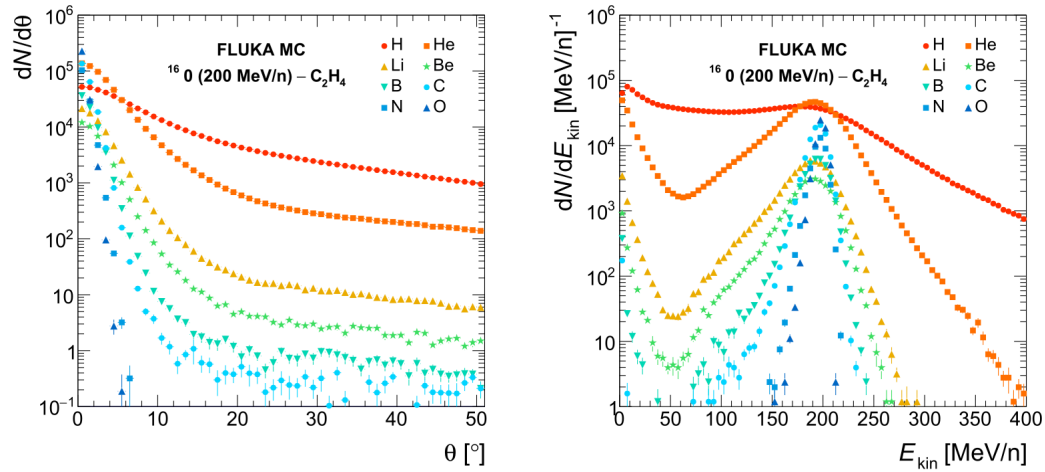


Figure 3.1: Angular (left) and kinetic energy (right) distribution of fragments produced by 200 MeV/n beam of  $^{16}\text{O}$  against a target of  $\text{C}_2\text{H}_4$

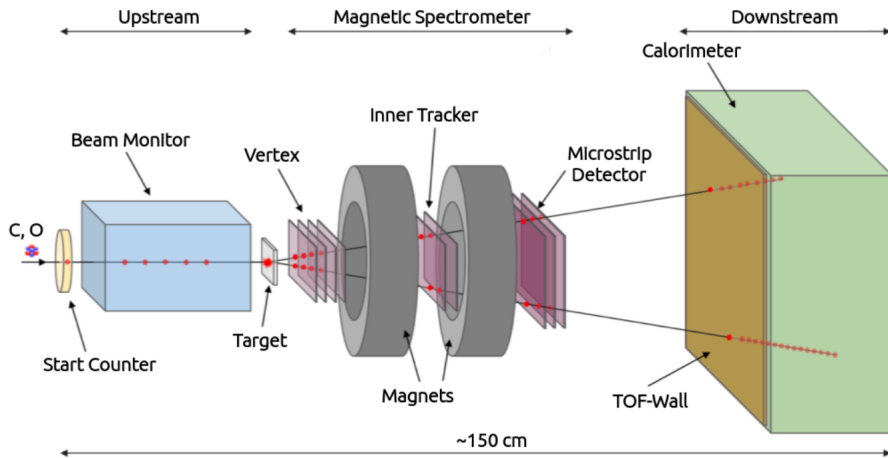


Figure 3.2: Schematic representation of the FOOT experimental setup (from [56])

- the momentum  $p$  can be measured by a magnetic spectrometer formed by three different types of silicon detectors by tracking reconstruction
- the kinetic energy  $E_k$  information is provided by a calorimeter. Putting together  $E_k$ ,  $p$  and  $TOF$ , three methods for the mass reconstruction are obtained:

$$p = m\beta\gamma \quad (3.1)$$

$$E_k = mc^2(\gamma - 1) \quad (3.2)$$

$$E_k = \sqrt{p^2c^2 + m^2c^4} - mc^2 \quad (3.3)$$

where  $\gamma = 1/\sqrt{1 - \beta^2}$

For description purposes, the experimental setup can be divided into three main regions: an upstream region, a tracking region and a downstream region, as shown in Fig. 3.2.

### 3.3.1 Upstream region

The *upstream region* is a pre-target region finalized to the monitoring of the beam before impinging with the target and it consists of two detectors: a thin plastic scintillator (namely Start Counter) and a drift chamber (namely Beam Monitor).

#### Start Counter

The Start Counter (SC) is made by a thin squared foil of EJ-228 plastic scintillator [57] with a thickness of  $250 \mu m$  and an active surface of  $5 \times 5 cm^2$ , enough to cover the transversal size of the beam. It is held by an aluminium structure and covered by a 3D printed black box in order to reduce external light background, as seen in Fig. 3.3 (a). The scintillation light produced in the detector is collected by 48  $3 \times 3 mm^2$  SiPMs [58], 12 per side, bundled in eight electronic channels. The readout and powering is handled by the WaveDAQ system [59].

The aims of SC are several: providing the Minimum Bias trigger, measuring the incoming ion flux and providing the start time for the  $TOF$  measurement. The SC time resolution is of the order of 50 ps, according to latest results.

#### Beam Monitor

The Beam Monitor (BM) is a drift chamber filled with a 80/20% gas mixture of Ar/CO<sub>2</sub> operating at  $\sim 0.9$  bar (see Fig. 3.3). It consists of

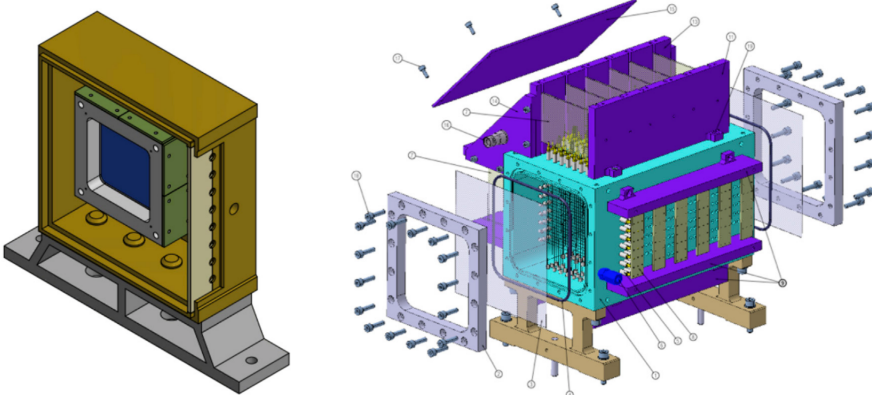


Figure 3.3: Schematic representation of the Start Counter inside the plastic box (left) and of the Beam Monitor (right)[54].

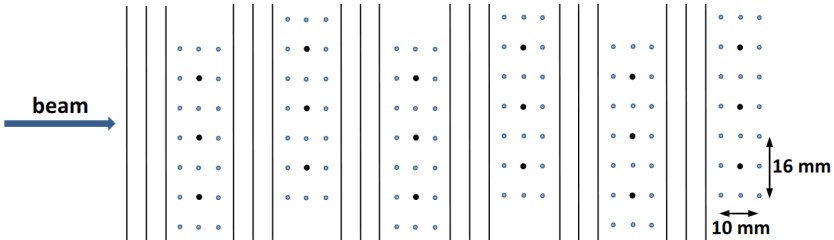


Figure 3.4: Schematic representation of the Beam Monitor cells layout [60].

12 wire layers, with three cells per layer of transversal shape  $16 \times 10 \text{ mm}^2$ . Plane layers oriented along x and y axes are alternated and consecutive ones are staggered by half a cell, allowing the beam profile reconstruction limiting ambiguities [60], as sketched in Fig. 3.4. The total dimensions are  $11 \times 11 \times 21 \text{ cm}^3$ .

The BM is positioned between the SC and the target, with the aim to measure the direction and the interaction point of the incoming beam, fundamental for particle tracking and inverse kinematic transformation. It is also used to discard pre-target fragmentation and to address pile-up ambiguity in the tracking devices. The spatial resolution of  $100 \mu\text{m}$  implies a track direction reconstruction with an accuracy of few  $\text{mrad}$ , needed for a good resolution in particle identification. Moreover, the monitoring performed by BM is also important to measure the real event rate of the beam because the standard ones set by the facilities suffer generally of fluctuations.

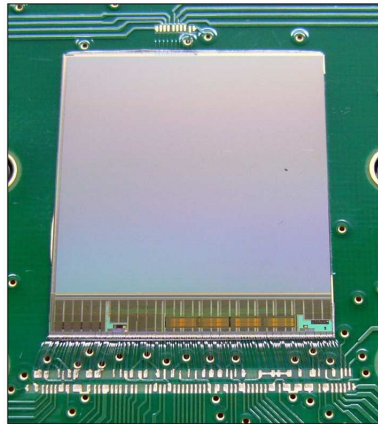


Figure 3.5: Picture of a M28 chip.

### 3.3.2 Tracking Region

The *tracking region* of the FOOT setup is composed by the target and a magnetic spectrometer, which consists of two permanent magnets, two stations of pixel and one of strip detectors: the vertex detector (VTX), the inner tracker (IT) and the microstrip detector (MSD). The main aim of this region is reconstruction of the track of the fragments through which it is possible to retrieve the momentum information, the correct path length of the particle and associating the correct energy deposits in other sub-detectors.

#### Vertex detector

The Vertex detector is situated after the target and before the first magnet, with the aim to identify the starting point of the track of the fragment. It is organized in four layers of a single MIMOSA-28 (M28) sensors based on CMOS Monolithic Active Pixel Sensors (MAPS) technology. Every sensor is made of a matrix with 928 (rows)  $\times$  960 (columns) pixels of  $20.7 \mu m$  pitch, for an overall chip total size of  $20.22 \text{ mm} \times 22.71 \text{ mm}$  and  $50 \mu m$  of thickness, showed in Fig. 3.5.

The detector guarantees a geometrical acceptance of  $40^\circ$  and a spatial resolution of  $5 \mu m$  [61], fulfilling the requirements of low material budget and high precision and efficiency.

#### Inner tracker

The Inner Tracker is made of two planes of pixel sensors between the two magnets, with the aim to provide tracking of the fragments in the magnetic

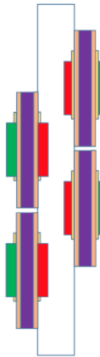


Figure 3.6: Sketch of the inner tracker, made of two planes of 4 ladders of M28 sensors each.

region. Every layer has a sensitive area of  $8 \times 8 \text{ cm}^2$  and a total of 16 M28 sensors. In order to fit the required acceptance, granularity and tracking performances, the pixel sensors are organized in ladders, each of which is made of two modules of four M28 sensors glued on both faces of a support structure of silicon carbide (SiC) 2 mm of thick. Then, every module hosts 4 M28 sensors, for a total of 4 ladders per layer staggered to increase acceptance due to sensor electronic and structure, as shown in Fig. 3.6. M28 sensors are negligibly affected by the residual magnetic field of the fragments [62].

### Micro Strip Detector

The Micro Strip detector is the tracking station positioned downwards the magnets, fundamental to measure the momentum and to match the track reconstructed in the magnetic spectrometer with the particle hits in the following detectors, the ToF Wall and the Calorimeter. It consists of 3 planes, each of which has an active area of  $9.6 \times 9.3 \text{ cm}^2$  and it is formed by two perpendicular Single-Sided Silicon Detector (SSSD). Every silicon sensor has a thickness of  $50 \mu\text{m}$  to minimize further fragmentation and a readout pitch of  $150 \mu\text{m}$  for a spatial resolution lower than  $40 \mu\text{m}$ .

It provides also to measure  $dE/dx$  for Z identification, an information that can be used in comparison with the more precise one of the ToF Wall.

### Magnets

The central part of the magnetic spectrometer is made by two magnets that bend the trajectory of the charged fragments produced in the target allowing for momentum measurement.

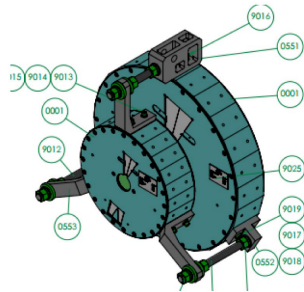


Figure 3.7: Sketch of the two magnets assembled in a mechanical structure.

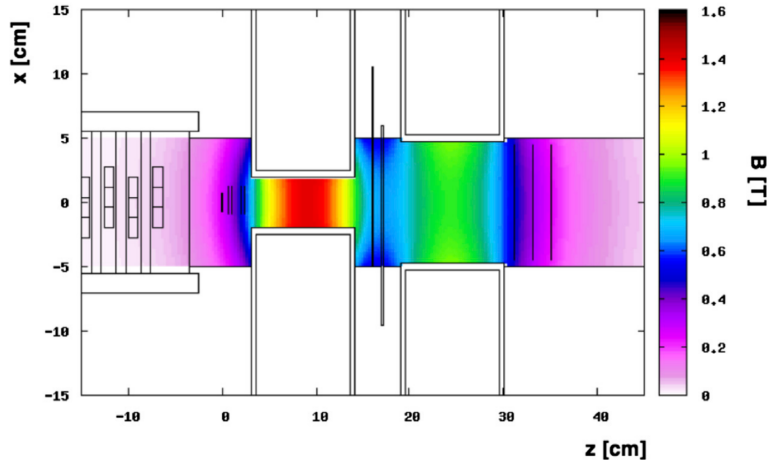


Figure 3.8: Computed magnetic field map of the two magnets in Halbach configuration, where the magnetic field intensity is referred to its y axis.

To guarantee portability and to reach the requested resolutions, they are two compact permanent magnets in a Halbach configuration. The two magnets are cylindrical in shape with an internal diameter of 5 cm and 10.6 cm respectively (see Fig. 3.7). The map of the magnetic field is simulated in Fig. 3.8 and allows to obtain a spatial intrinsic accuracy of  $10 \mu m$ . Moreover it is possible to infer that the intensity of the  $B$  field is high in the internal cylindrical hole ( $1.4$  T and  $0.9$  T) and decreases fast from the cavities, being relevant only in the region between the silicon detectors.

Each magnet is made of 12 units of Samarium-Cobalt, a robust material which maintain the magnetic field constant even in a high radiation environment.

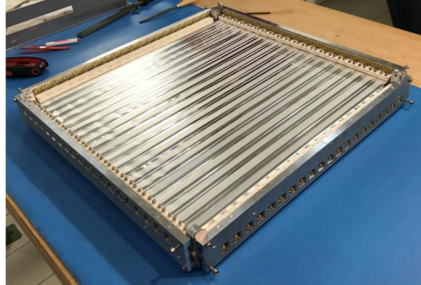


Figure 3.9: Picture of the mounted ToF Wall

### 3.3.3 Downstream Region

The *Downstream Region* is the last part of the FOOT electronic setup, located at least 1 m away from the target and made of two main component: a plastic scintillator (namely ToF Wall) to measure the energy loss and the stop time of the ToF and a Calorimeter for the kinetic energy measurement.

#### ToF Wall

The ToF Wall detector is composed by two orthogonal layers of 20 plastic scintillator bars with an active area of  $40 \times 40 \text{ cm}^2$ . Every bar is 0.3 cm thick and with a trasversal size of 2 cm  $\times$  44 cm (see Fig. 3.9). The granularity has been choosen in order to limit as much as possible the pile-up of particles in the same bar and the thickness is a trade-off between a high scintillation and a low secondary fragmentation. This detector extract time and charge information of the fragment.

Every bar is coupled at the edges to 4 SiPM with a  $3 \times 3$  active area and a pitch of  $25 \mu\text{m}$ .

The two side readout allow the measurement of the energy loss  $dE/dx$ , the final time information for the *ToF* measurement and the hit position for the track reconstruction. According to the FOOT requirements, the time resolution is of the order of 100 ps and the energy loss one is lower than 5% for fragments heavier than *He* [63], while the precision in the hit position is lower than 8 mm.

#### Calorimeter

The calorimeter is the last detector of the setup with the aim to absorbe completely the fragment in order to measure its kinetic energy, fundamental for the mass reconstruction. It will be composed of 320  $\text{Bi}_4\text{Ge}_3\text{O}_{12}$  (BGO) crystals divided in  $3 \times 3$  modules in a spherical shell arrangement of 20 cm of

radius. Each crystal has a truncated pyramid shape, with a length of 24 cm and a front and back size of  $2 \times 2\text{cm}^2$  and  $3 \times 3\text{cm}^2$  repectively. The BGO material has been chosen for its high light yield ( 10 photon/keV) and high density ( $\rho = 7.13\text{g/cm}^3$ ), suitable with the FOOT environment where speed response requirements are negligible.

Every crystal is coupled to a matrix of 25 SiPM with an active surface of  $2 \times 2\text{ cm}^2$  and a single sensor pitch of  $15\text{ }\mu\text{m}$ . At high energies ( $\sim 700\text{MeV/n}$  for the space radioprotection contest), the interactions that happen inside the calorimeter are not only due to electromagnetic scattering, so even hadronic showers can be produced. As a consequence of this, togheter with the production of neutrons, particles can escape out of the calorimeter causing a systematic error that worsens the energy resolution. The dept of each crystal has been chosen in order to minimize the energy leakage.

### 3.3.4 Future developments

The FOOT apparatus is currently in a partial configuration because some subdetectors are still under development and optimization. In particular, the magnets are under construction and are foreseen to be ready within 2022, while the 320 BGO crystals of the calorimeter will be assembled by the end of 2022. Several beam tests were performed at CNAO and GSI in order to optimize detectors configuration and response, and other are already planned in the next months.

A problem which is still under investigation concerns the fact that a significative quantity of secondary neutrons is produced as a consequence of nuclear fragmentation. They propagate in the FOOT setup and generally escape without interacting, causing a missing energy detection in the calorimeter and thus a bad mass reconstruction. To address this issue and to overcome the lack of neutron cross section results, the FOOT collaboration started the development of dedicated neutron detectors in Bologna that will be added to the current setup [64] in the next future.

Despite the partial configuration, three data takings for physics purposes have already been performed by the FOOT collaboration with electronic setup. The final campaign of data with the overall apparatus is foreseen for 2023 - 2024.



# Chapter 4

## GSI 2021 Analysis

The aim of this thesis is the analysis of data taken at GSI in July 2021 by a partial configuration of the FOOT apparatus, where a beam of  $^{16}O$  impinging on targets of Carbon and Polyethylene respectively was employed. After a description of the FOOT setup, the analysis software is introduced. Finally, the procedure toward a cross section measurement is explained in details and commented.

### 4.1 GSI facility

As mentioned before, GSI is a German research center situated in Darmstadt, equipped with a heavy ion accelerator facility to perform basic and applied research in physics, among which nuclear structure and reactions experiments [65].

The facility is composed by a linear accelerator of 120 meters length followed by a synchrotron with a circumference of 216 meters, able to accelerate a wide range of ions up to close the speed of light, from proton (up to a beam energy of 4.5  $GeV$ ) to Uranium (up to 1000  $MeV/u$ ). The beam emittance goes from  $30 \times 8 \text{ mm} \cdot \text{mrad}$  in fast configuration to  $5 \times 8 \text{ mm} \cdot \text{mrad}$ , in the slow one.

### 4.2 The FOOT setup at GSI 2021 data taking

Measurements were performed by the FOOT experiment at GSI in July 2021 with a partial setup, which involved the Start Counter (SC), the Beam Monitor (BM), the Vertex (VTX), the Micro Strip Detector (MSD), the ToF Wall (TW) and 9 crystals of BGO for the calorimeter (CALO), as reported in Fig. 4.1.

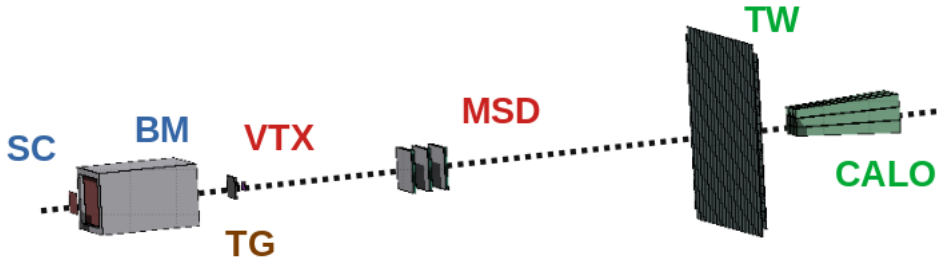


Figure 4.1: Schematic representation of the FOOT electronics setup at GSI 2021

Beams of  $^{16}O$  were employed against targets of graphite (C) and Polyethylene ( $C_6H_6$ ) respectively, with energy of 200 MeV/u and 400 MeV/u, for a total of more than 40 millions events in several configurations.

The absence of the magnets makes the reconstruction of the momentum not possible, while the presence of just a module of calorimeter allows fragment kinetic energy measurements only with a very limited angular acceptance. For the purposes of this thesis, the analysis was focused on data of  $^{16}O$  impinging on a target of graphite (C) and, due to the aforementioned characteristics, the aim is the measurement of elemental totla cross sections and angular differential cross section, where the charge is reconstructed by the TW and the fragmnet direction by the tracking algorithm.

GSI 2021 data and Monte Carlo Simulations with the same parameter setup were processed using SHOE as analysis software, described in the following section.

## 4.3 Analysis software

SHOE (*Software for Hadrontherapy Optimiazion Experiment*) is a software whose final aim is the full reconstruction of both data and simulated events for cross section measurements. It is a C++ object-oriented software, based on the ROOT [66] framework, developed by the FOOT collaboration and stored in the INFN git repository [67].

### 4.3.1 Simulated and real data

Data used as input source by SHOE can be Monte Carlo simulations or acquired data. According to the data type, they have different features.

- Simulated data are obtained by the MC simulator FLUKA [68], used to simulate the passage of particles through matter using nuclear models tuned by real cross sections data. In both cases, after a description of the setup which includes the geometry, the position and the materials for every detector, the MC code generates beam particles' interactions and consequent fragment propagation through the apparatus. This provides physical quantities for every physical object. The results are digitized and stored in a ROOT format file.
- All the subdetectors of the electronic setup of FOOT (see Chap. 3) are managed by a *Trigger and Data Acquisition System* (TDAQ), whose aim is the collection of data following all the steps between the generation of signals in the detectors to their storage on disk. However, since detectors have different architectures, several readout solutions are needed (from standard VME boards to custom FPGAs and specific subdetector software like WAVEDAQ [59]) with the critical task to synchronize data of all the detector in the right way for every event building. Another important aspect is the trigger for the selection of specific events of interest during the data taking and the detector online monitoring during the acquisition, like hardware and software status of sensor temperature. Raw data are stored in a ROOT format file.

### 4.3.2 Reconstruction

The event reconstruction made by the SHOE software is conceived in several steps:

- *Level 0* - The first step of the SHOE reconstruction code is to obtain a common format input source, reading, interpreting and converting MC or real raw data into the same structure ROOT file. At this step, several operations concerning the subdetectors are accomplished, like pixel and strip clusterization and digitization (VTX and MSD), signal processing to obtain ToF and charge information (SC and TW) and position evaluation. Charge reconstruction is reported in Sec. 4.4. For every specific data taking, calibration and parametrization files of every detectors are loaded.
- *Track reconstruction* - A Kalman Filter algorithm provided by GENFIT [69] library is employed to reconstruct the track of every fragment, in order to estimate kinematics parameters like position, direction, momentum and time of flight of a specific particle. A more detailed de-

scription of Kalman algorithm is given in Sec. 4.5. Again, all the results are written in a ROOT format file.

- *High Level* - Once all the physical quantities are estimated or extrapolated in the reconstruction, the analysis can go on with the fragment identification (univocal measurement of the atomic number  $Z$  and mass number  $A$  of a fragment) and all the other steps needed for the final cross section measurement, which are outlined in Sec. 4.6.

### 4.3.3 Cross section software

A Python software was coded with the aim to take in input all the relevant physical quantities reconstructed by SHOE and combine them to obtain as output a cross section measurement. The software is implemented in a flexible way such that the parameters of interest are set dynamically according to the features of the specific input ROOT file: for GSI 2021 data taking charge and angular distribution parameters were used, but the adaptive script can be used successfully even in further data takings where the full experimental setup will be present.

Up to now, the software is able to measure the cross section according to the beam parameters, the events distribution and the efficiency of a given variable also considering background and systematics. However, it is implemented in a way to have the possibility to introduce easily other statistical improvements and new features.

It is updated using the INFN git repository with the future goal to integrate it in SHOE as a fundamental step for analysis purpose.

## 4.4 Fragment identification

Due to the specific setup of GSI 2021, the identification of a particle is strictly connected to its charge, since the mass can be reconstructed only for a little variety of fragments with a low angular aperture.

The particle charge is reconstructed thanks to the information given by SC and TW, namely Time of Flight (TOF) and  $dE/dx$ , which are quantities of Bethe Bloch formula (Eq. 1.1 of Sec. 1.1.2) through which it is possible to retrieve the charge  $z$ .

In SHOE, the charge identification algorithm discriminates a fragment according to the  $dE$  -  $ToF$  graph: as can be seen in Fig. 4.2, a Bethe Bloch curve is computed for every charge (from  $z = 1$  to  $z = 8$  in GSI 2021 campaign) as a function of time. Since Eq. 1.1 depends on  $\frac{1}{\beta^2}$ , it is also proportional to

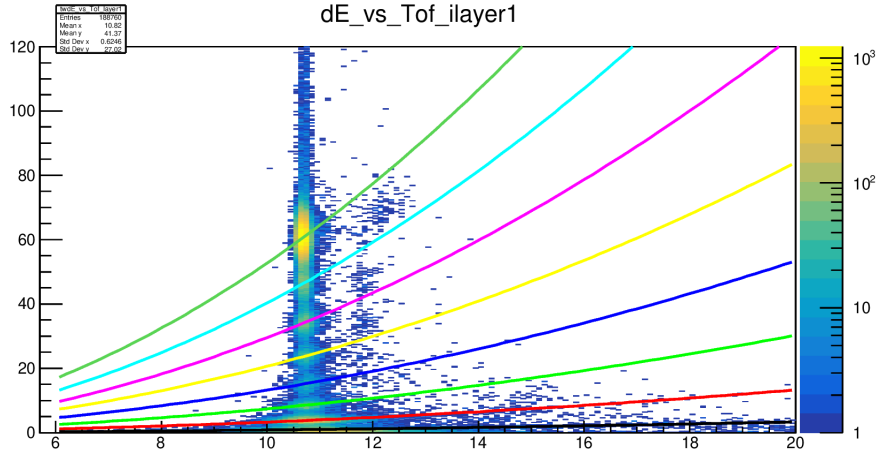


Figure 4.2: Real events of  $^{16}\text{O}$  at 400 MeV/u fragmentation in regions delimited by Bethe Bloch curves according to the charge.

$t^2$ . Every fragment is then described by  $dE$ , the energy released in the TW bars and the ToF, the time taken by the particle to reach the TW from the target and, according to them, it is associated to the charge of the closest curve.

Charge parameter is exploited by the tracking algorithm to reconstruct trajectories, as explained in the following section.

## 4.5 Tracking

Tracking is a the technique through which it is possible to reconstruct the trajectory of a particle as a consequence of its interaction with several detectors. From it, important physical quantities are retrieved as position, direction and momentum. Moreover, it allows to associate TW and CAL energy deposit (and relative detector measured quantities) to trajectories obtained by tracker detectors.

In global tracking methods, the estimation of the physical parameters is done applying a minimization method like the *Maximum Likelihood Method* or the *Least Squares Method*, once all the hits are collected. The one used in the FOOT analysis is instead a progressive method, in which the estimation of the parameters is improved adding hits step by step. It is called *Kalman Filter* and it is more powerful and flexible than classical ones because track parameters are uploaded in an iterative way, improving the fit near the interaction point, as shown in Fig. 4.3.

In the FOOT experiment, the algorithm is implemented in SHOE through the

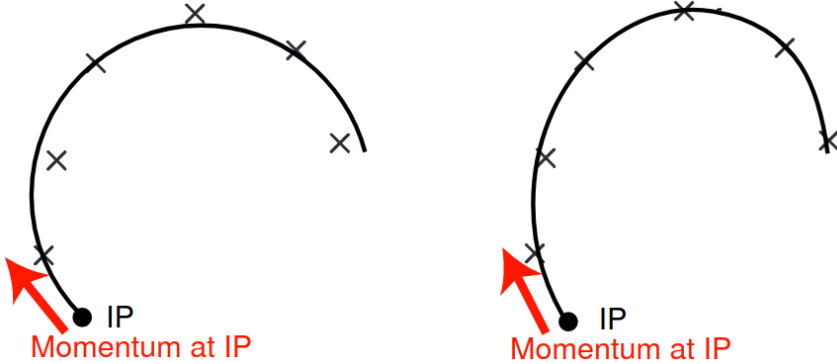


Figure 4.3: (Left) Least square fitting of hits: only one track parameter can be defined. (Right) Kalman fitting of hits: track parameters are defined for every hit. [71].

GENFIT software package, written in a C++ object-oriented design [69]. The track reconstruction is done exploiting the B field generated by the two magnets and the hits in the VTX, the IT and MSD (see Sec.3). Once every point is added, a tracking fit is calculated according to the possible charge of the fragments in the current event, an information obtained as described in Sec. 4.4.

In the specific GSI 2021 campaign, the trajectory can be reconstructed considering the hits in the SC, BM, MSD and TW, as reported in Fig. 4.4. This led to obtain track distributions with reference to charge and angle. However, for the purposes of this analysis, the tracking algorithm was set considering only points of the VTX and of the TW as a first approximation. Moreover, an hand-made procedure to limit the offset of the TW position can be applied as explained in [70].

The theory behind the Kalman Filter algorithm is explained in the next paragraph.

#### 4.5.1 The Kalman Filter

In filtering algorithms, the track of a particle is considered as a dynamic system, described by a state vector  $\bar{x}$  (the line denotes true value). In the framework used in FOOT, the state vector is a 5-dimensional vector which

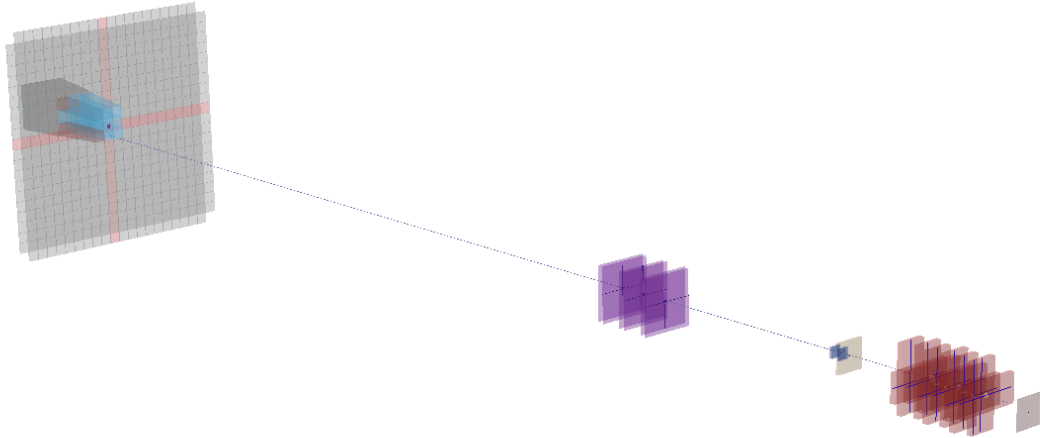


Figure 4.4: Track reconstruction in GSI 2021 setup: the collected points are from the SC, the BM, the MSD, the TW. The reconstructed trajectory is linear due to the absence of the B field.

contains track parametrization in plane coordinates:

$$\bar{\mathbf{x}} = \begin{pmatrix} q/p \\ u' \\ v' \\ u \\ v \end{pmatrix} \quad (4.1)$$

where  $q/p$  is the particle charge over the momentum,  $u'$  and  $v'$  are direction tangents,  $u$  and  $v$  are positions of the detector.

Assuming that the state can be specified at discrete points  $\mathbf{k}$ , which are i.e. the intersection points of the particle with a detector, the evolution of the dynamic system can be described by a differential system equation:

$$\bar{\mathbf{x}}_k = \mathbf{f}_{k-1}(\bar{\mathbf{x}}_{k-1}) + \mathbf{w}_{k-1} \quad (4.2)$$

where  $\mathbf{f}_{k-1}(\bar{\mathbf{x}}_{k-1})$  is a function called *propagator* from point  $\mathbf{k-1}$  to point  $\mathbf{k}$  and  $\mathbf{w}_{k-1}$  is called *process noise* and represents random disturbance of the track from  $\mathbf{k-1}$  to  $\mathbf{k}$ , which in FOOT experiment is given mainly by multiple scattering and energy loss in the crossed path.

The state vector is generally not observed directly but can be obtained by  $\mathbf{m}_k$ , the quantity measured by the detector in  $\mathbf{k}$  position with the following relation:

$$\mathbf{m}_k = \mathbf{h}_k(\bar{\mathbf{x}}_k) + \epsilon_k \quad (4.3)$$

where  $\mathbf{h}_k(\bar{\mathbf{x}}_k)$  is a function called *measure propagator* and  $\epsilon_k$  represents the noise of the process.

Given  $\mathbf{C}_k$  the covariant matrix of  $\bar{\mathbf{x}}_k$ ,  $\mathbf{Q}_k$  and  $\mathbf{V}_k$  respectively the covariant matrixes of process and measurement noise  $\bar{\mathbf{w}}_k$  and  $\bar{\epsilon}_k$ , the Kalman filter is an efficient recursive algorithm that finds the optimum estimate  $\tilde{\mathbf{x}}_k$  (tilde stands for estimate) for the unknown true state vector  $\bar{\mathbf{x}}$  of a system from a series of noisy measurements [72]. The main steps are *prediction*, *filtering* and *smoothing*.

## Prediction

The *prediction* step consists of propagating a state vector from a point  $k - 1$  to point  $k$  and it is written as  $\mathbf{x}_{k-1}^k$ , while the predicted covariance  $\mathbf{C}_{k-1}$  is extrapolated by means of multiple scattering and energy loss. In particular:

$$\tilde{\mathbf{x}}_{k-1}^k = \mathbf{f}_{k-1}(\bar{\mathbf{x}}_{k-1}) \quad (4.4)$$

## Filtering

In the *filtering* step, the predicted state  $\tilde{\mathbf{x}}_{k-1}^k$  is updated considering the information at point  $k$  given by the measurement state  $\mathbf{m}_k$ .

It is useful to introduce the *residual*:

$$\tilde{\mathbf{r}}_k = \mathbf{m}_k - \mathbf{H}_k \tilde{\mathbf{x}}_k \quad (4.5)$$

where  $\mathbf{H}_k = \frac{\partial \mathbf{h}_k}{\partial \mathbf{x}_{k-1}^k}$  is called *projector matrix*.

It is possible to compute  $\chi^2$  between the predicted and measured state at the point  $k$ :

$$\chi_k^2 = \mathbf{r}_k^T (\mathbf{V}_k - \mathbf{H}_k \mathbf{C}_k \mathbf{H}_k^T)^{-1} \mathbf{r}_k \quad (4.6)$$

and, minimizing it with respect to  $\mathbf{x}_k$ , the update state vector becomes:

$$\tilde{\mathbf{x}}_k = \tilde{\mathbf{x}}_{k-1}^k + \mathbf{K}_k (\mathbf{m}_k - \mathbf{h}_k(\tilde{\mathbf{x}}_k^{k-1})) \quad (4.7)$$

where  $\mathbf{K}_k = \mathbf{C}_k \mathbf{H}_k \mathbf{G}_k$  is the *Kalman Gain Matrix*, which states how much the measurement suits the predicted state vector. An intuitive sketch of prediction and filtering steps is given in Fig. 4.5.

## Smoothing

Once the filtering process has done for all the points of a given system *forward* from  $k = 0$  to  $k = n$ , it is possible to refine estimates of previous states going *backward* from  $k = n$  to  $k = 0$ , processing all the given data. Thus,

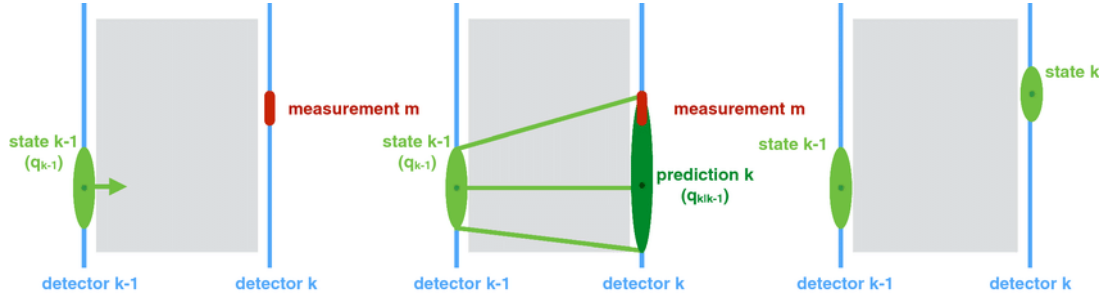


Figure 4.5: (Left) Let's suppose to have a particle crossing two detectors at position  $k - 1$  and  $k$ . The state vector  $\mathbf{x}_{k-1}$  at the position  $k - 1$  is described as a green ellipse, while the measurement at position  $k$  is indicated in red. (Center) A prediction is made for the state vector on the  $k$ th surface and the size of the prediction is indicated with the dark green ellipse. (Right) The state vector on the  $k^{\text{th}}$  surface is updated by including the measurement on the  $k$ th surface applying filtering [73].

the *smoothing* step can be considered as filtering in the opposite direction, in light of all observations:

$$\tilde{\mathbf{x}}_k^n = \mathbf{x}_k + \mathbf{A}_k (\tilde{\mathbf{x}}_{k+1}^n - \tilde{\mathbf{x}}_{k+1}^k) \quad (4.8)$$

where  $\mathbf{A}_k = \mathbf{C}_k \mathbf{F}_k (\mathbf{C}_{k+1}^k)^{-1}$  is the *smoothed gain matrix* and  $\mathbf{F}_k = \frac{\partial \mathbf{f}_k}{\partial \mathbf{x}_{k-1}}$  is the *propagator matrix* [74].

What described so far works good for linear systems, however it can be extended even to non-linear ones (*Extended Kalman Filter*) where non-linearities are approximated using e.g. Taylor series derivatives [75].

After filtering and smoothing steps, the state vector in position  $k$  can be predicted by information from all the previous and following points. Based on this prediction, it is possible to match every point with a probability factor to filter out all noises measurements, with a process known as *Deterministic Annealing Filter*, described in details in [76].

## 4.6 Analysis strategy

For the purposes of this thesis, data of  $400 \text{ MeV/u}$   $^{16}\text{O}$  beam against a target of graphite ( $C$ ) are considered. The main procedure to reach the goal of cross section measurements is reported in the following sections.

- At first, experimental data are taken into account in order to study pile up of projectile particles in an event (see Sec. 4.6.1), which is the consequence of more than one projectile hitting the target in the same acquisition time-window.
- Then the focus moves to a MC dataset generated by the FLUKA code to simulate detectors and beams with the GSI 2021 campaign settings. Tracks are reconstructed applying the Kalman filter algorithm.
- The trigger used during data acquisition is simulated in order to consider only fragmented particles from the dataset and thus to reject all the events in which the projectile did not interact. (see Sec. 4.6.2)
- Moreover, some background sources concerning the TW and track algorithm mis-reconstruction are studied to improve the purity of the data sample (see Sec. 4.6.3).
- A comparison between reconstructed and generated charges for every track is done, in order to verify the reliability of the used algorithms. A first attempt of correction is given for every charge through a scale factor (see Sec. 4.6.4).
- Subsequently, the efficiency of the tracking algorithm is measured comparing the reconstructed tracks and the generated MC particles (see Sec. 4.6.5).
- At this point, two different MC datasets are used to obtain a first cross section measurement (see Sec. 4.6.6): the former to retrieve background sources, efficiencies and scale factors of Eq. 4.13 and Eq. 4.14, the latter to simulate real data as Yield. The comparison of this cross section with the generated particles represents a closure test for the reliability of this analysis.
- The found efficiencies and scale factors are applied to a data run.
- Finally, after some considerations about how to handle real data, preliminary experimental cross section are shown.

All the plots shown in this chapter are taken from an MC dataset of 1 million of events generated by FLUKA to simulate the GSI2021 campaign.

### 4.6.1 Pile-up discrimination

As said in Sec.4.3.2, real data are acquired by a TDAQ system and stored when a trigger condition is satisfied. The main triggers are:

- *Minimum Bias* (MB): trigger is fired when at least 4 channels of the SC are fired with a certain signal in the time coincidence of 20 ns.
- *Fragmentation Bias* (FB): trigger is fired when MB holds and in anti coincidence with a signal from one of the TW central bars. In this way, all the events in which there is fragmentation of the projectile are considered. The not interacting beam particles, in fact, maintain their straight trajectory crossing only the center of TW.

The maximum acquisition rate, when operating with trigger, depends on the slowest detector, which in the FOOT setup is the MIMOSA chip used in the pixel trackers (VTX and ITR). Its readout frequency is about 5 kHz but, in order to limit source of systematic uncertainties, the DAQ rate is set to 1 kHz.

The acquisition of SC is managed by a system called WaveDAQ, whose sampling rate is set on 3Gsamples/s. Thus, considering every sampling as made of 1024 points, data acquisition window of SC is around 330 ns.

The facility used in GSI 2021 campaign was not able to deliver a stable flux at the frequency of 1 kHz and thus the sampling rate was not constant. As a consequence, there was the possibility of a superimposition of more than one projectile in the same SC time window, which translates in more than a peak of the fired SC raw signal, as seen in Fig. 4.6. It is then fundamental to filter out offline all the pile up events, otherwise they would worsen the overall analysis.

For the purpose of this thesis, an algorithm for pile-up discrimination was implemented on SHOE and its main aspects are described in the following section.

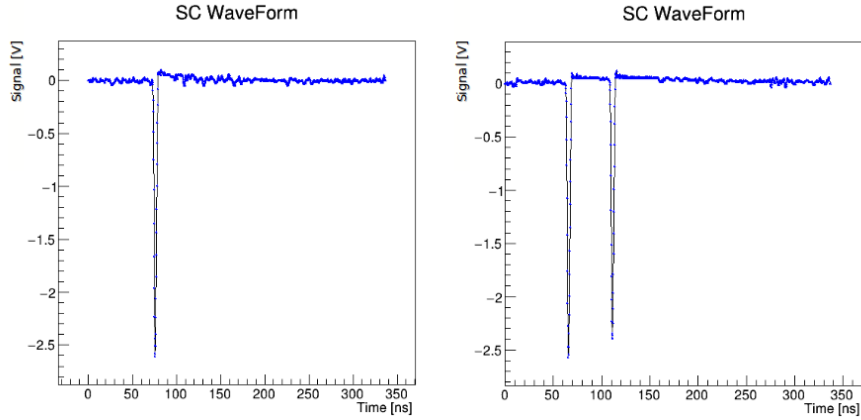


Figure 4.6: (Left) Signal of a single event fired in the SC. (Right) Pile-up of two events impinging the SC in the same sampling time window.

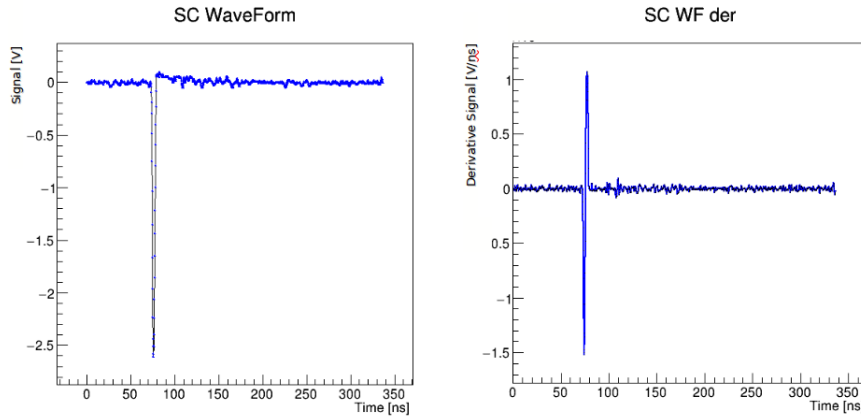


Figure 4.7: (Left) Signal of a single event fired in the SC. (Right) Derivative of the signal applying the derivative method.

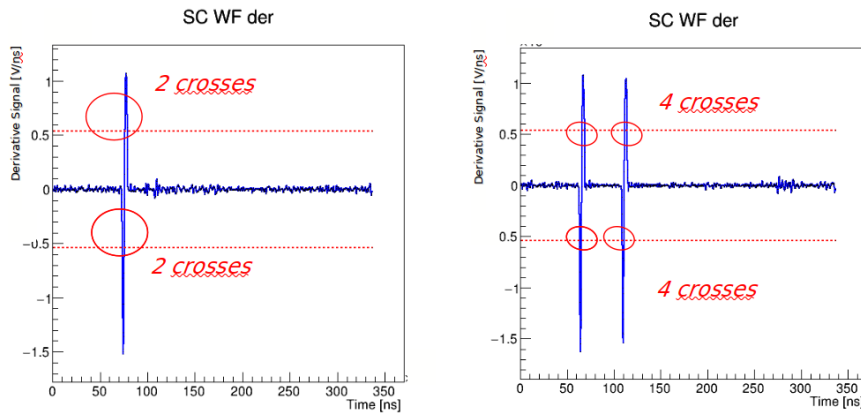
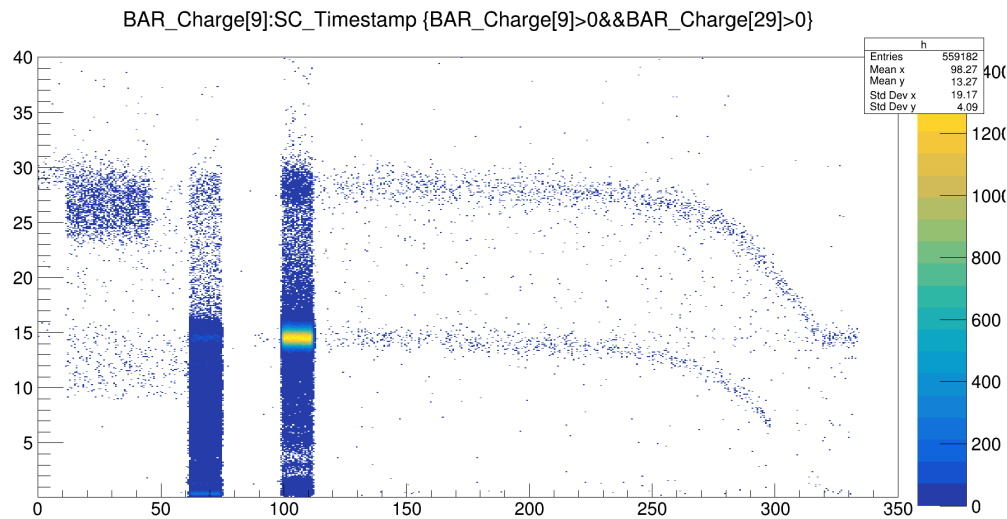


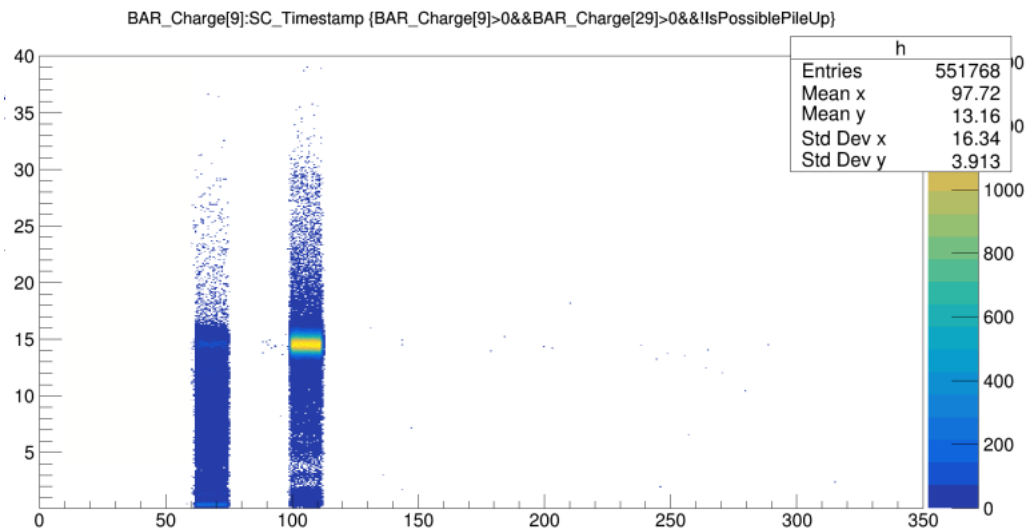
Figure 4.8: (Left) Derivative of a single signal: 4 intersection points. (Right) Derivative of a pile-up signal: more than 4 intersection points with the threshold lines.

### Derivative method

A derivative of every SC signal is measured in an iterative way every 5 points. Every signal peak results then into a distribution with two peaks of opposite sign, whose height depends on the steepness of the primitive one as seen in Fig.4.7.



(a) Plot of signal charge vs time of acquisition of events crossing the SC. The two "columns" are due Minimum Bias and Fragmentation trigger.



(b) (Left) Events crossing the SC after the pile-up discrimination.

Figure 4.9

Then, a threshold at 50% of the positive peak height is applied for both positive and negative signal values and their intersections are counted: a single signal crosses the threshold lines 4 times, while for a pileup signal the intersections are more (see Fig. 4.8). The used threshold was found after a dedicated study on GSI 2021 data sample.

This is at the basis of the *constant threshold discrimination method*, widely used in particle physics, i.e. by n\_TOF experiment for pulse shape processing [77].

## Application

In Fig.4.9a, signals fired by the SC are shown in a *signal charge vs time of acquisition* plot. The two “columns” are due to MB and FB triggers, which have two different response times and a width of 12 ns due to SC resolution. All the events out of the "columns" are possible cases of pile up and, in order to filter them out, the derivative method plus a time cut lower than 60 ns has been applied. The results are visible in Fig.4.9b. The method reveals fast and robust with a final removal of 1% of events marked as "pile-up" ones, improving the accuracy of the cross section measurement.

An important aspect to underline is that even spurious events disguised inside the "columns" are filtered out, an ability not replaceable by a pure cut-off method.

### 4.6.2 Fragmentation Trigger Simulation

As said in Sec. 4.6.1, the fragmentation trigger works when there is a signal in the SC (MB trigger) in anti coincidence with a signal from of the central bars of the TW, as reported in Fig. 4.10a.

In SHOE, a software trigger which simulates these requests has been implemented. In particular, all the fragments which interact with 3 TW bars (of ID 8,9,10) in both vertical and horizontal planes (see Fig. 4.10b) are rejected because considered as not fragmented projectile beam. An upper energy threshold is also applied to the signal of each scintillator bar.

Since the fragmentation is of the order of 8% in the target used at GSI, it is fundamental to limit all the contribution by the projectile in order to speed up data acquisition and reduce the amount of stored event without fragmentation. It is also fundamental to reject these events and to correctly simulate the trigger effects on MC for a precise cross section result. This is clearly visible in Fig. 4.11a and 4.11b, where the *reconstructed vs generated charge* plot before and after the simulated trigger application is shown. The plot

becomes more diagonal limiting the sources of systematics.

### 4.6.3 Background removal

The main sources of background investigated for this thesis are due to misreconstruction of charges and tracks respectively. Studies were carried out at the level of generated MC particles.

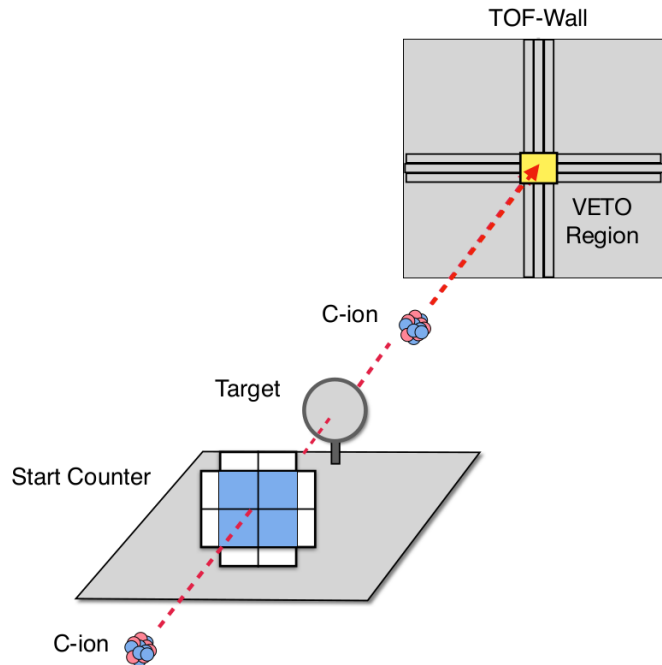
For what concern fragment identification, it is possible that TW is hit by several fragments at the same time, as reported in Fig. 4.12. On the one hand, it causes the deposition of a higher amount of energy and thus a wrong reconstruction of the fragment, while on the other hand the position of the hit can be badly evaluated by ghost hits effects.

Therefore, a code is implemented in SHOE where all the reconstructed tracks of which the TW point is composed by more than one hit are disentangled. Of course, it is an information that is possible to retrieve only from a MC dataset.

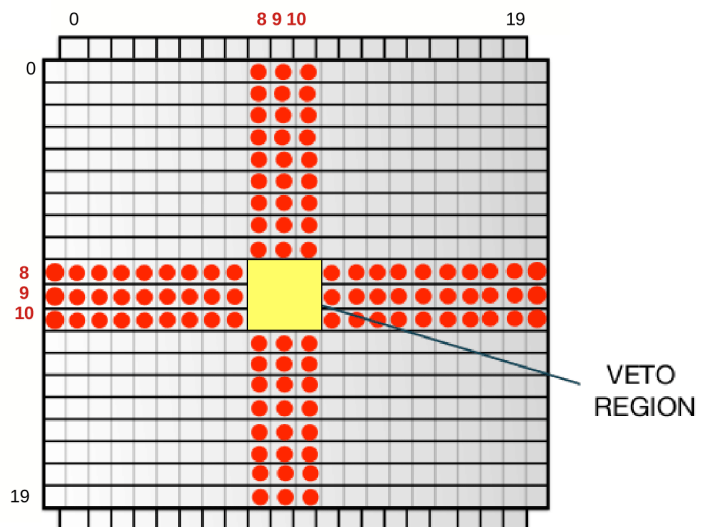
The charge identification is at the basis even of track misreconstruction. In the best scenario, a track is made of points all belonging to the same particle, as shown in Fig. 4.13a. However, due to several systematic effects such as secondary fragmentation out of target, it is possible that hits of different particles are matched in the same track, causing an overall bad match, as shown in Fig. 4.13b. If the TW point belongs to another particle, due to its importance in the overall tracking algorithm as explained in Sec. 4.5.1, it is possible that the track is badly reconstructed, associating the wrong charge to the track itself.

Thus, an algothm is implemented in SHOE where all the reconstructed tracks whose associated generated particle is different from the one relative to the TW point are rejected.

Both contributions can be estimante via MC studies and considered as background sources. Subtracting both contributes, the fragment distributions of Fig. 4.11b becomes the one shown in Fig. 4.11c. What can be seen is that the distribution in terms of *reconstructed charge vs the generated one* becomes more diagonal. This means that the possibility of misreconstruction is highly reduced.

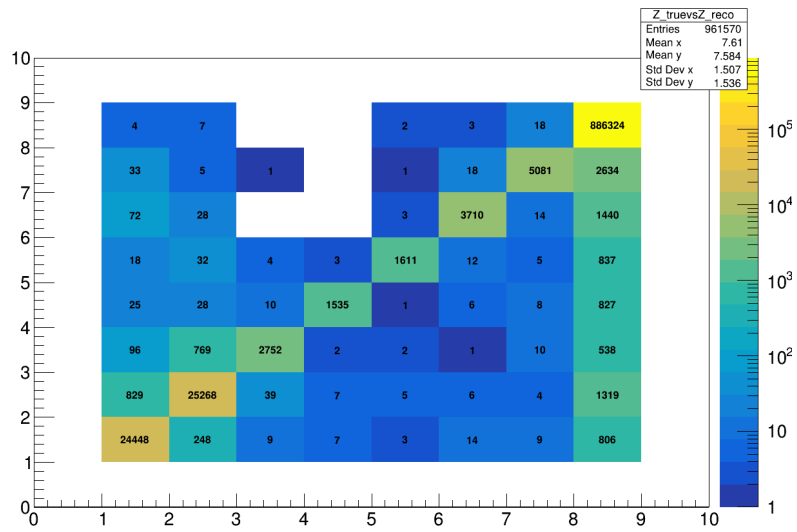


(a) Sketch of the fragmentation trigger in the FOOT setup: it is fired when there is a signal in the SC and NOT in the central part of the TW.

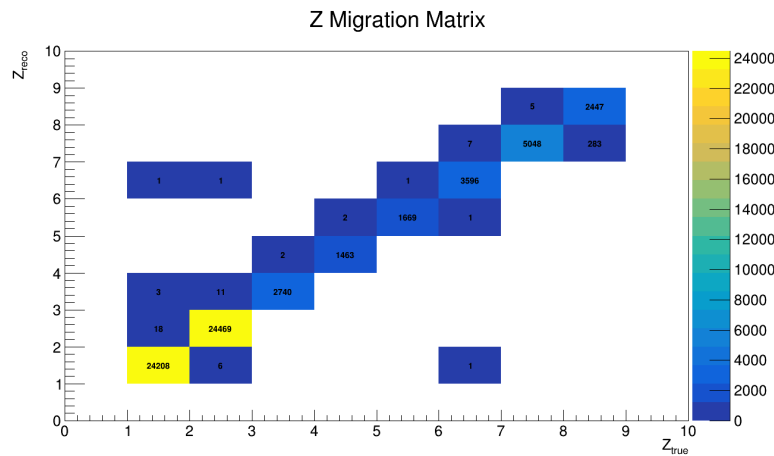


(b) The TW bars interested by the VETO are the ones of ID = 8, 9, 10 for both vertical and horizontal plane.

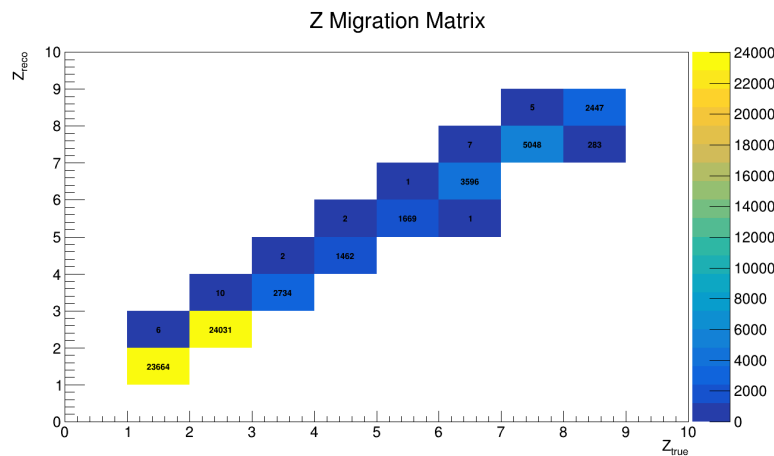
Figure 4.10



(a) Migration matrix of reconstructed tracks



(b) Migration matrix of reconstructed tracks after simulated trigger application



(c) Migration matrix of reconstructed tracks after simulated trigger application and background removal

Figure 4.11

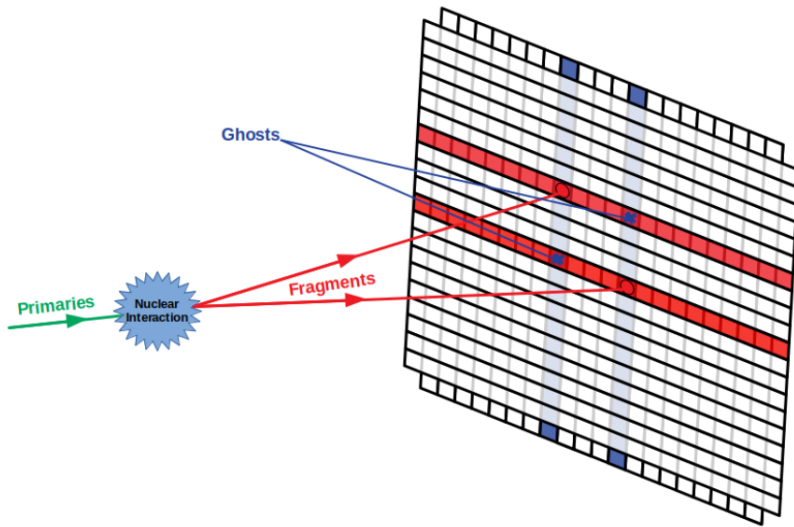


Figure 4.12: More than one fragment can reach the TW bars of each plane, causing the release of multiple hits and the formation of ghost hits effects

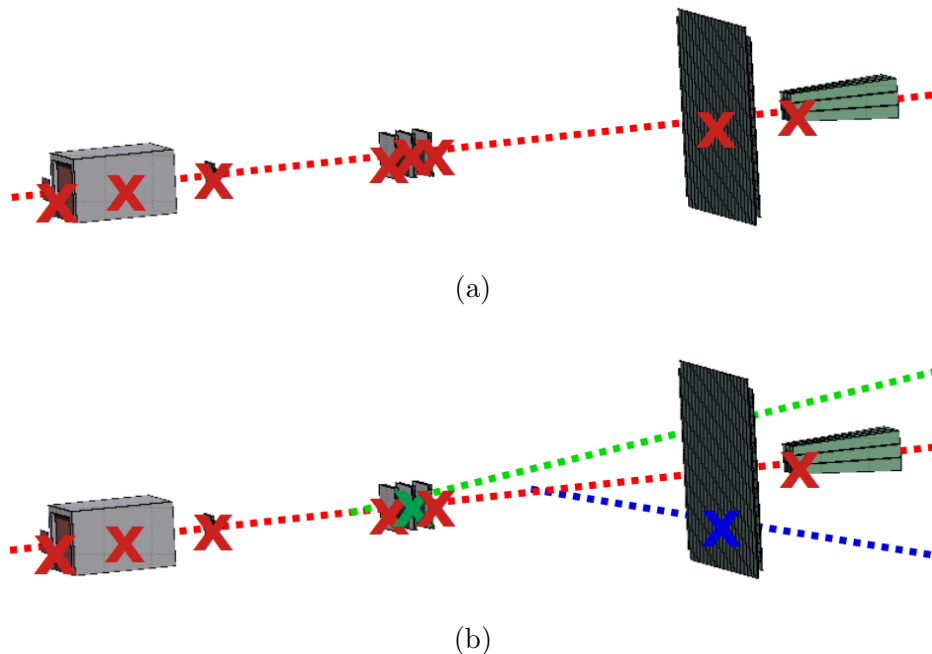


Figure 4.13: Sketch of track reconstruction in GSI 2021 set up.

- (a) In the best scenario, all the points of a track belongs to the same particles.
- (b) Due to secondary fragmentation and other systematics, it is possible that points belonging to different particles are matched in the same track

#### 4.6.4 Fragment correction

What shown in Fig. 4.11c is called *migration matrix*, which represents the reconstructed charge of a track with respect to the charge of the generated particle associated.

For every track, the generated charge is reported on the X axis, while the reconstructed one on the Y axis. Thus, all the fragments in the diagonal are well reconstructed, while the ones outside suffer of charge migration.

Several correction methods are applied in nuclear and subnuclear physics in order to correct for the migration of variable values, among which the most common is *unfolding*, explained in [78].

For the purposes of this thesis, a first attempt of migration correction is introduced comparing the reconstructed fragment and the generated charge distributions. In particular a scale factor  $\gamma$  is calculated for every fragment as:

$$\gamma(Z) = \frac{Y(Z)_{reco} - Y(Z)_{reco}^{mis} + Y(Z)_{gen}^{mis}}{Y(Z)_{reco}} \quad (4.9)$$

where  $Y_{mis}(Z)$  is the sum of all the reconstructed fragments of a given  $Z$ ,  $Y(Z)_{mis}^{out}$  represents all the fragments with different generated charges but reconstructed as charge  $Z$ ,  $Y(Z)_{gen}^{mis}$  represents all the fragments generated with charge  $Z$  but wrongly reconstructed as other charges.

Values of the scale factor can be higher or lower than 1, since it is different from an efficiency. The scale factors of the migration matrix of Fig. 4.11c are reported in Fig. 4.14: all the values are very close to 1 because, thanks to the background corrections, the starting matrix was already diagonal in a good way.

#### 4.6.5 Track efficiency

The efficiency of the tracking algorithm has been computed comparing respectively reconstructed tracks and MC generated particles, as follows:

$$\epsilon(Z) = \frac{N_{track}(Z)}{N_{true}(Z)} \quad (4.10)$$

where  $N_{track}(Z)$  represents the reconstructed particle by the Kalman Filter algorithm and  $N_{true}(Z)$  the MC true particle. Considering the efficiency as a binomial distribution, the standard deviation is calculated as follow:

$$\sigma_\epsilon(Z) = \sqrt{\frac{\epsilon(Z)(1 - \epsilon(Z))}{N_{true}(Z)}} \quad (4.11)$$

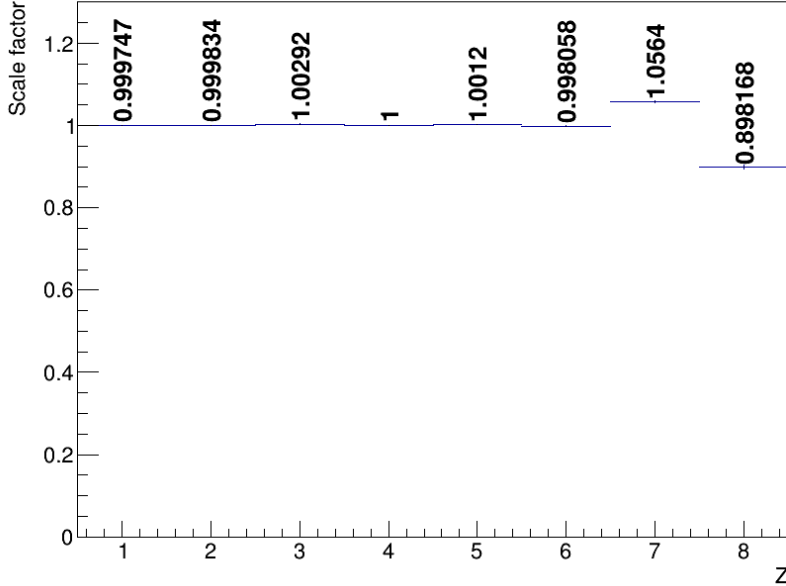


Figure 4.14: Scale factors of the migration matrix of Fig. 4.11c

In parallel, a similar equation can be used to measure the efficiency differential in angle for every fragment:

$$\epsilon(Z, \theta) = \frac{N_{track}(Z, \theta)}{N_{true}(Z, \theta)} \quad (4.12)$$

with an analogous standard deviation.

Reconstructed tracks correspond to fragments which leave a signal in all detectors between TG and TW (fundamental for charge identification). As a consequence of that, the particles used in MC studies were selected among primary fragments generated in the TG with an energy  $E > 100\text{MeV}/u$ , enough to go beyond the target and to reach the end of the apparatus.

At this point, two different studies are carried out. On the one hand, no angular constraints are applied: this means that in the MC dataset all the particles with an angular aperture higher than the TW acceptance are considered, in sight of a total cross section measurement. On the other hand, an emission with  $\theta < 8^\circ$  was requested, to match with the angular acceptance of the TW and in sight of a so called "fiducial" cross section measurement.

#### 4.6.6 Cross section empirical formula

The angular differential cross section is empirically defined as follows:

$$\frac{d\sigma}{d\theta}(Z) = \frac{Y(Z, \theta) - B}{N_{beam} N_{target} \Omega_\theta \epsilon(Z, \theta)} \quad (4.13)$$

where  $Y(Z, \theta)$  and  $\epsilon(Z, \theta)$  are respectively the number of fragments and the efficiency of a given charge reconstructed in every event,  $B$  is the background present in each fragment production,  $\Omega_\theta$  is the phase space,  $N_{prim}$  is the number of primaries impinging on the target and  $N_{target}$  is the number of interaction centres in the target per unit surface. The total elemental cross section can be obtained integrating Eq. 4.13:

$$\sigma(Z) = \int_0^{\theta_{max}} \frac{d\sigma}{d\theta}(Z) = \frac{Y(Z) - B}{N_{beam} N_{target} \epsilon(Z)} \quad (4.14)$$

where  $\theta_{max}$  represents the maximum angular acceptance of the detector.  $N_{beam}$  is an information retrieved by the SC and BM and can be considered as the sum of all the selected events taking part in the analysis. Instead, the number of scattering centers  $N_{target}$  can be written as:

$$N_{target} = \frac{\rho \Delta x N_A}{A} \quad (4.15)$$

where  $\rho$  is the density,  $\Delta x$  is the target thickness,  $N_A$  the Avogadro number and  $A$  the mass number. In particular, for the graphite target  $\rho = 1.83$   $g/cm^3$ ,  $\Delta x = 0.5$  cm and  $A = 12.0107$ .

The efficiencies  $\epsilon$  are introduced dividing the Yield by the given factor for every bin of the distribution, both for elemental and angular differential cross sections.

In the following chapter, all the results are shown.

# Chapter 5

## Results

### 5.1 Closure test on MC dataset

A MC dataset of 1 million of events was generated by FLUKA to simulate the GSI 2021 campaign. Following the procedure described in Sec. 4.6, an elemental fragmentation cross section (both fiducial and total) and an angular differential fragmentation cross section for every charge has been measured as final goal.

In Fig. ?? the MC fragment distribution is shown, considering also background contributions. What emerges is that the only elements which suffer of misreconstruction after the applied selections are  $H$  and  $He$ : they are the lightest ones and thus their release of energy in the apparatus is low. This worsen the performance of the charge identification algorithm and, as a consequence, the one of track reconstruction for this kind of elements.

In Fig.5.3, all the angular yields and background contributions are reported for every fragment, following the behaviour already commented. In all the considered cases, it is possible to note that the background source due to the tracking algorithm is much lower than the TW one, underlying its high reliability.

In Fig. 5.2a and Fig. 5.2b the tracking efficiencies respectively in sight of a *fiducial* and *total* elemental fragment cross section (see Sec. 4.6.5) are reported. In general, an efficiency higher than 80% is obtained for elements heavier than  $Li$ , while for  $H$  and  $He$  other considerations need to be done. In Fig. 5.2b, efficiency values are lower due to geometrical reasons: all the particles emitted outside the angular acceptance of the TW ( $\sim 8^\circ$ ) are removed at MC level. In Fig. 5.2a, instead, values are lower than the ones

of heavier fragments due to the not suited performance of the apparatus for light elements, as above mentioned.

Comparing the two efficiency plots, moreover, it is possible to ascertain that the main differences are in the lower fragments: that's because an angular constraint of  $\theta < 8^\circ$  has negligible effect on heavy fragments whose angular distribution is peaked around  $1^\circ$  and steeply decreases, as said in Sec. 3.2. The track efficiencies for every fragment, in terms of angular distribution are reported in Fig. 5.4. The previous distinction between fiducial and total datasets is not requested in this case because the fragments inside the angular acceptance of the apparatus are the same in both: all the fragments of the total dataset outside this angle aperture are in fact cut out since reconstruction is not possible.

Inspecting the plots, efficiency starts to decrease for angles with  $\theta > 4^\circ$ , where the simulated MC statistics of the tracks is low due to border effects in the detectors' layers. For  $Z = 7$  and  $Z = 8$  fragments, a reshape of the bins is needed due to the low yield of the fragments. A further improvement would be a simulation with more events to reduce also the efficiency uncertainties at high angles.

Once all the elements of Eq. 4.14 and of Eq. 4.13 are obtained, cross sections can be measured.

If a MC dataset of 1 million of events was used to obtain background sources and efficiencies from the generated particles, another MC dataset of 1 million of events was introduced to simulate the reconstructed tracks that can be retrieved in real experiments. The aim is to understand the reliability of the analysis chain and algorithms comparing the MC data-like cross sections with the MC simulated ones.

In Fig. 5.5, fiducial and total elemental fragmentation cross sections are reported, where the ratio between the data-like and simulated MC datasets represents the reliability of the used algorithms and strategy. For all the elements, the ratio value is very close to one, showing that the followed analysis procedure described in Sec. 4.6 is solid.

The obtained cross section values are reported in Tab. 5.1 and, as expected, the difference is slightly bigger between the two measurements referred to  $H$  and  $He$  fragments due to different track efficiencies.

Analogously, the angular differential cross sections and the relative numerical values are reported in Fig. 5.6 and in Tab. 5.2 respectively. For angular distributions as well, the ratio is very close to one, worsening for higher and higher angles where the statistics is poorer and the detector start to loose full coverage.

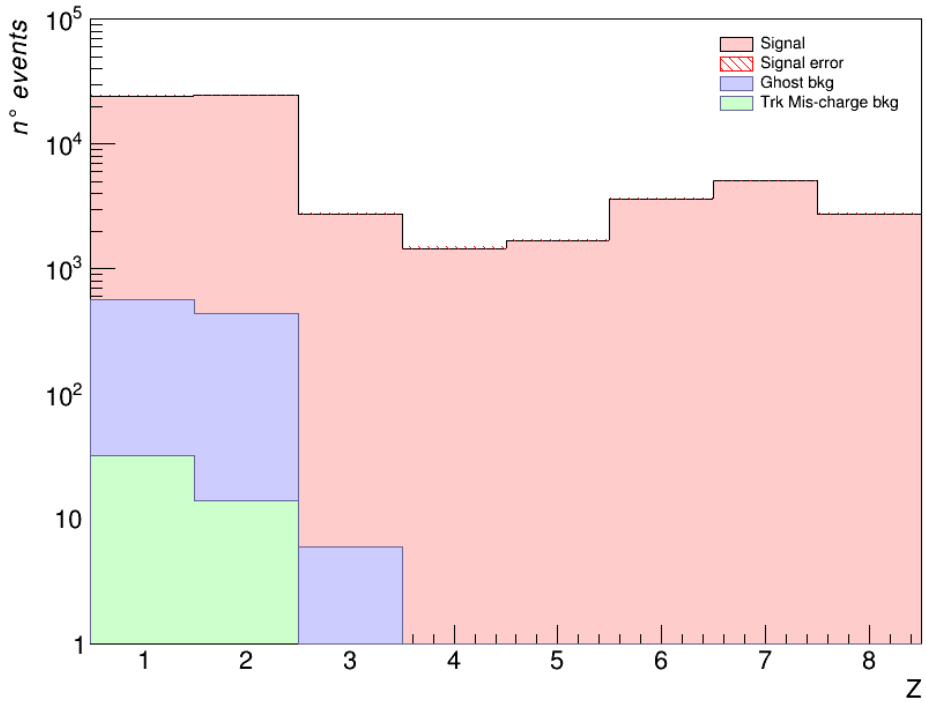
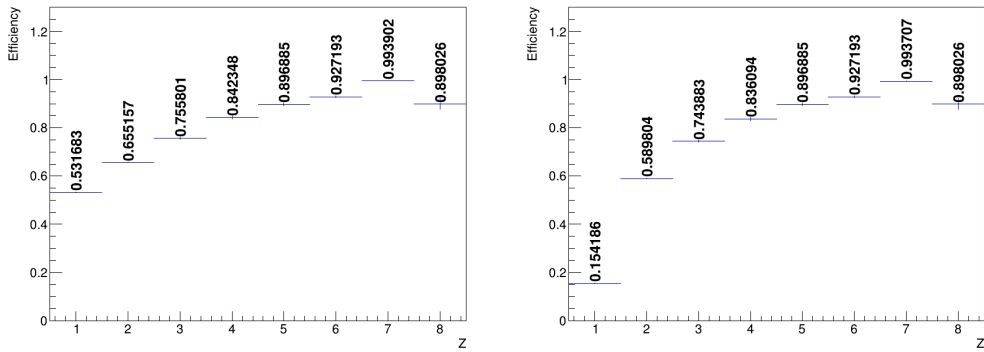


Figure 5.1: Fragment distribution (in red) concerning background contribution due to TW (blue) and tracking (green) misreconstruction



(a) Track efficiency of fragments for fiducial cross section

(b) Track efficiency of fragments for total cross section

Figure 5.2

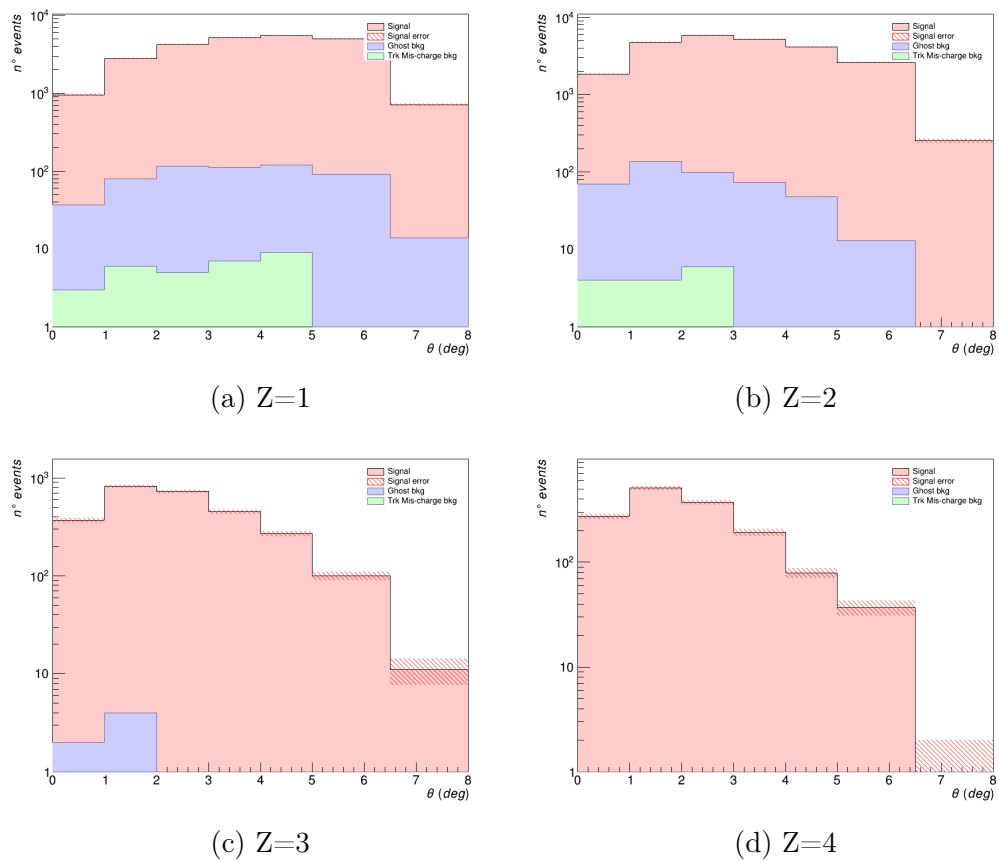


Figure 5.3: Angular distributions with background components of fragments

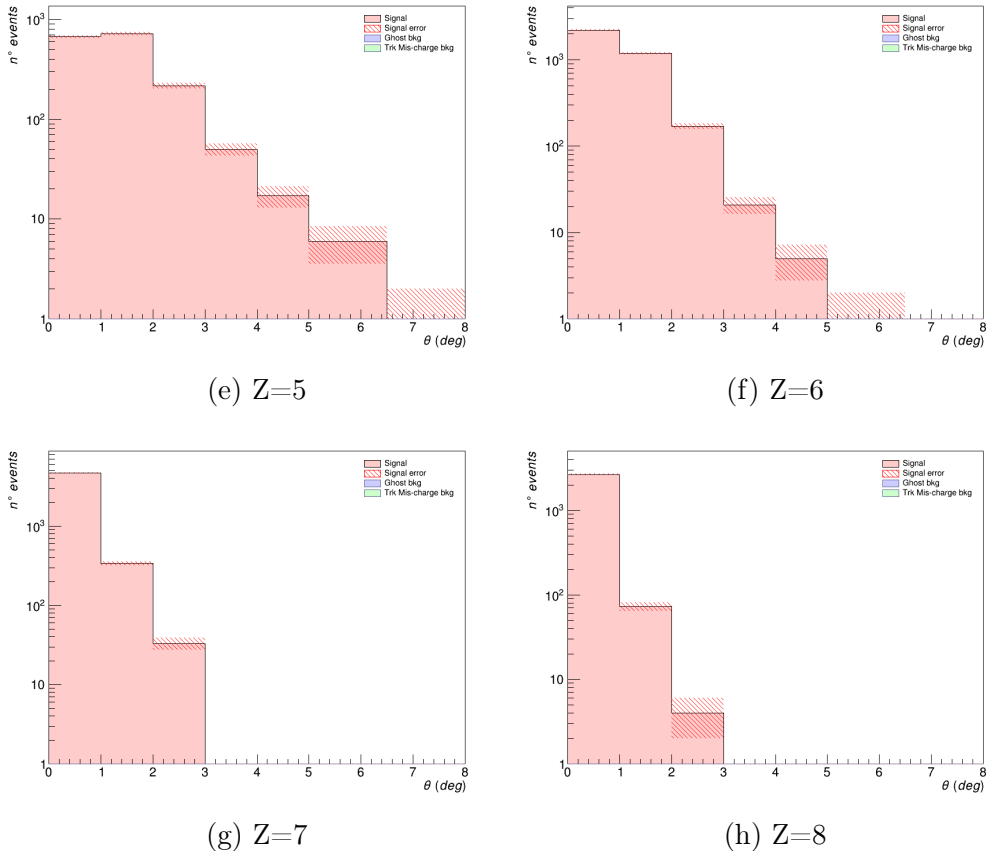


Figure 5.3: Angular distributions with background components of fragments (cont.)

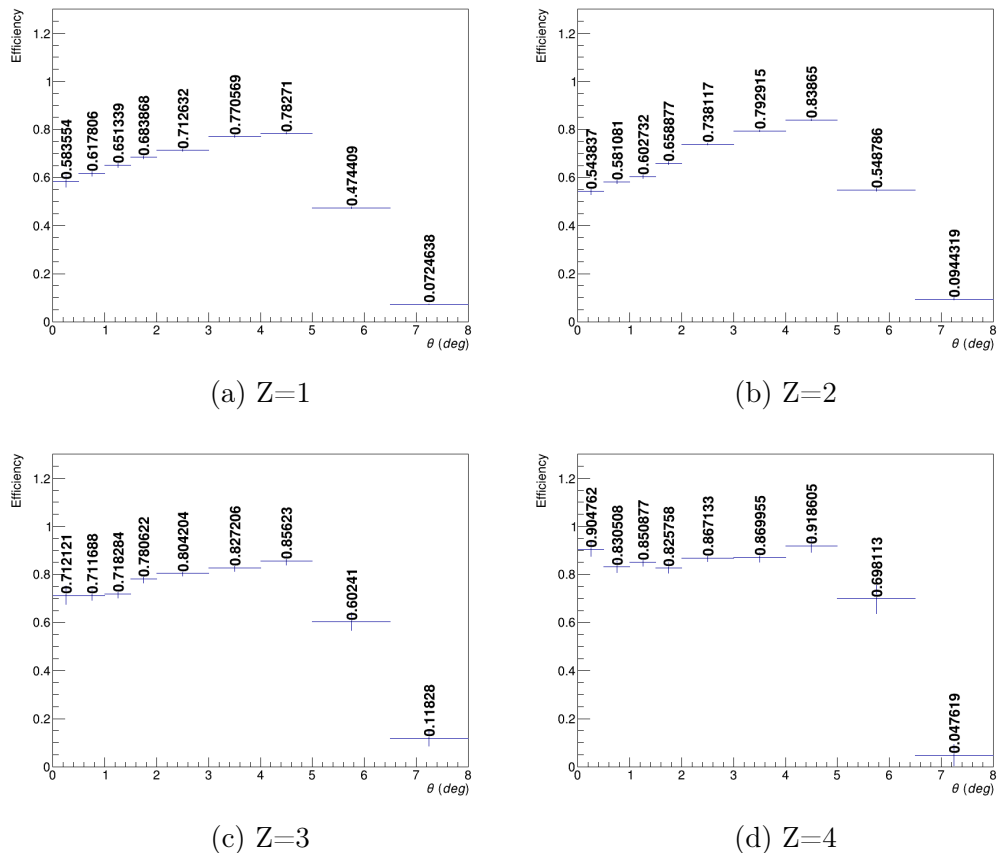


Figure 5.4: Angular track efficiency for every fragment

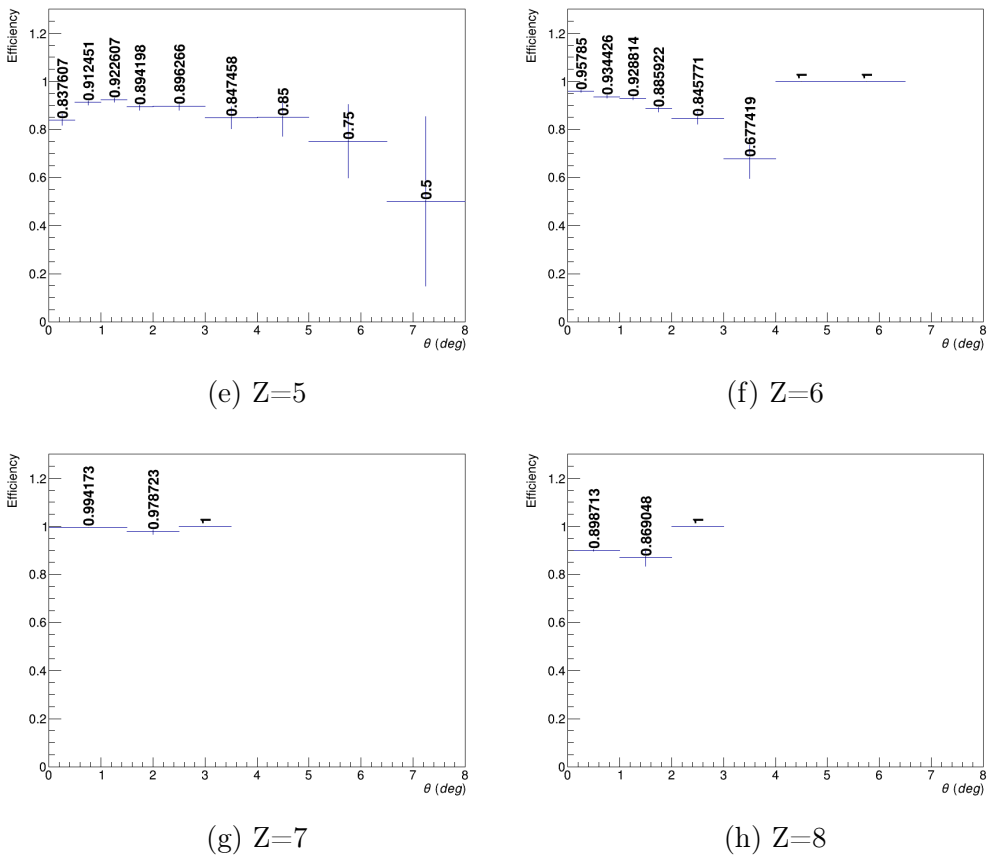
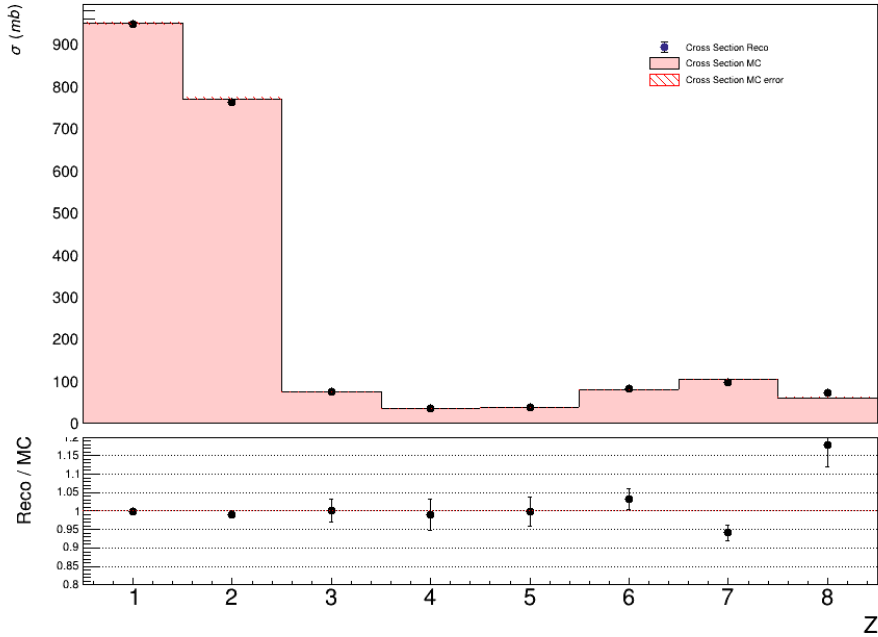
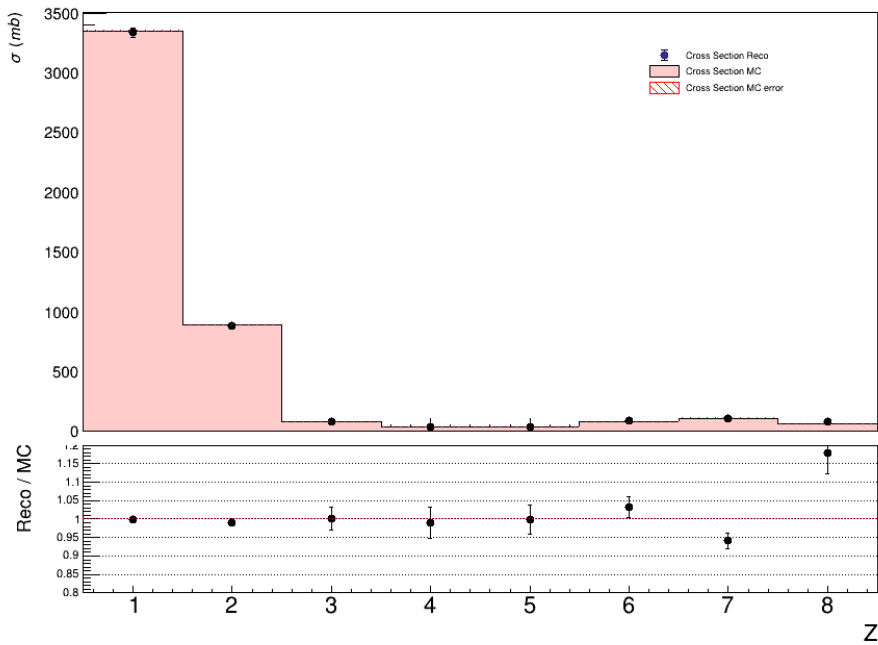


Figure 5.4: Angular track efficiency for every fragment (cont.)



(a) Elemental fragmentation *fiducial* cross section (dots) in comparison with MC generated particle distributions (red) and their ratio



(b) Elemental fragmentation *total* cross section (dots) in comparison with MC generated particle distributions (red) and their ratio

Figure 5.5

Charge	$\sigma_{meas}$ (mb)	$\sigma_{MC}$ (mb)
Z = 1	$946 \pm 9$	$949 \pm 4$
Z = 2	$762 \pm 7$	$770 \pm 4$
Z = 3	$74 \pm 1$	$74 \pm 1$
Z = 4	$35 \pm 1$	$35 \pm 0$
Z = 5	$37 \pm 1$	$37 \pm 0$
Z = 6	$82 \pm 1$	$79 \pm 1$
Z = 7	$97 \pm 1$	$103 \pm 1$
Z = 8	$72 \pm 3$	$61 \pm 1$

(a) *Fiducial* Elemental Fragmentation Cross section values for reconstructed and MC data

Charge	$\sigma_{meas}$ (mb)	$\sigma_{MC}$ (mb)
Z = 1	$3337.5 \pm 36.5$	$3346.2 \pm 8.5$
Z = 2	$880.0 \pm 8.7$	$888.5 \pm 4.4$
Z = 3	$80.4 \pm 2.1$	$80.2 \pm 1.3$
Z = 4	$37.8 \pm 1.3$	$38.2 \pm 0.9$
Z = 5	$40.5 \pm 1.3$	$40.6 \pm 0.9$
Z = 6	$87.5 \pm 1.9$	$84.7 \pm 1.4$
Z = 7	$104.2 \pm 1.9$	$110.8 \pm 1.6$
Z = 8	$78.2 \pm 3.6$	$66.3 \pm 1.2$

(b) *Total* Elemental Fragmentation Cross section values for reconstructed and MC data

Table 5.1

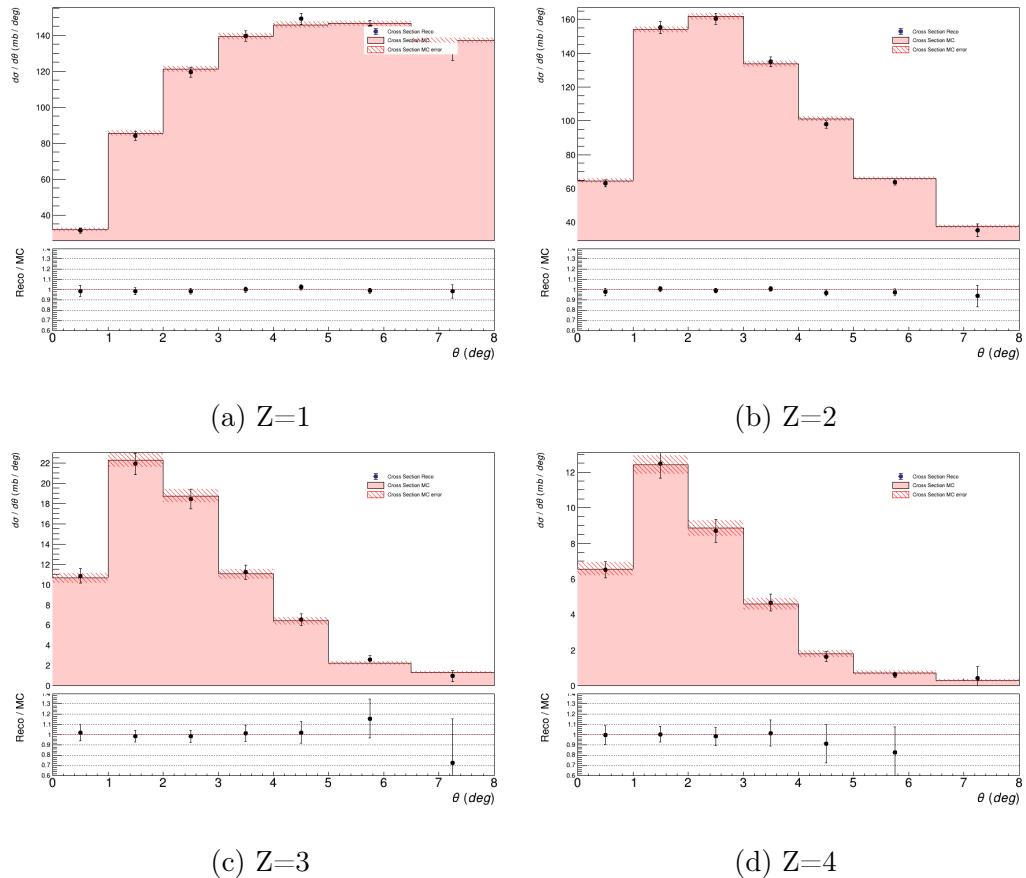


Figure 5.6: Differential angular cross section for a reconstruction sampling (points) in comparison with generated MC data (in red) and their ratio (cont.)

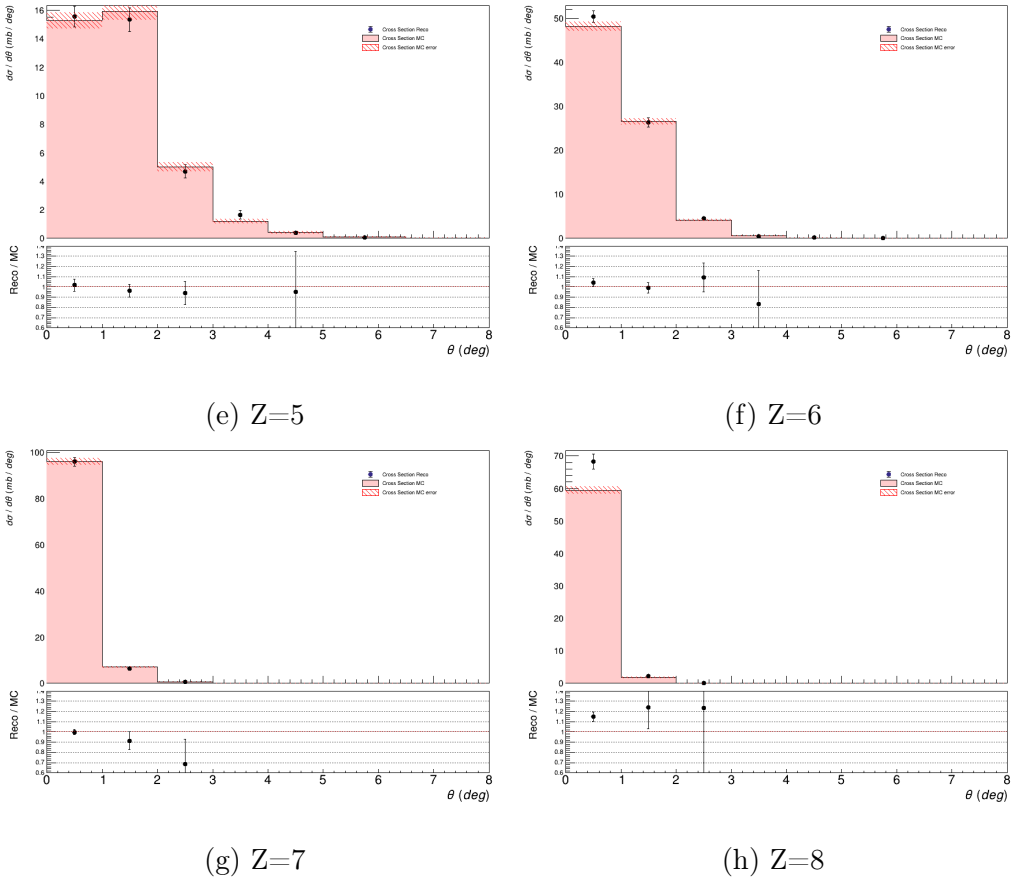


Figure 5.6: Differential angular cross section for a reconstruction sampling (points) in comparison with generated MC data (in red) and their ratio.

Angle( <i>degree</i> )	$\sigma_{meas}$ (mb)	$\sigma_{MC}$ (mb)
$0.0 \leq \theta < 1.0$	$31 \pm 1$	$31 \pm 0$
$1.0 \leq \theta < 2.0$	$84 \pm 2$	$85 \pm 1$
$2.0 \leq \theta < 3.0$	$119 \pm 2$	$121 \pm 1$
$3.0 \leq \theta < 4.0$	$139 \pm 2$	$139 \pm 1$
$4.0 \leq \theta < 5.0$	$149 \pm 3$	$145 \pm 1$
$5.0 \leq \theta < 6.5$	$144 \pm 3$	$146 \pm 1$
$6.5 \leq \theta < 8.0$	$134 \pm 8$	$137 \pm 1$

(a) Z=1

Angle( <i>degree</i> )	$\sigma_{meas}$ (mb)	$\sigma_{MC}$ (mb)
$0.0 \leq \theta < 1.0$	$63 \pm 2$	$64 \pm 1$
$1.0 \leq \theta < 2.0$	$155 \pm 3$	$153 \pm 1$
$2.0 \leq \theta < 3.0$	$160 \pm 3$	$161 \pm 1$
$3.0 \leq \theta < 4.0$	$134 \pm 2$	$133 \pm 1$
$4.0 \leq \theta < 5.0$	$98 \pm 2$	$101 \pm 1$
$5.0 \leq \theta < 6.5$	$63 \pm 1$	$65 \pm 0$
$6.5 \leq \theta < 8.0$	$35 \pm 3$	$37 \pm 0$

(b) Z=2

Angle( <i>degree</i> )	$\sigma_{meas}$ (mb)	$\sigma_{MC}$ (mb)
$0.0 \leq \theta < 1.0$	$10 \pm 0$	$10 \pm 0$
$1.0 \leq \theta < 2.0$	$21 \pm 1$	$22 \pm 0$
$2.0 \leq \theta < 3.0$	$18 \pm 0$	$18 \pm 0$
$3.0 \leq \theta < 4.0$	$11 \pm 0$	$11 \pm 0$
$4.0 \leq \theta < 5.0$	$6 \pm 0$	$6 \pm 0$
$5.0 \leq \theta < 6.5$	$2 \pm 0$	$2 \pm 0$

(c) Z=3

Table 5.2: Differential angular cross section for a reconstruction sampling (points) in comparison with generated MC data (in red) and their ratio

Angle( <i>degree</i> )	$\sigma_{meas}$ (mb)	$\sigma_{MC}$ (mb)
$0.0 \leq \theta < 1.0$	$6 \pm 0$	$6 \pm 0$
$1.0 \leq \theta < 2.0$	$12 \pm 0$	$12 \pm 0$
$2.0 \leq \theta < 3.0$	$8 \pm 0$	$8 \pm 0$
$3.0 \leq \theta < 4.0$	$4 \pm 0$	$4 \pm 0$
$4.0 \leq \theta < 5.0$	$1 \pm 0$	$1 \pm 0$

(d) Z=4

Angle( <i>degree</i> )	$\sigma_{meas}$ (mb)	$\sigma_{MC}$ (mb)
$0.0 \leq \theta < 1.0$	$15 \pm 0$	$15 \pm 0$
$1.0 \leq \theta < 2.0$	$15 \pm 0$	$15 \pm 0$
$2.0 \leq \theta < 3.0$	$4 \pm 0$	$4 \pm 0$
$3.0 \leq \theta < 4.0$	$1 \pm 0$	$1 \pm 0$

(e) Z=5

Angle( <i>degree</i> )	$\sigma_{meas}$ (mb)	$\sigma_{MC}$ (mb)
$0.0 \leq \theta < 1.0$	$50 \pm 1$	$48 \pm 1$
$1.0 \leq \theta < 2.0$	$26 \pm 1$	$26 \pm 0$
$2.0 \leq \theta < 3.0$	$4 \pm 0$	$4 \pm 0$

(f) Z=6

Table 5.2: Differential angular cross section for a reconstruction sampling (points) in comparison with generated MC data (in red) and their ratio (cont.)

Angle( <i>degree</i> )	$\sigma_{meas}$ (mb)	$\sigma_{MC}$ (mb)
$0.0 \leq \theta < 1.0$	$95 \pm 1$	$95 \pm 1$
$1.0 \leq \theta < 2.0$	$6 \pm 0$	$7 \pm 0$

(g) Z=7

Angle( <i>degree</i> )	$\sigma_{meas}$ (mb)	$\sigma_{MC}$ (mb)
$0.0 \leq \theta < 1.0$	$68 \pm 2$	$59 \pm 1$
$1.0 \leq \theta < 2.0$	$2 \pm 0$	$1 \pm 0$

(h) Z=8

Table 5.2: Differential angular cross section for a reconstruction sampling (points) in comparison with generated MC data (in red) and their ratio (cont.)

## 5.2 Experimental results

A first measurement of experimental cross section was achieved analyzing a dataset of 570000 events taken during the GSI 2021 campaign.

Differently from MC data where the geometry and the positions of each subdetector were known a priori, the real apparatus suffers of little shifts and movements due to technical and physical reasons faced in the research room. Alignment is then fundamental to remove all the offsets introduced by the subdetectors and thus systematics due to a wrong reconstruction of the points of interaction. This will be object of detailed studies for future improved results of cross sections.

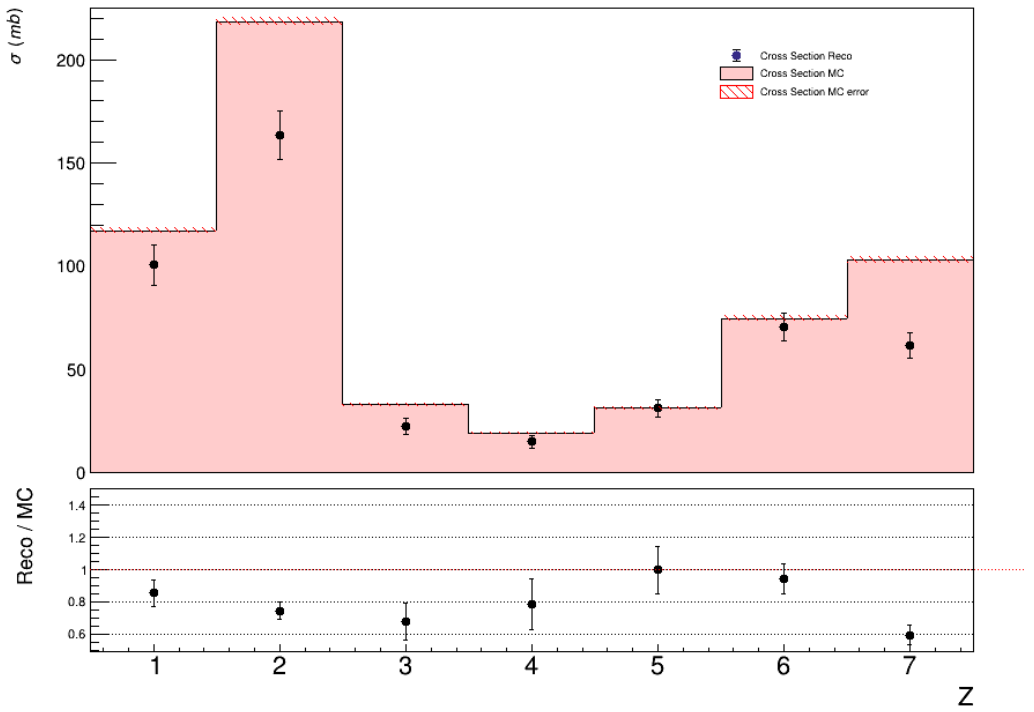
Checking the consistency of experimental cross section measurements with Monte Carlo simulation was deliberated as the first goal. Thus, the tracking reconstruction algorithm was set in such a way the angular aperture of every track cannot be higher than  $3^\circ$ . From the one hand, a lot of noise due to reconstruction of secondary fragments with high angle emission is omitted, increasing the statistics of the used signal. From the other hand, since the angular distribution of heavy fragments is very peaked around  $1^\circ$  (see Sec. 3.2), the chosen selection does not invalidate the following results.

The experimental elemental fragment cross section and its numerical values are reported in Fig. 5.7, where a comparison with the MC distribution is present. It was chosen to omit  $Z=8$  particles from the analysis because the discrimination between Oxygen projectiles and fragments need further investigation studies. What can be inspected is that the match between experimental and MC data for all the elements seems in good agreement, with a ratio of the order of magnitude of 1 for all of them. In particular, the best similarities appear for heavy ions, for which the apparatus is better performed.

The angular differential cross sections of experimental data and their values are reported in Fig. 5.8 and Tab. 5.3 respectively. Despite the comparison is in good consistency for all the fragments, it is possible to see, mainly for heavier ones, that the experimental distribution is slightly shifted. One of the main reasons is surely the misalignment between TW and VTX: an offset in their position definition can change, even considerably, the angular distribution reconstruction of the track. Further studies about this issues need to be started for the next experimental measurements.

To conclude, the obtained results represents a powerful point of arrival for the aforementioned analysis strategy stating that a good correspondence holds between MC simulations and experimental data for the GSI 2021 cam-

paing of  $^{16}O$  at 400 MeV/u impinging on a target of Graphite. However, new studies can be easily introduced to refine it. In particular, systematics uncertainty need to be evaluated and a more powerful correction method, like the already mentioned *unfolding*, can be implemented. This would enhance the results of the actual dataset, in sight of the new cross section measurements for data about  $^{16}O$  at 400 MeV/u and 200 MeV/u impinging on graphite (C) and polyethilene ( $C_6H_6$ ) for the GSI 2021 campaign, as well as for new data taking that are forseen in the next months by the FOOT experiment, when the overall setup would be present.



(a) Experimental elemental cross section (dots) in comparison with MC generated particle distributions (red) and their ratio

Charge	$\sigma_{meas}$ (mb)	$\sigma_{MC}$ (mb)
$Z = 1$	$100 \pm 9$	$117 \pm 1$
$Z = 2$	$163 \pm 11$	$218 \pm 2$
$Z = 3$	$22 \pm 3$	$32 \pm 0$
$Z = 4$	$14 \pm 2$	$18 \pm 0$
$Z = 5$	$31 \pm 4$	$31 \pm 0$
$Z = 6$	$70 \pm 6$	$74 \pm 1$
$Z = 7$	$61 \pm 6$	$103 \pm 1$
$Z = 8$	$708 \pm 37$	$61 \pm 1$

(b) Elemental Fragmentation Cross section values for experimental and MC data

Figure 5.7

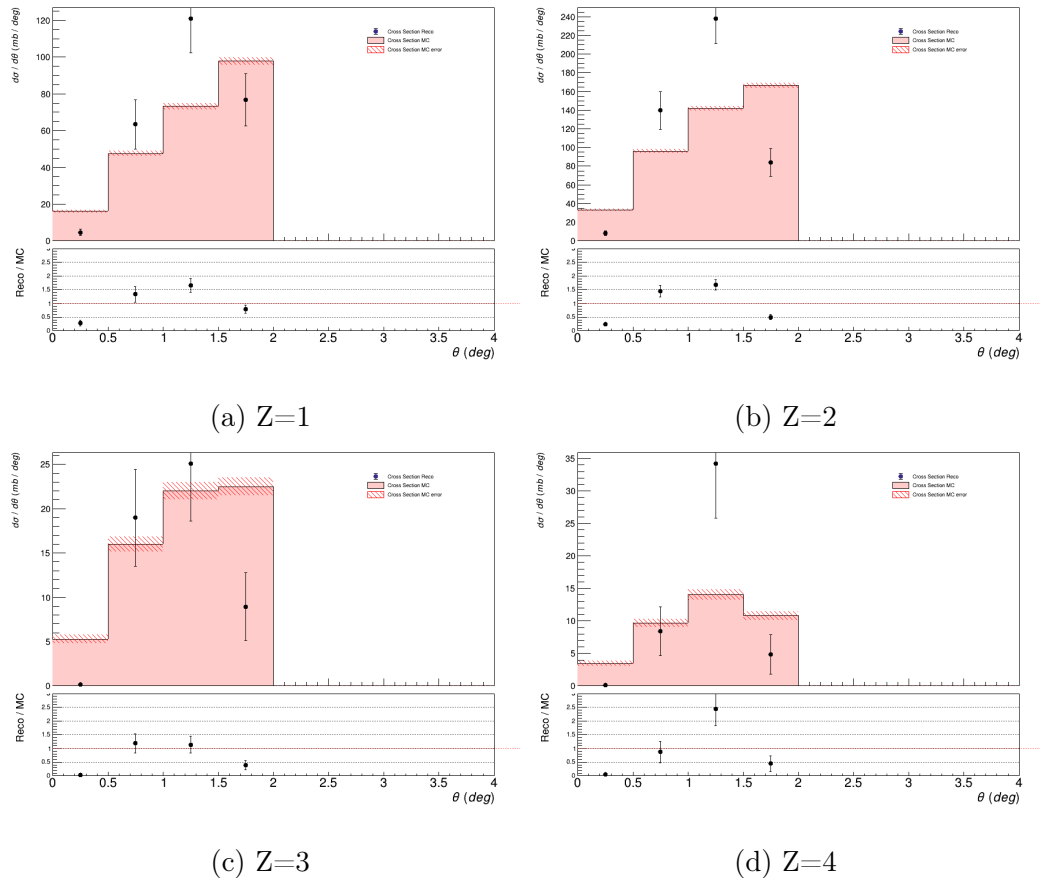


Figure 5.8: Differential angular cross section for the experimental sampling (points) in comparison with generated MC data (in red) and their ratio (cont.)

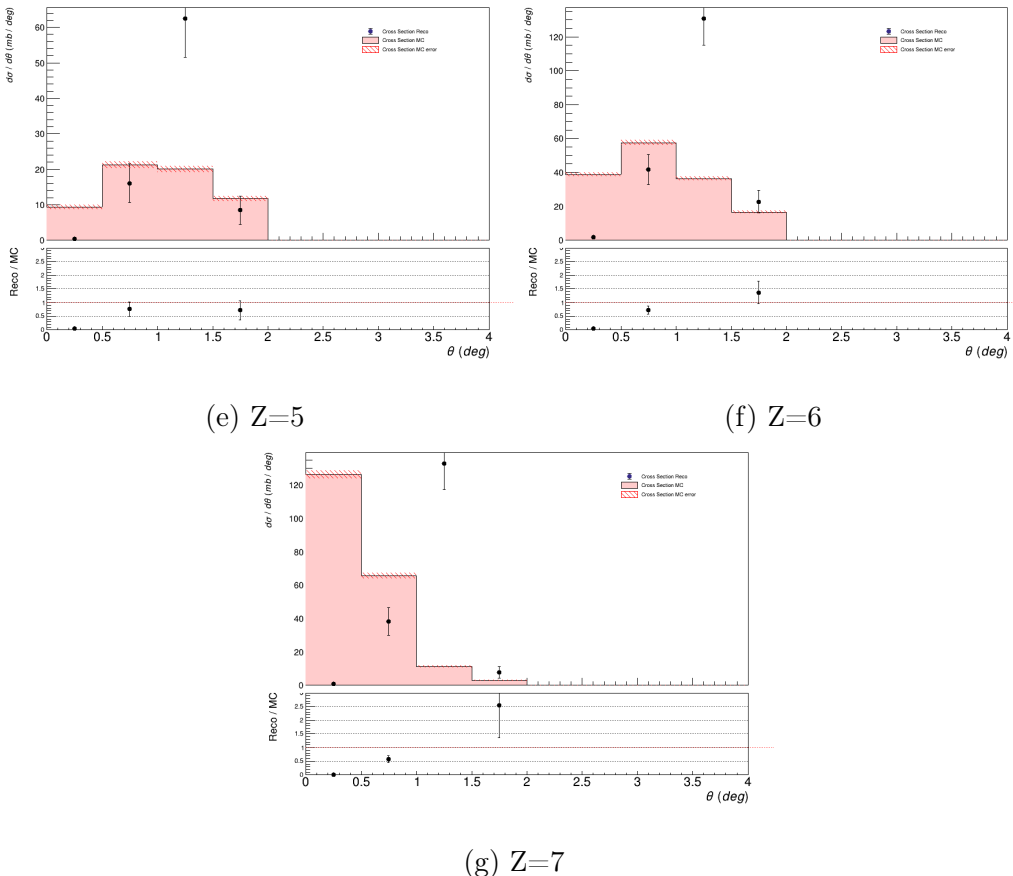


Figure 5.8: Differential angular cross section for the experimental sampling (points) in comparison with generated MC data (in red) and their ratio.

Angle( <i>degree</i> )	$\sigma_{meas}$ (mb)	$\sigma_{MC}$ (mb)
$0.0 \leq \theta < 0.5$	$4 \pm 1$	$16 \pm 0$
$0.5 \leq \theta < 1.0$	$63 \pm 13$	$47 \pm 1$
$1.0 \leq \theta < 1.5$	$120 \pm 18$	$73 \pm 1$
$1.5 \leq \theta < 2.0$	$76 \pm 14$	$97 \pm 2$

(a) Z=1

Angle( <i>degree</i> )	$\sigma_{meas}$ (mb)	$\sigma_{MC}$ (mb)
$0.0 \leq \theta < 0.5$	$8 \pm 2$	$33 \pm 1$
$0.5 \leq \theta < 1.0$	$139 \pm 20$	$96 \pm 2$
$1.0 \leq \theta < 1.5$	$237 \pm 26$	$141 \pm 2$
$1.5 \leq \theta < 2.0$	$83 \pm 14$	$166 \pm 2$

(b) Z=2

Angle( <i>degree</i> )	$\sigma_{meas}$ (mb)	$\sigma_{MC}$ (mb)
$0.5 \leq \theta < 1.0$	$18 \pm 5$	$15 \pm 0$
$1.0 \leq \theta < 1.5$	$25 \pm 6$	$22 \pm 0$
$1.5 \leq \theta < 2.0$	$8 \pm 3$	$22 \pm 0$

(c) Z=3

Table 5.3: Differential angular cross section for the experimental sampling (points) in comparison with generated MC data (in red) and their ratio

Angle( <i>degree</i> )	$\sigma_{meas}$ (mb)	$\sigma_{MC}$ (mb)
$0.5 \leq \theta < 1.0$	$8 \pm 3$	$9 \pm 0$
$1.0 \leq \theta < 1.5$	$34 \pm 8$	$14 \pm 0$
$1.5 \leq \theta < 2.0$	$4 \pm 3$	$10 \pm 0$

(d) Z=4

Angle( <i>degree</i> )	$\sigma_{meas}$ (mb)	$\sigma_{MC}$ (mb)
$0.5 \leq \theta < 1.0$	$16 \pm 5$	$21 \pm 0$
$1.0 \leq \theta < 1.5$	$62 \pm 10$	$20 \pm 0$
$1.5 \leq \theta < 2.0$	$8 \pm 3$	$11 \pm 0$

(e) Z=5

Angle( <i>degree</i> )	$\sigma_{meas}$ (mb)	$\sigma_{MC}$ (mb)
$0.0 \leq \theta < 0.5$	$1 \pm 1$	$38 \pm 1$
$0.5 \leq \theta < 1.0$	$41 \pm 8$	$57 \pm 1$
$1.0 \leq \theta < 1.5$	$130 \pm 15$	$36 \pm 1$
$1.5 \leq \theta < 2.0$	$22 \pm 6$	$16 \pm 0$

(f) Z=6

Angle( <i>degree</i> )	$\sigma_{meas}$ (mb)	$\sigma_{MC}$ (mb)
$0.5 \leq \theta < 1.0$	$38 \pm 8$	$65 \pm 1$
$1.0 \leq \theta < 1.5$	$132 \pm 15$	$11 \pm 0$
$1.5 \leq \theta < 2.0$	$7 \pm 3$	$3 \pm 0$

(g) Z=7

Table 5.3: Differential angular cross section for the experimental sampling (points) in comparison with generated MC data (in red) and their ratio (cont.)



# Conclusions

The FOOT experiment has been conceived with the main aim of measuring double differential fragmentation cross sections of light fragments ( $Z < 10$ ) in the energy range between 100 MeV/u and 800 MeV/n, typical for hadron-therapy and space radioprotection applications. The results will overcome the lack of experimental data in order to improve the Treatment Planning System in hadrontherapy and enhance risk models for space radioprotection. The goal of this thesis is the measurement of elemental and angular differential cross sections of a beam of  $^{16}O$  at 400 MeV/u impinging on a target of graphite (C), for experimental data taken at GSI in 2021.

At first, a pile-up reduction method is applied to experimental data, obtaining a rejection of 1% of the all events. In this way, a lot of spurious events are filtered out in order to enhance the effectiveness of the analysis. Afterwards, a Monte Carlo dataset was generate by FLUKA to simulate the GSI 2021 campaign settings. Performance of fragment identification and Kalman tracking algorithms were studied, in order to retrieve background sources, efficiency and correction factors. Misreconstruction background is lower than 4% of the all events, concerning mainly the light fragments ( $Z < 2$ ). Comparing generated particles and reconstructed tracks, the tracking efficiency has been obtained, with a resolution higher than 80% for heavy fragments ( $Z \geq 3$ ) and higher than 90% for the angular distribution of every charged element. Afterwards, reconstructed and generated charges of every track are compared as a first attempt of correction, obtaining a scale factor close to 1 for all the fragments. All these results underline the reliability of the used algorithms.

Furthermore, fragment cross section and angular differential cross section were measured using MC datasets: the former to obtain efficiency, background and correction, the latter to obtain the yield simulating real data. The results show that there is high correspondence between the generated particles distribution of the former and the MC cross section measurement of the latter, demonstrating how powerful the followed analysis strategy is.

Finally, a first analysis of a subset of GSI 2021 data for elemental and angular differential cross section was obtained. Comparing MC and experimental cross sections, the strong agreement between them, mainly for high fragments, suggests the high capability of reconstruction of the used tracking algorithm and of the overall procedure, despite new studies need to be introduced in order to refine the analysis.

In conclusion, this analysis represents the first step to demonstrate the FOOT experiment reliability to properly achieve cross section measurements and lays the foundation structure for the future data takings that would be carried out in the next future with the full experimental setup.

? qualche dato

# Bibliography

- [1] Collisional cross section, physical and theoretical chemistry.  
<https://chem.libretexts.org/@go/page/1403>.
- [2] William R Leo. *Techniques for nuclear and particle physics experiments: a how-to approach*. Springer Science & Business Media, 2012.
- [3] Wayne D Newhauser and Rui Zhang. The physics of proton therapy. *Physics in Medicine and Biology*, 60(8):R155–R209, mar 2015.
- [4] Robert R. Wilson. Range, straggling, and multiple scattering of fast protons. *Phys. Rev.*, 71:385–386, Mar 1947.
- [5] H. A. Bethe. Molière’s theory of multiple scattering. *Phys. Rev.*, 89:1256–1266, Mar 1953.
- [6] Ulmer W. C.A. Danielewicz P. Bertulani. *Introduction to Nuclear Reactions (1st ed.)*. 2004.
- [7] J.-J. Gaimard and K.-H. Schmidt. A reexamination of the abrasion-ablation model for the description of the nuclear fragmentation reaction. *Nuclear Physics A*, 531(3):709–745, 1991.
- [8] Kenneth S Krane. *Introductory nuclear physics*. Wiley, New York, NY, 1988.
- [9] L. Sihver, C. H. Tsao, R. Silberberg, T. Kanai, and A. F. Barghouty. Total reaction and partial cross section calculations in proton-nucleus ( $z_t \leq 26$ ) and nucleus-nucleus reactions ( $z_p$  and  $z_t \leq 26$ ). *Phys. Rev. C*, 47:1225–1236, Mar 1993.
- [10] Mauro Belli, A. Campa, Giustina Simone, Maria Antonella Tabocchini, Francesca Ballarini, Angelica Facoetti, and A. Ottolenghi. Radiobiological basis of hadrontherapy. *Rivista Medica*, 14:31–42, 03 2008.

- [11] Ugo Amaldi. History of hadrontherapy. *Modern Physics Letters A*, 30:1540018, 05 2015.
- [12] Particle therapy co-operative group, facilities. <https://www.ptcog.ch/index.php/facilities-in-operation>.
- [13] CNAO, Centro Nazionale di Adroterapia per il trattamento di tumori inoperabili, Ospedale Pavia Oncologia. <https://fondazionecnao.it/>.
- [14] Centro di Protonterapia Trento. <https://protonterapia.provincia.tn.it/>.
- [15] Alberto Degiovanni and Ugo Amaldi. History of hadron therapy accelerators. *Physica Medica*, 31(4):322–332, 2015.
- [16] José A. Diaz M. and D. A. Torres. A geant4 simulation of the depth dose percentage in brain tumors treatments using protons and carbon ions. *AIP Conference Proceedings*, 1753(1):080019, 2016.
- [17] Hui Liu and Joe Chang. Proton therapy in clinical practice. *Chinese journal of cancer*, 30:315–26, 05 2011.
- [18] Sandro Rossi. Hadron therapy achievements and challenges: The cnao experience. *Physics*, 4(1):229–257, 2022.
- [19] David Jette and Weimin Chen. Creating a spread-out bragg peak in proton beams. *Physics in Medicine and Biology*, 56(11):N131–N138, may 2011.
- [20] Hywel Owen, Antony Lomax, and Simon Jolly. Current and future accelerator technologies for charged particle therapy. *Nuclear Instruments and Methods in Physics Research Section A: Accelerators, Spectrometers, Detectors and Associated Equipment*, 809:96–104, 2016. Advances in detectors and applications for medicine.
- [21] Antje-Christin Knopf and Antony Lomax. iin vivo/iproton range verification: a review. *Physics in Medicine and Biology*, 58(15):R131–R160, jul 2013.
- [22] Sayyed Bijan Jia, Ali Mowlavi, Hadi Yazdi, and Mahdy Loushab. Impact of range straggling and multiple scattering on proton therapy of brain, using a slab head phantom. *International journal of radiation research (IJRR)*, 12:171–177, 04 2014.

- [23] Aafke Christine Kraan. Range verification methods in particle therapy: Underlying physics and monte carlo modeling. *Frontiers in Oncology*, 5, 2015.
- [24] Michela Marafini, A. Attili, Giuseppe Battistoni, Nicola Belcari, Maria Giuseppina, Niccolò Camarlinghi, Fabrizio Cappucci, Matteo Cecchetti, Piergiorgio Cerello, Fabio Ciciriello, Pablo Cirrone, S. Coli, Francesco Corsi, Giacomo Cuttone, Erika De Lucia, Stefano Ferretti, Riccardo Facchini, Elisa Fiorina, Paola Maria Frallicciardi, and A. Del Guerra. The inside project: Innovative solutions for in-beam dosimetry in hadron-therapy. *Acta Physica Polonica A*, 127:1465–1467, 05 2015.
- [25] Marco Toppi, Guido Baroni, and Giuseppe Battistoni. Monitoring carbon ion beams transverse position detecting charged secondary fragments: Results from patient treatment performed at cnao. *Frontiers in Oncology*, 11, 2021.
- [26] G. Battistoni, I. Mattei, and S. Muraro. Nuclear physics and particle therapy. *Advances in Physics: X*, 1(4):661–686, 2016.
- [27] <https://www.nasa.gov/content/nasas-journey-to-mars>.
- [28] Mariel Borowitz and Jonathan Battat. Multidisciplinary evaluation of next steps for human space exploration: Technical and strategic analysis of options. *Space Policy*, 35:33–42, 2016.
- [29] Walter Tinganelli, Francesca Luoni, and Marco Durante. What can space radiation protection learn from radiation oncology? *Life Sciences in Space Research*, 30:82–95, 2021.
- [30] Joseph Barthel and Nesrin Sarigul-Klijn. A review of radiation shielding needs and concepts for space voyages beyond earth’s magnetic influence. *Progress in Aerospace Sciences*, 110:100553, 2019.
- [31] Kim, myung-hee y. contribution of high charge and energy (hze) ions during solar-particle event of september 29, 1989. nasa, 1999.
- [32] T. K. Gaisser and T. Stanev. Cosmic rays. *The European Physical Journal C - Particles and Fields*, 15(1):150–156, Mar 2000.
- [33] Marco Durante and Francis A. Cucinotta. Physical basis of radiation protection in space travel. *Rev. Mod. Phys.*, 83:1245–1281, Nov 2011.

- [34] Iris Gebauer. *An anisotropic model for galactic cosmic ray transport and its implications for indirect dark matter searches*. PhD thesis, Karlsruher Inst. für Technologie, Diss., 2010, 2010.
- [35] Jae Hun Kim. Three principles for radiation safety: time, distance, and shielding. *The Korean journal of pain*, 31(3):145–146, Jul 2018. PMC6037814[pmcid].
- [36] C. Zeitlin, S. Guetersloh, L. Heilbronn, and J. Miller. Shielding and fragmentation studies. *Radiation Protection Dosimetry*, 116(1-4):123–124, 12 2005.
- [37] Joseph Barthel and Nesrin Sarigul-Klijn. Importance of spherical shell models for radiation shielding designs on space missions. *Journal of Spacecraft and Rockets*, 56(5):1658–1661, 2019.
- [38] Cary Zeitlin and Chiara La Tessa. The role of nuclear fragmentation in particle therapy and space radiation protection. *Frontiers in Oncology*, 6, 3 2016.
- [39] Nikolaos Schetakis, Rodrigo Crespo, José Vázquez-Poletti, Mariano Sasstre, Luis Vázquez, and Alessio Di Iorio. Overview of main radiation transport codes. 06 2020.
- [40] L. Magos. C. lentner (ed.). geigy scientific tables, 8th edition. vol. 1. units of measurement. body fluids. composition of the body. nutrition. 1981, 298 pp. vol. 2. introduction to statistics. statistical tables. mathematical formulae. 1982, 241 pp. vol. 3. physical chemistry. composition of the blood. haematology. human somatometric data. 1984, 359 pp. vol. 4. biochemistry. metabolism of xenobiotics. inborn error of metabolism. pharmacogenetics and ecogenetics. 1986, 330 pp. ciba-geigy, basel, £12.50 each volume. distributed in u.k. by farrand press. *Journal of Applied Toxicology*, 7(6):413–413, 1987.
- [41] P. Schwaller, M. Pepin, B. Favier, C. Richard-Serre, David F. Measday, and P. U. Renberg. PROTON TOTAL CROSS-SECTIONS ON H-1, H-2, HE-4, BE-9, C AND O IN THE ENERGY RANGE 180-MEV TO 560-MEV. *Nucl. Phys. A*, 316:317–344, 1979.
- [42] Exfor Basics I. A quick guide to Exfor. <https://www-nds.iaea.org/nrdc/basics/exfor-basics-1.html>.
- [43] Landolt-börnstein. <https://materials.springer.com/bookshelf>.

- [44] Particle Data Group. Data files and plots of cross-sections and related quantities in the 2014 review of particle physics.
- [45] NNDC. Evaluated nuclear data file (endf).
- [46] Y Yariv, Th Aoust, A Boudard, J Cugnon, J C David, S Lemaire, and S Leray. Intra-nuclear cascade models at low energy? In *ND2007*, Les Ulis, France, 2007. EDP Sciences.
- [47] A. Boudard, J. Cugnon, J.-C. David, S. Leray, and D. Mancusi. New potentialities of the liège intranuclear cascade model for reactions induced by nucleons and light charged particles. *Phys. Rev. C*, 87:014606, Jan 2013.
- [48] J. Dudouet and Juliani. Double-differential fragmentation cross-section measurements of 95 mev/nucleon  $^{12}\text{C}$  beams on thin targets for hadron therapy. *Phys. Rev. C*, 88:024606, Aug 2013.
- [49] M. De Napoli and C. Agodi. Carbon fragmentation cross sections for hadrontherapy and space radiation protection. *Nuclear Data Sheets*, 119:273–276, 2014.
- [50] M. Toppi, Ziad Abou Haidar, Clementina Agodi, M. Alvarez, T. Au-mann, F. Balestra, Giuseppe Battistoni, A. Bocci, T. Böhlen, A. Boudard, Antonio Brunetti, Massimo Carpinelli, Roberto Cirio, Pablo Cirrone, Miguel Cortés-Giraldo, Giacomo Cuttome, M. Napoli, Marco Durante, Juan Pablo Fernández-García, and Vincenzo Patera. Measurement of fragmentation cross sections of  $\text{c } 12$  ions on a thin gold target with the first apparatus. *Physical Review C*, 93, 06 2016.
- [51] John W. Norbury, Jack Miller, Anne M. Adamczyk, Lawrence H. Heil-bronn, Lawrence W. Townsend, Steve R. Blattnig, Ryan B. Norman, Stephen B. Guetersloh, and Cary J. Zeitlin. Nuclear data for space radiation. *Radiation Measurements*, 47(5):315–363, 2012.
- [52] F Luoni, F Horst, CA Reidel, A Quarz, L Bagnale, L Sihver, U We-ber, RB Norman, W de Wet, M Giraudo, G Santin, J Norbury, and M Durante. Total nuclear reaction cross-section database for radiation protection in space and heavy-ion therapy applications. 2021.
- [53] Fragmentation, Jul 2022. <https://www.gsi.de/fragmentation>.
- [54] Giuseppe Battistoni, Marco Toppi, Vincenzo Patera, and The FOOT Collaboration. Measuring the impact of nuclear interaction in particle

- therapy and in radio protection in space: the foot experiment. *Frontiers in Physics*, 8, 2021.
- [55] Giuliana Galati and Andrey Alexandrov. Charge identification of fragments with the emulsion spectrometer of the foot experiment. *Open Physics*, 19(1):383–394, 2021.
  - [56] Roberto Zarrella. Charge identification of nuclear fragments with the time-of-flight detectors of the foot experiment. *Thesis*.
  - [57] ELJEN TECHNOLOGY. [https://www.southernscientific.co.uk/data/file/8/6/SSL\\_EJ228-230.1438855383.pdf](https://www.southernscientific.co.uk/data/file/8/6/SSL_EJ228-230.1438855383.pdf).
  - [58] AdvanSid. [https://advansid.com/attachment/get/up\\_53\\_1432731710.pdf](https://advansid.com/attachment/get/up_53_1432731710.pdf).
  - [59] L. Galli and A.M. Baldini. Wavedaq: An highly integrated trigger and data acquisition system. *Nuclear Instruments and Methods in Physics Research Section A: Accelerators, Spectrometers, Detectors and Associated Equipment*, 936:399–400, 2019. Frontier Detectors for Frontier Physics: 14th Pisa Meeting on Advanced Detectors.
  - [60] Ziad Abou Haidar and Agodi. Performance of upstream interaction region detectors for the first experiment at gsi. *Journal of Instrumentation*, 7:P02006, 02 2012.
  - [61] E. Spiriti and Ch. Finck. Cmos active pixel sensors response to low energy light ions. *Nuclear Instruments and Methods in Physics Research Section A: Accelerators, Spectrometers, Detectors and Associated Equipment*, 875:35–40, 2017.
  - [62] W de Boer and V Bartsch. Measurements with a cmos pixel sensor in magnetic fields. *Nuclear Instruments and Methods in Physics Research Section A: Accelerators, Spectrometers, Detectors and Associated Equipment*, 487(1):163–169, 2002. 3rd International Workshop on Radiation Imaging Detectors.
  - [63] Matteo Morrocchi and Esther Ciarrocchi. Development and characterization of a e-tof detector prototype for the foot experiment. *Nuclear Instruments and Methods in Physics Research Section A: Accelerators, Spectrometers, Detectors and Associated Equipment*, 916:116–124, 2019.
  - [64] Sofia Colombi. The foot experiment: current status and future perspective for nuclear fragmentation studies in particle therapy and space radiation protection. *EPJ*, 2022.

- [65] GSI Center, Jul 2022. <https://www.gsi.de/start/aktuelles>.
- [66] R. Brun and F. Rademakers. ROOT: An object oriented data analysis framework. *Nucl. Instrum. Meth. A*, 389:81–86, 1997.
- [67] SHOE repository. <https://baltig.infn.it/asarti/shoe>.
- [68] Giuseppe Battistoni and Julia Bauer. The fluka code: An accurate simulation tool for particle therapy. *Frontiers in Oncology*, 6, 05 2016.
- [69] Johannes Rauch and Tobias Schlüter. GENFIT — a generic track-fitting toolkit. *Journal of Physics: Conference Series*, 608:012042, may 2015.
- [70] Riccardo Ridolfi. The foot experiment: Trigger and data acquisition (tdaq) development and data analysis. 2022.
- [71] Kaltest: A root-based Kalman filter package. <https://www.jlc.kek.jp/subg/offl/kaltest/>.
- [72] C. Höppner, S. Neubert, B. Ketzer, and S. Paul. A novel generic framework for track fitting in complex detector systems. *Nuclear Instruments and Methods in Physics Research Section A: Accelerators, Spectrometers, Detectors and Associated Equipment*, 620(2):518–525, 2010.
- [73] Xiaocong Ai, Georgiana Mania, Heather Gray, Michael Kuhn, and Nicholas Styles. A gpu-based kalman filter for track fitting. *Computing and Software for Big Science*, 5, 12 2021.
- [74] R. Frühwirth. Application of kalman filtering to track and vertex fitting. *Nuclear Instruments and Methods in Physics Research Section A: Accelerators, Spectrometers, Detectors and Associated Equipment*, 262(2):444–450, 1987.
- [75] Xiaocong Ai, Heather Gray, Andreas Salzburger, and Nicholas Styles. A non-linear kalman filter for track parameters estimation in high energy physics. 12 2021.
- [76] Sebastian Fleischmann. *Track reconstruction in the ATLAS experiment: The deterministic annealing filter*. PhD thesis, Wuppertal U., 2006.
- [77] P. Žugec and C. Weiß. Pulse processing routines for neutron time-of-flight data. *Nuclear Instruments and Methods in Physics Research Section A: Accelerators, Spectrometers, Detectors and Associated Equipment*, 812:134–144, 2016.

- [78] Volker Blobel. An unfolding method for high energy physics experiments. 09 2002.